NASA-CR-203587

IN-71-CR

Final Report on
NASA Ames Grant No. NCC2 - 5064

Development of Multiobjective Optimization Techniques for Sonic Boom Minimization

Technical Monitor: Dr. Eugene Tu

Performance Period:
5/16/94 - 9/15/96

Principal Investigators:

Aditi Chattopadhyay, Associate Professor,
Department of Mechanical and Aerospace Engineering
and
John Narayan Rajadas, Assistant Professor,
Department of Manufacturing and Aeronautical Engineering Technology

Graduate Research Associate:
Narayanan S. Pagaldipti
Department of Mechanical and Aerospace Engineering

Arizona State University
Tempe, Arizona 85287-6106

DECEMBER 1996

TABLE OF CONTENTS

List of Tables

List of Figures

Nomenclature

C_D	inviscid drag coefficient (non-dimensionalized using wing planform area) of wing-body configuration
C_{D_u}	inviscid drag coefficient (non-dimensionalized using unit reference area) of delta wing-body configuration
C_{D_w}	wave drag coefficient (non-dimensionalized using maximum cross-sectional area) of Hack-Adam body
C_L	inviscid lift coefficient (non-dimensionalized using wing planform area) of wing-body configurations
C_{L_u}	inviscid lift coefficient (non-dimensionalized using unit reference area) of delta wing-body configuration
c_o	root chord
c_t	tip chord
d	vertical distance from the axis of aircraft
$\mathbf{F}$	vector of objective functions
F_i	i^{th} objective function
F_{KS}	Kreisselmeier-Steinhauser function
g_j	j^{th} constraint
l_b	aircraft length
l_n	nose length
M_x	out of plane bending moment on wing
M_y	in plane bending moment on wing
M_∞	freestream Mach number
NDV	number of design variables
$\mathbf{R}$	vector of discrete flow equations
r	radius of centerbody
r_m	maximum nose radius
T	torsion on the wing
t_c	wing thickness-to-chord ratio
u	x-component velocity
v	y-component velocity
W	aircraft weight
W_{fus}	fuselage weight
W_{wsk}	wing skin weight
W_{wsp}	wing spar weight

w	z-component velocity
w_s	wing span
x	streamwise coordinate
x_b	break length
x_w	wing starting location
y	tangential coordinate
z	spanwise coordinate
Δp	change in pressure from freestream value, normalized by freestream value
Φ	design variable vector
ϕ_m	m^{th} design variable
η	tangential coordinate
κ	thermal conductivity of air
λ	leading edge sweep (delta wing-body case)
λ_1	first leading edge sweep (doubly swept wing-body case)
λ_2	second leading edge sweep (doubly swept wing-body case)
ρ	density of air
σ	vector of normal and shear stresses in wing box beam
ξ	streamwise coordinate
ζ	normal coordinate
Subscripts	
max, u	upper bound
min, l	lower bound
∞	free stream condition

Abstract

A discrete, semi-analytical sensitivity analysis procedure has been developed for calculating aerodynamic design sensitivities. The sensitivities of the flow variables and the grid coordinates are numerically calculated using direct differentiation of the respective discretized governing equations. The sensitivity analysis techniques are adapted within a parabolized Navier Stokes equations solver. Aerodynamic design sensitivities for high speed wing-body configurations are calculated using the semi-analytical sensitivity analysis procedures. Representative results obtained compare well with those obtained using the finite difference approach and establish the computational efficiency and accuracy of the semi-analytical procedures.

Multidisciplinary design optimization procedures have been developed for aerospace applications namely, gas turbine blades and high speed wing-body configurations. In complex applications, the coupled optimization problems are decomposed into sublevels using multilevel decomposition techniques. In cases with multiple objective functions, formal multiobjective formulation such as the Kreisselmeier-Steinhauser function approach and the modified global criteria approach have been used. Nonlinear programming techniques for continuous design variables and a hybrid optimization technqiue, based on a simulated annealing algorithm, for discrete design variables have been used for solving the optimization problems.

The optimization procedure for gas turbine blades improves the aerodynamic and heat transfer characteristics of the blades. The two-dimensional, blade-to-blade aerodynamic analysis is performed using a panel code. The blade heat transfer analysis is performed using an in-house developed finite element procedure. The optimization procedure yields blade shapes with significantly improved velocity and temperature distributions.

The multidisciplinary design optimization procedures for high speed wing-body configurations simultaneously improve the aerodynamic, the sonic boom and the structural characteristics of the aircraft. The flow solution is obtained using a comprehensive parabolized Navier Stokes solver. Sonic boom analysis is performed using an extrapolation procedure. The aircraft wing load carrying member is modeled as either an isotropic or a composite box beam. The isotropic box beam is analyzed using thin wall theory. The composite box beam is analyzed using a finite element procedure. The developed optimization procedures yield significant improvements in all the performance criteria and provide interesting design trade-offs. The semi-analytical sensitivity analysis techniques offer significant computational savings and allow the use of comprehensive analysis procedures within design optimization studies.

1. Introduction

Design of aerospace vehicles is associated with complex multidisciplinary couplings. The design process inherently involves interactions between various disciplines of engineering such as aerodynamics, structures, dynamics, aeroelasticity, heat transfer, controls and acoustics. Also, the impact of the operation of aerospace vehicles on the environment is gaining attention and importance at all stages of the design process. Examples of factors that have environmental impact include the engine noise, sonic boom, emission effects etc. The final vehicle configuration has to satisfy a number of design requirements associated with the various disciplines. Often, these multidisciplinary requirements are conflicting in nature. Design requirements that enhance the performance of the aerospace system in one discipline, may deteriorate its performance in other disciplines. For example, in high speed aircraft, it is desirable to have slender wings and a slender fuselage from aerodynamics point of view. From a structural view point, it is necessary to have a sufficiently thick wing to carry the aerodynamic loading well within material limits. From a payload point of view, the fuselage has to have a minimum volume to accomodate an economically feasible amount of payload. These are examples of conflicting design requirements. Also, the impact of individual design features on the overall system performance is often not apparent to the designer. Therefore, the designer must be able to evaluate the various conflicting design requirements and provide insight into the effect of each design feature on the overall performance of the system. In a typical aircraft design procedure, these conflicting design requirements are compromised through a trade-off study. With the advent of modern computer technology, Multidisciplinary Design Optimization (MDO) techniques could be well suited for such design trade-off studies.

1.1 Multidisciplinary Design Optimization (MDO)

Multidisciplinary design optimization involves the coupling of two or more disciplines, associated with the design of a sytem, within a closed loop numerical optimization procedure. The importance of multidisciplinary couplings in successful design optimization of aerospace systems has been long recognized. Sobieszczanski and Loendorf [1] developed a MDO procedure for the design of fuselage structures. Fulton et al. [2] performed design optimization of a complete aircraft model that involved 700 design variables and 2500 constraints. Barthelemy et al. [3-5] developed MDO procedures for supersonic transport aircraft which included structural, aerodynamic and aeroelastic criteria. Celi and Friedmann [6] developed a MDO procedure that performed structural optimization of rotor blades with constraints on their aeroelastic behavior. Chattopadhyay et al. [7-12] and McCarthy et al. [13-14] have developed several MDO procedures that integrate structural, aeroelastic and aerodynamic performance criteria for various rotary wing applications. In these research efforts, optimization is performed by addressing all the design criteria in a single level. Such an optimization approach, referred to as the "individual discipline feasible" formulation [15-16], can be inefficient and may restrict design variable movement due to conflicting design requirements.

1.1.1 MDO Using Multilevel Decomposition

A highly integrated and large design optimization problem can be decomposed into a number of smaller subproblems using a process referred to as multilevel decomposition. The subproblems are optimized separately and a procedure, which accounts for the interdisciplinary coupling, is devised so that at convergence, the resulting optimum is that of the original non-decomposed problem. Decomposition also helps decrease the size of the optimization problem because each subproblem uses only a subset of the original design parameters as design variables. For some problems, the process that accounts for interdisciplinary coupling may be non-iterative. Multilevel decomposition techniques with a non-iterative interdisciplinary coupling process are called hierarchical decomposition techniques [16]. For highly coupled systems, the process that establishes interdisciplinary coupling is iterative in nature. Multilevel decomposition techniques with such iterative coupling processes fall under non-hierarchical decomposition techniques [16]. Multilevel decomposition techniques have been widely applied to problems in structural optimization. Schmit et al. [17-18] developed a hierarchical procedure for truss and wing box models that included local and global constraints. Hughes [19] developed similar ideas for naval structures. Sobieszczanski [20] developed a linear decomposition method for a large class of nonlinear design problems. The effectiveness of this method has been demonstrated on two- and three-level structural framework design problems [21-23]. Using the same method, Wrenn and Dovi [24] optimized a complex transport wing model with 1200 variables and 2500 nonlinear constraints. The method has been adapted to penalty function optimization techniques [25] where improved efficiency is demonstrated by limiting the optimization to a single minimization step for each subproblem within each cycle. Kirsch [26] used a multilevel formulation for the simultaneous analysis and optimization of reinforced concrete beams. An obstacle to the use of multilevel methods is that they can be computationally expensive because of the cycling necessary to account for the coupling between the subproblems. Barthelemy and Riley [27] developed an improved approach that increases the computational efficiency of multilevel optimization by adopting constraint approximation and temporary constraint deletion. Barthelemy [28] reviewed various engineering applications of heuristic decomposition methods. Bloebaum and Hajela [29] have applied these methods for the decomposition of non-hierarchical systems.

Attempts have also been made to use multilevel decomposition techniques for MDO problems. Rogan and Kolb [30] showed how a transport aircraft preliminary design problem can be treated as a multilevel optimization problem. Adelman et al. [31] have reported a two-level procedure for performing integrated aerodynamic, dynamic and structural optimization of rotor blades, based on the multilevel optimization strategy described in Ref. 20. Chattopadhyay et al. [32] developed a three-level, non-hierarchical procedure for optimization of helicopter rotor blades with the integration of aerodynamics, dynamics, aeroelastic stability and structures. The blade aerodynamic performance was improved in level 1, the dynamic performance and the aeroelastic stability roots of the blade were improved in level 2 and the blade structural weight was reduced in level 3 subject to stress constraints. Chattopadhyay et al. [33] also developed a two-level decomposition procedure for improved high-speed cruise and hovering performance of tiltrotor aircraft. These non-hierarchical multilevel optimization procedures cycle through the various levels until global convergence is achieved. The interdisciplinary coupling between the various levels is established through optimal sensitivity parameters [34-37]. At a given level, the optimal sensitivity parameters are the derivatives of the objective functions and design variables of the other levels with respect to design variables of the current level.

1.1.2 Accuracy of MDO Procedures

The validity of the designs obtained using MDO procedures depends strongly upon the accuracy of the analysis techniques used. The reliability and practical implementation of the design trends obtained from MDO procedures are critically dependent on the accuracy of the analysis techniques used within them. It is essential to integrate accurate, efficient and comprehensive analysis techniques within the MDO procedures so that the optimum designs obtained are dependable. Such detailed analysis techniques are computationally intensive and therefore, can be prohibitive within a design optimization environment. For example, in high speed aircraft design, it is essential to use a comprehensive aerodynamic analysis procedure to solve the complex flow field around the aircraft. Although accurate detailed analyses of many complex flow fields are now possible using efficient Computational Fluid Dynamics (CFD) solvers and powerful supercomputers, viscous-compressible flow calculations around supersonic aircraft can require several Central Processing Unit (CPU) hours per steady-state solution. Therefore, the use of such comprehensive analysis procedures within MDO can be computationally expensive, especially if gradient-based techniques are used. Gradient-based optimization techniques require the calculation of the derivatives of the objective functions and constraints of the optimization procedure with respect to the design variables during each optimization cycle. The calculation of these derivatives is termed sensitivity analysis. In a typical multidisciplinary optimization process, most of the computational effort is spent towards sensitivity analysis. The computational time required for performing sensitivity analysis directly increases with (1) the complexity of the analysis procedures used and (2) the number of design variables involved. Since accurate MDO procedures typically use comprehensive analysis procedures and a large number of design variables, it is important to develop and use efficient sensitivity analysis techniques.

1.2 Design Sensitivity Analysis

Sensitivity analysis, in which the derivative of a system performance function (e.g., the lift-to-drag ratio of an aircraft wing) with respect to design variables (e.g., wing root chord) is calculated, is an essential component in gradient-based design optimization. A widely used technique for performing sensitivity analysis is the method of finite differences. In this method, the performance function, whose derivatives with respect to design variables are to be calculated, is first evaluated at the given design point. Then, the design variables are perturbed, one at a time and the function is evaluated at each one of these perturbed design points. The derivatives of the performance function are then calculated by taking the differences between perturbed function values and the original function value and dividing these differences by the corresponding perturbations in the design variables. As a result, the use of this method requires several applications of the appropriate analysis procedures. For example, if there are NDV design variables, then the finite difference method requires the execution of the analysis procedures at least (NDV+1) times. Thus the associated computational cost can be prohibitive when this method is used in an optimization problem involving a large number of design variables and computationally intensive analysis procedures (such as CFD codes for evaluating three-dimensional flow fields). Therefore, it is necessary to develop alternative techniques to calculate design sensitivities, so that complex analysis procedures may be more useful as practical design tools in multidisciplinary design optimization environments.

1.2.1 Semi-Analytical Sensitivity Analysis

It has been recognized that analytical or semi-analytical techniques for sensitivity analysis are preferable over the finite difference method due to their computational efficiency and accuracy [38]. Two such techniques are the direct differentiation approach and the adjoint variable approach [39-43]. These techniques have been widely used for sensitivity calculations in structural optimization [39-43]. In the direct differentiation approach, the governing equations for the response variables (e. g., flow variables in a CFD procedure) are differentiated with respect to the design variables using chain rule. This yields a large linear system of equations for the sensitivities of the system response variables. The derivatives of the system performance functions are readily calculated from these response sensitivities. In the adjoint variable approach, adjoint variable vectors are obtained as the solution to an adjoint problem. The adjoint variable vectors are then used to calculate the sensitivities of the system performance functions. It is important to note that in the adjoint variable approach, the design sensitivities of the system response variables are not calculated. The two semi-analytical techniques are equivalent and yield identical results for the sensitivities. There has been a widespread interest in using these techniques for calculating aerodynamic sensitivities. Carlson and Elbanna [44-47] have used the direct differentiation technique on the discretized transonic small perturbation and the full potential equations to obtain aerodynamic sensitivities. Baysal et al. [48-51] have performed discrete sensitivity analysis by directly differentiating the three-dimensional Euler equations. Korivi et al. [52] and Newman et al. [53] have developed a semi-analytical sensitivity analysis procedure for the thin-layer Navier-Stokes equations using an incremental strategy. In this approach, the aerodynamic sensitivities are calculated in an incremental fashion similar to the flow solution.

Depending on the type of governing equations used, semi-analytical sensitivity analysis can also be categorized either as a discrete approach [44-54] or a continuous approach [55-59]. The discrete approach takes analytical derivatives of the discretized governing equations with respect to design variables. The continuous approach, on the other hand, calculates the derivatives directly, based on the continuous governing equations, by using the generalized calculus of variations [55-56]. In other words, the governing equations are differentiated prior to their discretization. The sensitivities are then calculated using a numerical algorithm similar to the one used for obtaining the response solution. Jameson et al. [57-59] have developed such continuous sensitivity approaches using the adjoint variable method to calculate aerodynamic sensitivities.

Bischof et al. [60-62] have developed a technique called automatic differentiation for calculating sensitivities. Automatic differentiation techniques are based on the fact that every function, no matter how complicated, is executed as a sequence of elementary operations such as additions, multiplications and elementary functions such as Sine and Cosine in a computer. By applying the chain rule repeatedly to the composition of these elementary operations and functions, the derivatives of any complex function can be calculated exactly, even though this might be a computationally intensive process.

1.2.2 Grid Sensitivity Analysis

Two main components of an aerodynamic sensitivity analysis procedure are: (1) the calculation of the sensitivities of the flow variables and (2) the calculation of the sensitivities of the computational grid with respect to the aerodynamic design variables. The sensitivities of the flow variables are dependent upon the sensitivities of the computational grid coordinates [44-54]. In most of the aforementioned work, finite difference techniques were used to calculate the grid sensitivities. Very few formal investigations have been reported on the development of analytical or semi-analytical techniques for computing grid sensitivities. Advanced elliptic and hyperbolic grid generation codes are often used for generating grids for evaluating the flow fields of aircraft configurations [63-64]. The use of the finite difference method for calculating grid sensitivities can be computationally prohibitive in such cases. Taylor et al. [65-68] have developed a grid sensitivity analysis procedure in which the Jacobian matrix of the entire grid with respect to the grid points on the boundary of the domain is calculated. The sensitivities of the surface grid points are calculated using an elastic membrane analogy to represent the computational domain and the surface grid sensitivities are calculated from a structural analysis code using the finite element method. Extension of this technique to complex three-dimensional flow fields can be complicated and time consuming. Further, the use of an additional structural analysis code increases computing time. Sadrehaghighi et al. [69-70] proposed an analytical approach for calculating grid sensitivities in which algebraic grid generation is performed using transfinite interpolation and surface parameterization in terms of design variables. The transfinite interpolation equations are analytically differentiated to obtain the grid sensitivities. The most general parameterization of the boundaries would require the specification of every grid point on the boundary which, however, is impractical from a computational point of view. A quasi-analytical parameterization is used in Refs. 69 and 70 that allows an aircraft component to be specified by a relatively small number of parameters. However, the technique does not offer a great amount of generality because most CFD codes use complex grids which are generated using methods based on partial differential equations. Therefore, there is a need for developing efficient analytical or semi-analytical techniques, for calculating the grid sensitivities, to be used within aerodynamic sensitivity analysis.

1.3 Practical Applications of MDO

The application of MDO to practical aerospace design problems is briefly discussed below. The procedure integrates aerodynamics, structures and sonic boom in an effort to obtain an optimum high speed aircraft configuration. In 1987, the US government identified the development of long range, high speed transports as one of the three major goals in aeronautics [71]. Since then, the National Aeronautics and Space Agency (NASA) and the aerospace industry have conducted studies to determine the feasibility of developing an economically viable High Speed Civil Transport (HSCT) and the required technology development [72-74]. These studies have indicated that HSCT will have a potential market at the turn of the 21st century provided the vehicle is environmentally compatible and can compete economically with advanced long-range subsonic transports. The HSCT concept used in the studies [75] is a baseline vehicle designed to carry 305 passengers with a range of 5000 nautical miles and a cruise Mach number of 2.4. Advanced technologies that are required in the major discipline areas of aerodynamics, structures, propulsion and flight deck systems for the development of the HSCT have since been identified [75]. NASA has developed the High Speed Research (HSR) Program which addresses these requirements, primarily in the disciplines of aerodynamics and structures. In aerodynamics, one of the goals of the HSR Program has been to achieve increased lift-to-drag ratios throughout the flight regime which requires improved wing designs. High speed wing design efforts utilize state-of-the-art CFD tools for flow analysis. Methods currently being developed for supersonic wing design couple optimization schemes with CFD solvers (Full Potential, Euler, Thin Layer Navier Stokes and Parabolized Navier Stokes) [76-79]. Reductions in airframe weight also contribute towards better performance. Improvements in the areas of airframe structures and materials can lead to significant weight reductions in the wing, fuselage and other structural components. These improvements may be achieved through the development of new light weight high temperature materials, innovative structural concepts, low-cost fabrication techniques and aeroelastic tailoring. Optimization techniques are very useful in these efforts to develop improved designs.

Supersonic civil transport aircraft of the present day have unacceptable sonic boom characteristics which prevent routine flights over population centers. The term sonic boom refers to pressure variations away from the ambient pressure, at locations away from the aircraft (usually at ground level). To make supersonic travel economically feasible for commercial operators, sonic boom levels produced by future supersonic transport must be low enough to avoid severe restrictions being placed on their flight paths. Hence sonic boom prediction and minimization becomes an integral part of the high speed aircraft design process. Sonic boom studies conducted in the past [80-87] indicate that low boom configurations typically exhibit a bluntness in the aircraft nose region. However, extreme nose bluntness leads to degradation in the aerodynamic performance which might affect the aircraft payload capacity. Such conflicting design requirements between the various disciplines demand the use of formal multidisciplinary optimization techniques to study the design trade-offs associated with the development of a vehicle such as the HSCT.

2. Objectives

The primary goal of the present work has been to develop an efficient semi-analytical sensitivity analysis technique to be integrated within advanced CFD codes for aerospace applications. The CFD solver and the sensitivity analysis technique can then be used within formal multidisciplinary design optimization procedures to investigate interdisciplinary couplings and design trade-offs associated with applications such as high speed aircraft design. The secondary goal of the present work has been to develop multidisciplinary design optimization procedures for a practical aerospace application namely, the minimization of sonic boom associated with high speed wing-body configurations.

In the present work, an efficient semi-analytical aerodynamic sensitivity analysis has been developed inside a CFD solver and used within the multidisciplinary design optimization of high speed wing-body configurations. The parabolized Navier-Stokes (PNS) equations have been used extensively to compute complex, steady, supersonic, viscous flow fields [88-89]. A CFD procedure, UPS3D, that is based on a finite volume approach [90-91] has been used to solve the PNS equations for supersonic flows past high speed configurations in the present work. The semi-analytical aerodynamic sensitivity analysis procedure has been developed within the UPS3D code using the discrete, direct differentiation approach. Here, the sensitivities of the flow variables and the performance functions (e.g., drag and lift coefficients) are calculated by differentiating the discretized governing equations [92-93]. The choice of the discrete approach has been due to the fact that the finite volume algorithm of the PNS solver is readily amenable to such an approach. The grid sensitivities, which are part of the semi-analytical aerodynamic sensitivity analysis, have been efficiently calculated by differentiating the discretized, hyperbolic grid generation equations [94-95] with respect to design variables. This results in a linear system of equations, which are solved readily for the grid sensitivities. Aerodynamic design sensitivities have been calculated for high speed configurations using the semi-analytical sensitivity analysis procedures. Representative results have been compared with those obtained using the finite difference approach to establish the computational accuracy and efficiency of the developed semi-analytical procedures.

To demonstrate the efficiency of the semi-analytical sensitivity analysis procedures within an design optimization environment, a few MDO procedures have been developed for the integrated aerodynamic, sonic boom and structural optimization of high speed configurations [92-93, 96-101]. In these optimization procedures, the aerodynamic design sensitivities are calculated using the semi-analytical sensitivity procedures. The optimization procedures use a two-level decomposition, where necessary. Appropriate aerodynamic and structural models have been developed for the wing-body configurations. Design variables from these models have been used within the optimization procedures.

3. Sensitivity Analysis

The calculation of the derivatives of all the objective functions and constraints with respect to the design variables within an optimization procedure is referred to as sensitivity analysis. To illustrate the different sensitivity analysis techniques, consider an aerodynamic performance coefficient, C_j. In the following sections, symbols in bold letters represent vectors. In general, the coefficient C_j explicitly depends on the vector of flow variables, **Q**, the vector of computational grid coordinates, **X** and the vector of design variables, **Φ**. This can be represented mathematically as follows.

$$C_j = C_j(\mathbf{Q}(\mathbf{\Phi}), \mathbf{X}(\mathbf{\Phi}), \mathbf{\Phi}) \tag{1}$$

The vector of flow variables, **Q**, and the vector of grid coordinates, **X**, are also functions of the vector of design variables, **Φ**. The derivative of C_j with respect to the i^{th} design variable, ϕ_i, is of interest here. As mentioned earlier, this derivative can be calculated using either the finite difference method or the semi-analytical approach which are discussed in the following sections.

3.1 Finite Difference Sensitivity Analysis

In this approach, the coefficient C_j is evaluated at the current design point, **Φ** and at a perturbed design point, $\mathbf{\Phi} + \Delta\mathbf{\Phi}_i$, where $\Delta\mathbf{\Phi}_i$ is a vector whose elements, with the exception of the i^{th} element, are all equal to zero. The i^{th} element of the $\Delta\mathbf{\Phi}_i$ vector is equal to $\Delta\phi_i$ where $\Delta\phi_i$ is a small, user-specified perturbation to the i^{th} design variable, ϕ_i. Then, the derivative of C_j with respect to ϕ_i is evaluated by,

$$\frac{dC_j}{d\phi_i} = \frac{\{C_j(\mathbf{Q}(\mathbf{\Phi}+\Delta\mathbf{\Phi}_i), \mathbf{X}(\mathbf{\Phi}+\Delta\mathbf{\Phi}_i), \mathbf{\Phi}+\Delta\mathbf{\Phi}_i) - C_j(\mathbf{Q},\mathbf{X},\mathbf{\Phi})\}}{\Delta\phi_i} \tag{2}$$

Thus, if there are NDV design variables in the vector **Φ**, then the coefficient C_j has to be evaluated (NDV+1) times, in order to calculate its derivatives with respect to all the design variables using the one-sided finite difference method. This means that the aerodynamic analysis needs to be executed (NDV+1) times which can be computationally expensive if a CFD-based analysis procedure (e.g., 3-D PNS solver) is used.

3.2 Discrete Semi-Analytical Aerodynamic Sensitivity Analysis

In this research, the sensitivities of the aerodynamic performance coefficients of the aircraft with respect to the relevant geometric parameters (design variables) are calculated using the direct differentiation approach which is described in detail below.

The derivative of C_j with respect to the i^{th} design variable, ϕ_i, can be obtained by using the chain rule of differentiation on Eq. 1. This is expressed mathematically as,

$$\frac{dC_j}{d\phi_i} = \left\{\frac{\partial C_j}{\partial \mathbf{Q}}\right\}^T \left\{\frac{\partial \mathbf{Q}}{\partial \phi_i}\right\} + \left\{\frac{\partial C_j}{\partial \mathbf{X}}\right\}^T \left\{\frac{\partial \mathbf{X}}{\partial \phi_i}\right\} + \frac{\partial C_j}{\partial \phi_i} \qquad (3)$$

Here, the terms $\left\{\frac{\partial C_j}{\partial \mathbf{Q}}\right\}$, $\left\{\frac{\partial C_j}{\partial \mathbf{X}}\right\}$ and $\frac{\partial C_j}{\partial \phi_i}$ can be readily calculated since the explicit dependence of the aerodynamic coefficient C_j on the vector of flow variables, **Q**, the vector of grid coordinates, **X**, and the i^{th} design variable ϕ_i are usually known. The term $\left\{\frac{\partial \mathbf{Q}}{\partial \phi_i}\right\}$, which represents the sensitivities of the flow variables with respect to the i^{th} design variable, cannot be calculated easily because the dependence of **Q** on ϕ_i is implicit in nature. Similarly, the term $\left\{\frac{\partial \mathbf{X}}{\partial \phi_i}\right\}$, which represents the sensitivities of the computational grid coordinates with respect to the i^{th} design variable, cannot be calculated readily because of the implicit dependence of **X** on ϕ_i. In this research, these two terms are calculated using the direct differentiation approach. The calculation of the sensitivities of the flow variables is discussed here and the calculation of the grid sensitivities is discussed in the next section. In order to calculate $\left\{\frac{\partial \mathbf{Q}}{\partial \phi_i}\right\}$, the discretized governing differential equations for the flow variables need to be considered. The governing differential equations, discretized over a computational domain, are expressed as follows.

$$\{\ \mathbf{R}(\mathbf{Q}(\mathbf{\Phi}),\mathbf{X}(\mathbf{\Phi}),\mathbf{\Phi})\ \} = \{\mathbf{0}\} \qquad (4)$$

Equation 4, when differentiated with respect to ϕ_i, yields the following.

$$\left\{\frac{d\mathbf{R}}{d\phi_i}\right\} = \left\{\frac{\partial \mathbf{R}}{\partial \mathbf{Q}}\right\}^T \left\{\frac{\partial \mathbf{Q}}{\partial \phi_i}\right\} + \left\{\frac{\partial \mathbf{R}}{\partial \mathbf{X}}\right\}^T \left\{\frac{\partial \mathbf{X}}{\partial \phi_i}\right\} + \left\{\frac{\partial \mathbf{R}}{\partial \phi_i}\right\} = \{\mathbf{0}\} \qquad (5)$$

Equation 5 represents a set of linear algebraic equations in $\left\{\frac{\partial \mathbf{Q}}{\partial \phi_i}\right\}$ which need to be solved. It is to be noted that the terms $\left\{\frac{\partial \mathbf{R}}{\partial \mathbf{Q}}\right\}$, $\left\{\frac{\partial \mathbf{R}}{\partial \mathbf{X}}\right\}$ and $\left\{\frac{\partial \mathbf{R}}{\partial \phi_i}\right\}$ in Eq. 5, can be calculated easily, since the explicit dependence of **R** on **Q**, **X** and ϕ_i is known from the numerical scheme used to obtain Eq. 4. It is also to be noted that the grid sensitivity vector, $\left\{\frac{\partial \mathbf{X}}{\partial \phi_i}\right\}$, must be calculated before Eq. 5 can be solved for the flow variable sensitivities, $\left\{\frac{\partial \mathbf{Q}}{\partial \phi_i}\right\}$.

3.3 Grid Sensitivity Technique

The term $\left\{\dfrac{\partial X}{\partial \phi_i}\right\}$, appearing in Eqs. 3 and 5, represents the grid sensitivity vector. One way to calculate the grid sensitivity vector is to use the finite difference method, described in Section 3.1, by perturbing each design variable individually and executing the grid generation procedure (NDV+1) times. Over the past decade, grid generation techniques have advanced to a very high level. Grid generation techniques, based on elliptic and hyperbolic differential equations, are widely used in CFD instead of algebraic techniques due to their robustness [63]. With such advanced grid generation techniques, the finite difference method for calculating grid sensitivities can be expensive. In this research, a direct differentiation approach has been developed for calculating grid sensitivities. A hyperbolic grid generation scheme developed by Steger et al. [102-104] has been used by the flow solver used in the present research. The hyperbolic grid generation scheme in Ref. 104, formulated from grid orthogonality and cell volume specification, can be used to generate three-dimensional grids for a wide variety of geometries. Using this scheme, generalized computational coordinates $\xi(x,y,z)$, $\eta(x,y,z)$ and $\zeta(x,y,z)$ are sought where the body surface is chosen to coincide with $\zeta(x,y,z) = 0$ and the surface distribution of ξ = constant and η = constant are user-specified. Here, the xyz coordinate system is a Cartesian coordinate system representing the physical domain and $\xi\eta\zeta$ coordinate system is the computational domain used by the CFD procedure for aerodynamic analysis [Fig. 1].

The grid generation equations are derived from orthogonality relations between ξ and ζ, between η and ζ and a cell volume or a finite Jacobian J constraint [101]:

$$x_\xi x_\zeta + y_\xi y_\zeta + z_\xi z_\zeta = 0 \tag{6a}$$

$$x_\eta x_\zeta + y_\eta y_\zeta + z_\eta z_\zeta = 0 \tag{6b}$$

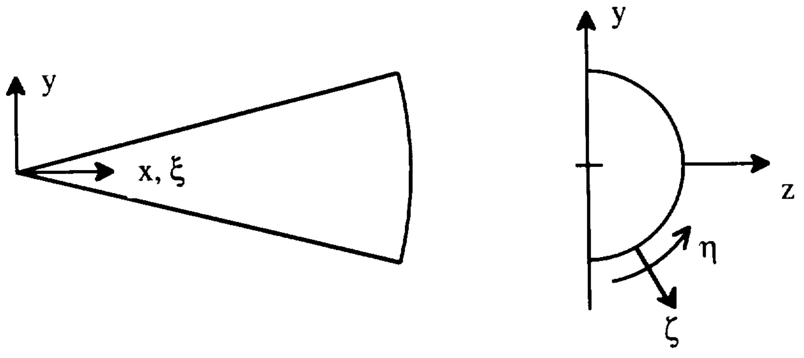

Figure 1. Coordinate systems.

$$x_\xi(y_\eta z_\zeta - y_\zeta z_\eta) + x_\eta(y_\zeta z_\xi - y_\xi z_\zeta) + x_\zeta(y_\xi z_\eta - y_\eta z_\xi) = \mathbf{\Delta} V \tag{6c}$$

or, with $\vec{r}$ defined as $(x,y,z)^T$

$$\vec{r}_\xi \cdot \vec{r}_\zeta = 0 \tag{7a}$$

$$\vec{r}_\eta \cdot \vec{r}_\zeta = 0 \tag{7b}$$

$$\left|\frac{\partial(x,y,z)}{\partial(\xi,\eta,\zeta)}\right| = J^{-1} = \mathbf{\Delta} V \tag{7c}$$

In Eq. 6c, ΔV is a user-specified cell volume distribution. The cell volume at a given grid point is set equal to the computed surface area element times a user specified arc length for marching in the ζ direction [104]. Equations 6 comprise a system of nonlinear partial differential equations which can be solved for the grid coordinates, x, y and z, using a non-iterative implicit finite difference scheme by marching in the ζ direction, starting with the initial (x, y, z) data specified at $\zeta = 0$. Linearization of Eqs. 6 is performed about the previous marching step in ζ [104].

Let $\Delta\xi = \Delta\eta = \Delta\zeta = 1$ such that $\xi = j-1$, $\eta = k-1$ and $\zeta = l-1$. Central differencing of Eqs. 6 in ξ and η with two-point backward implicit differencing in ζ leads to the following difference equations.

$$\mathbf{A}_l \delta_\xi(\vec{r}_{l+1} - \vec{r}_l) + \mathbf{B}_l \delta_\eta(\vec{r}_{l+1} - \vec{r}_l) + \mathbf{C}_l(\vec{r}_{l+1} - \vec{r}_l) = \vec{g}_{l+1} \tag{8}$$

where

$$\mathbf{A} = \begin{pmatrix} x_\zeta & y_\zeta & z_\zeta \\ 0 & 0 & 0 \\ (y_\eta z_\zeta - y_\zeta z_\eta) & (x_\zeta z_\eta - x_\eta z_\zeta) & (x_\eta y_\zeta - x_\zeta y_\eta) \end{pmatrix} \tag{9a}$$

$$\mathbf{B} = \begin{pmatrix} 0 & 0 & 0 \\ x_\zeta & y_\zeta & z_\zeta \\ (y_\zeta z_\xi - y_\xi z_\zeta) & (x_\xi z_\zeta - x_\zeta z_\xi) & (x_\zeta y_\xi - x_\xi y_\zeta) \end{pmatrix} \tag{9b}$$

$$\mathbf{C} = \begin{pmatrix} x_\xi & y_\xi & z_\xi \\ x_\eta & y_\eta & z_\eta \\ (y_\xi z_\eta - y_\eta z_\xi) & (x_\eta z_\xi - x_\xi z_\eta) & (x_\xi y_\eta - x_\eta y_\xi) \end{pmatrix} \tag{9c}$$

$$\vec{g}_{l+1} = \begin{pmatrix} 0 \\ 0 \\ \Delta V_{l+1} \end{pmatrix} \tag{9d}$$

and $$\delta_\xi \vec{r}_j = \frac{\vec{r}_{j+1} - \vec{r}_{j-1}}{2}, \quad \delta_\eta \vec{r}_k = \frac{\vec{r}_{k+1} - \vec{r}_{k-1}}{2} \tag{9e}$$

Here, only those indices that change are indicated, thus r_{l+1} implies $r_{j,k,l+1}$ and r_{j+1} implies $r_{j+1,k,l}$ etc. Multiplying through Eq. 8 by $\mathbf{C}_l^{-1}$ and approximately factoring gives

$$(\mathbf{I}+\mathbf{C}_l^{-1}\mathbf{B}_l\delta_\eta)(\mathbf{I}+\mathbf{C}_l^{-1}\mathbf{A}_l\delta_\xi)(\vec{r}_{l+1}-\vec{r}_l) = \mathbf{C}_l^{-1}\vec{g}_{l+1} \tag{10}$$

where **I** is the identity matrix. Equation 10 is a sequence of two block tridiagonal systems which can be solved readily to obtain the grid coordinates vector, $\vec{r}_{l+1}$, which is part of the grid coordinates vector, **X**.

The grid sensitivities $\left\{\frac{\partial \mathbf{X}}{\partial \phi_i}\right\}$.are obtained by directly differentiation Eq. 10 with respect to the ith design variable, ϕ_i. To illustrate the semi-analytical grid sensitivity technique, Eq. 10 is rewritten based on the approximate factorization algorithm as:

$$(\mathbf{I}+\mathbf{C}_l^{-1}\mathbf{B}_l\delta_\eta)\vec{t}_{l+1} = \mathbf{C}_l^{-1}\vec{g}_{l+1} \tag{11}$$

where

$$(\mathbf{I}+\mathbf{C}_l^{-1}\mathbf{A}_l\delta_\xi)(\vec{r}_{l+1}-\vec{r}_l) = \vec{t}_{l+1} \tag{12}$$

Thus, the grid generation is performed in two steps. First, Eq. 11 is solved for $\vec{t}_{l+1}$, using a block tridiagonal solver. The quantity, $\vec{t}_{l+1}$, is then used as the right hand side of Eq. 12. Next, Eq. 12 is solved using a block tridiagonal solver to obtain the new grid coordinates vector, $\vec{r}_{l+1}$. The grid sensitivity calculations proceed in a similar two-step fashion. First, Eq. 11 is differentiated with respect to ϕ_i resulting in,

$$(\mathbf{I}+\mathbf{C}_l^{-1}\mathbf{B}_l\delta_\eta)\frac{d\vec{t}_{l+1}}{d\phi_i} = \frac{d(\mathbf{C}_l^{-1}\vec{g}_{l+1})}{d\phi_i} - \frac{d(\mathbf{I}+\mathbf{C}_l^{-1}\mathbf{B}_l\delta_\eta)}{d\phi_i}\vec{t}_{l+1} \tag{13}$$

Equation 13 is solved for the derivatives, $\frac{d\vec{t}_{l+1}}{d\phi_i}$. Next, Eq. 12 is differentiated with respect to ϕ_i resulting in the following equation for $\left\{\frac{\partial\vec{r}_{l+1}}{\partial\phi_i}\right\}$, which are part of the grid sensitivity vector.

$$(\mathbf{I}+\mathbf{C}_l^{-1}\mathbf{A}_l\delta_\xi)\frac{d(\vec{r}_{l+1}-\vec{r}_l)}{d\phi_i} = \frac{d\vec{t}_{l+1}}{d\phi_i} - \frac{d(\mathbf{I}+\mathbf{C}_l^{-1}\mathbf{A}_l\delta_\xi)}{d\phi_i}(\vec{r}_{l+1}-\vec{r}_l) \tag{14}$$

Equations 13 and 14 represent linear systems of equations for the grid sensitivities. It is important to note that the coefficient matrices on the left hand side of Eqs. 11 and 13 are identical. The coefficient matrices in Eqs. 12 and 14 are also identical. The block tridiagonal systems in Eqs. 11 and 12 are solved within the grid generation procedure using a L-U decomposition scheme which is also used for solving Eqs. 13 and 14, after the appropriate right hand side vectors of Eqs. 13 and 14 are calculated for each design variable. The computational cost of calculating these right hand side vectors is significantly lower than that of recomputing the L-U decompositions for NDV design variables (as would be required by the finite difference approach during the execution of the grid generation procedure an additional NDV times) resulting in significant CPU savings.

3.4 Adaptation of Sensitivity Analysis to Flow Solver

In this research, the semi-analytical aerodynamic sensitivity analysis technique described above has been adapted to be used with the flow solver (PNS equations). The assumptions made in deriving the PNS equations are outlined below [88-90]. The streamwise derivatives of the viscous terms are neglected. This assumption is considered valid for high Reynolds number flows [90]. The inviscid region of the flow field must be supersonic and the streamwise velocity component must be positive everywhere. Thus streamwise flow separation is not allowed but crossflow separation is allowed. Unlike the unsteady Navier-Stokes equations which require time marching numerical schemes, the PNS equations are solved using space marching schemes resulting in reductions in computational time and memory requirements. The PNS equations are written in the computational domain ($\xi\eta\zeta$ system) as [90],

$$\frac{\partial\hat{\mathbf{E}}}{\partial\xi}+\frac{\partial\hat{\mathbf{F}}}{\partial\eta}+\frac{\partial\hat{\mathbf{G}}}{\partial\zeta}=0 \tag{15}$$

where

$$\hat{\mathbf{E}} = \left(\frac{\xi_x}{J}\right)\mathbf{E}_i + \left(\frac{\xi_y}{J}\right)\mathbf{F}_i + \left(\frac{\xi_z}{J}\right)\mathbf{G}_i \tag{16a}$$

$$\hat{\mathbf{F}} = \left(\frac{\eta_x}{J}\right)(\mathbf{E}_i - \mathbf{E}_v^*) + \left(\frac{\eta_y}{J}\right)(\mathbf{F}_i - \mathbf{F}_v^*) + \left(\frac{\eta_z}{J}\right)(\mathbf{G}_i - \mathbf{G}_v^*) \tag{16b}$$

$$\hat{\mathbf{G}} = \left(\frac{\zeta_x}{J}\right)(\mathbf{E}_i - \mathbf{E}_v^*) + \left(\frac{\zeta_y}{J}\right)(\mathbf{F}_i - \mathbf{F}_v^*) + \left(\frac{\zeta_z}{J}\right)(\mathbf{G}_i - \mathbf{G}_v^*) \tag{16c}$$

The inviscid flux vectors (subscript i) and viscous flux vectors (subscript v) are defined by

$$\begin{aligned} \mathbf{E}_i &= \begin{bmatrix} \rho u & \rho u^2+p & \rho uv & \rho uw & (E_t+p)u \end{bmatrix}^T \\ \mathbf{F}_i &= \begin{bmatrix} \rho v & \rho uv & \rho v^2+p & \rho vw & (E_t+p)v \end{bmatrix}^T \\ \mathbf{G}_i &= \begin{bmatrix} \rho w & \rho uw & \rho vw & \rho w^2+p & (E_t+p)w \end{bmatrix}^T \end{aligned} \tag{17}$$

$$\begin{aligned} \mathbf{E}_v &= \begin{bmatrix} 0 & \tau_{xx} & \tau_{xy} & \tau_{xz} & u\tau_{xx}+v\tau_{xy}+w\tau_{xz}-q_x \end{bmatrix}^T \\ \mathbf{F}_v &= \begin{bmatrix} 0 & \tau_{xy} & \tau_{yy} & \tau_{yz} & u\tau_{xy}+v\tau_{yy}+w\tau_{yz}-q_y \end{bmatrix}^T \\ \mathbf{G}_v &= \begin{bmatrix} 0 & \tau_{xz} & \tau_{yz} & \tau_{zz} & u\tau_{xz}+v\tau_{yz}+w\tau_{zz}-q_z \end{bmatrix}^T \end{aligned} \tag{18}$$

$$E_t = \rho\left[e + \frac{1}{2}\left(u^2+v^2+w^2\right)\right] \tag{19}$$

The superscript "*" on the viscous flux vectors in Eqs. 16 indicates that derivatives with respect to ξ have been omitted. In these equations, p is the pressure, ρ is the density, u, v and w are the velocity components in the x, y and z directions, respectively, e is the internal energy, τ is the viscous stress and q is the heat conduction rate. All physical quantities have been non-dimensionalized appropriately [90]. The partial derivatives, ξ_x, ξ_y, ..., ζ_y, ζ_z, are the metrics of transformation between the $\xi\eta\zeta$ and the xyz system and J denotes the Jacobian of the transformation. The flow solver is the UPS3D code [90] developed at NASA Ames Research Center. The computational procedure used in this code integrates the PNS equations using an implicit, approximately factored, finite-volume algorithm where the crossflow inviscid fluxes are evaluated by Roe's flux-difference splitting scheme [91]. The UPS3D code also has the capability of calculating the inviscid flow field, by solving the PNS equations without the viscous terms. In the present research, this inviscid option has been used while evaluating the flow field. The upwind algorithm is used to improve the resolution of the shock waves over that obtained with the conventional central differencing schemes. The post-processor in the UPS3D solver evaluates the non-dimensional force coefficients, such as lift coefficient (C_L) and drag coefficient (C_D), by integrating the pressure distributions over the surface of the body. Non-dimensionalization of these force coefficients is performed using a user-specified characteristic area of the aircraft. The numerical algorithm of the UPS3D solver calculates the flow solution by marching in the ξ direction. The PNS equations given by Eq. 15 take on the following discrete form using the finite-volume algorithm.

$$\begin{gathered}\left(\hat{\mathbf{E}}_i\right)_{k,l}^{n+1} + \left(\hat{\mathbf{F}}_i - \hat{\mathbf{F}}_v^*\right)_{k+\frac{1}{2},l}^{n+\frac{1}{2}} + \left(\hat{\mathbf{G}}_i - \hat{\mathbf{G}}_v^*\right)_{k,l+\frac{1}{2}}^{n+\frac{1}{2}} - \\ \left(\hat{\mathbf{E}}_i\right)_{k,l}^{n} - \left(\hat{\mathbf{F}}_i - \hat{\mathbf{F}}_v^*\right)_{k-\frac{1}{2},l}^{n+\frac{1}{2}} - \left(\hat{\mathbf{G}}_i - \hat{\mathbf{G}}_v^*\right)_{k,l-\frac{1}{2}}^{n+\frac{1}{2}} = 0\end{gathered} \tag{20}$$

where the subscript k represents a grid point in the η direction, the subscript l denotes a grid point in the ζ direction, the superscript n denotes the grid point in the current ξ location and the superscript n+1 denotes the next ξ step in the space marching scheme. To avoid departure behavior of the flow solutions associated with Eq. 20, it is necessary to suppress the ellipticity that is caused by the pressure gradient in the streamwise momentum equation. This is accomplished by a technique developed by Vigneron et al. [105] in which the streamwise flux vector, $\left(\hat{\mathbf{E}}_i\right)_{k,l}^{n}$, is separated into two parts as follows.

$$\left(\hat{\mathbf{E}}_i\right)_{k,l}^{n} = \hat{\mathbf{E}}^*\left(dS_{k,l}^{n}, U_{k,l}^{n}\right) + \hat{\mathbf{E}}^p\left(dS_{k,l}^{n}, U_{k,l}^{n-1}\right) \tag{21}$$

This splitting of the streamwise flux vector is unique to PNS solvers. However, even when the inviscid option is used, the UPS3D solver [90] applies this splitting in its numerical algorithm. This is one of the distinguishing features of the UPS3D solver. The forms of $\hat{\mathbf{E}}^*$ and $\hat{\mathbf{E}}^p$ of Eq. 21 are given by

$$\hat{\mathbf{E}}^* = \begin{pmatrix} \rho\hat{U} \\ \rho u\hat{U} + \left(\frac{\xi_x}{J}\right)\omega p \\ \rho v\hat{U} + \left(\frac{\xi_y}{J}\right)\omega p \\ \rho w\hat{U} + \left(\frac{\xi_z}{J}\right)\omega p \\ (E_t + p)\hat{U} \end{pmatrix} \qquad \hat{\mathbf{E}}^p = \begin{pmatrix} 0 \\ \left(\frac{\xi_x}{J}\right)(1-\omega)p \\ \left(\frac{\xi_y}{J}\right)(1-\omega)p \\ \left(\frac{\xi_z}{J}\right)(1-\omega)p \\ 0 \end{pmatrix} \tag{22}$$

$$\hat{U} = \left(\frac{\xi_x}{J}\right)u + \left(\frac{\xi_y}{J}\right)v + \left(\frac{\xi_z}{J}\right)w \tag{23}$$

An eigenvalue analysis shows that Eq. 20 is hyperbolic-parabolic with respect to the new dependent vector $\hat{\mathbf{E}}^*$, provided that ω satisfies the relation

$$\omega = \min\left[1, \frac{\sigma\gamma M_\xi^2}{1+(\gamma-1)M_\xi^2}\right] \tag{24}$$

where M_ξ is the Mach number in the ξ direction and σ is a factor used to account for nonlinearities not otherwise included in the analysis. In Eq. 21, $\hat{\mathbf{E}}^*\left(d\mathbf{S}_{k,l}^n, \mathbf{U}_{k,l}^n\right)$ means that $\hat{\mathbf{E}}^*$ is evaluated from Eq. 22 using the values of the metrics and the flow variables corresponding to station n. Similarly, the term $\hat{\mathbf{E}}^p\left(d\mathbf{S}_{k,l}^n, \mathbf{U}_{k,l}^{n-1}\right)$ in Eq. 21 indicates that $\hat{\mathbf{E}}^p$ is evaluated from Eq. 22 using the values of the metrics corresponding to station n and the flow variables (including ω) corresponding to station (n-1). To avoid the difficulty of extracting the flow properties from the flux vector $\hat{\mathbf{E}}^*$ and to simplify the application of the implicit algorithm, a change is made in the dependent variable from $\hat{\mathbf{E}}^*$ to the vector of conserved variables, **U**, using the following linearization.

$$\hat{\mathbf{E}}^*\left(d\mathbf{S}^n, \mathbf{U}^n\right) = \hat{\mathbf{A}}^{*^{n-1}}\mathbf{U}^n \tag{25}$$

where

$$\mathbf{U} = \left[\rho \quad \rho u \quad \rho v \quad \rho w \quad E_t\right]^T \tag{26}$$

and

$$\hat{\mathbf{A}}_{k,l}^{*^{n-1}} = \frac{\partial \hat{\mathbf{E}}^*\left(d\mathbf{S}^n, \mathbf{U}^{n-1}\right)}{\partial \mathbf{U}^{n-1}} \tag{27}$$

Using Roe's flux vector splitting for the crossflow fluxes, the Vigneron technique [105] for suppressing departure solution and an implicit algorithm, Eq. 20 is approximately factored into two block-tridiagonal systems to yield the following discrete governing equations for calculating the flow field [88].

$$\left[\hat{\mathbf{A}}^{*}_{k,l} + \frac{\partial\left(\delta_\eta\left\{\hat{\mathbf{F}}^{I}_{i} - \hat{\mathbf{F}}_{v}\right\}\right)}{\partial \mathbf{U}_{k,l}} + \bar{\delta}_\eta\left(\frac{\partial\left\{\hat{\mathbf{F}}^{I}_{i} - \hat{\mathbf{F}}_{v}\right\}}{\partial \mathbf{U}}\right)\bullet\right]^{n}\left[\left(\hat{\mathbf{A}}^{*}_{k,l}\right)^{-1}\right]^{n} \mathrm{x}$$

$$\left[\hat{\mathbf{A}}^{*}_{k,l} + \frac{\partial\left(\delta_\zeta\left\{\hat{\mathbf{G}}^{I}_{i} - \hat{\mathbf{G}}_{v}\right\}\right)}{\partial \mathbf{U}_{k,l}} + \bar{\delta}_\zeta\left(\frac{\partial\left\{\hat{\mathbf{G}}^{I}_{i} - \hat{\mathbf{G}}_{v}\right\}}{\partial \mathbf{U}}\right)\bullet\right]^{n} \delta^{n+1}\mathbf{U}_{k,l} = \mathrm{RHS}^{n} \tag{28a}$$

where

$$\begin{aligned}\mathrm{RHS}^{n} = & -\left(\hat{\mathbf{A}}^{*^{n}}_{k,l} - \hat{\mathbf{A}}^{*^{n-1}}_{k,l}\right)\mathbf{U}^{n}_{k,l} - \delta_\eta\left(\hat{\mathbf{F}}^{II}_{i} - \hat{\mathbf{F}}_{v}\right) \\ & - \delta_\zeta\left(\hat{\mathbf{G}}^{II}_{i} - \hat{\mathbf{G}}_{v}\right) - \left[\hat{\mathbf{E}}^{p}\left(d\mathbf{S}^{n+1}_{k,l}, \mathbf{U}^{n}_{k,l}\right) - \hat{\mathbf{E}}^{p}\left(d\mathbf{S}^{n}_{k,l}, \mathbf{U}^{n-1}_{k,l}\right)\right]\end{aligned} \tag{28b}$$

$\mathbf{F}^{I}$ and $\mathbf{G}^{I}$ are the first order cross flow fluxes in the η and the ζ direction, respectively. $\mathbf{F}^{II}$ and $\mathbf{G}^{II}$ are the second order cross flow fluxes in the η and the ζ direction, respectively. The inviscid option in the UPS3D solver ignores the viscous terms on both sides of Eq. 28a while solving for the flow variables. The differencing operators in Eq. 28 are defined as follows.

$$\begin{aligned}\delta_\kappa \boldsymbol{\Phi} &= \boldsymbol{\Phi}_{m+\frac{1}{2}} - \boldsymbol{\Phi}_{m-\frac{1}{2}} \\ \bar{\delta}_\kappa\left(\frac{\partial \boldsymbol{\Psi}}{\partial \mathbf{U}}\right)\bullet\boldsymbol{\Phi} &= \frac{\partial \boldsymbol{\Psi}_{m+\frac{1}{2}}}{\partial \mathbf{U}_{m+1}}\boldsymbol{\Phi}_{m+1} - \frac{\partial \boldsymbol{\Psi}_{m-\frac{1}{2}}}{\partial \mathbf{U}_{m-1}}\boldsymbol{\Phi}_{m-1}\end{aligned} \tag{29}$$

Using the discrete semi-analytical aerodynamic sensitivity analysis approach, the discretized governing flow equations, Eq. 28, are directly differentiated with respect to the ith design variable, ϕ_i. This yields a system of algebraic equations for the flow sensitivities which can be approximately factored into two block tridiagonal systems as follows.

$$
\left[\hat{\mathbf{A}}^*_{k,l} + \frac{\partial\left(\delta_\eta\left\{\hat{\mathbf{F}}^I_i - \hat{\mathbf{F}}_v\right\}\right)}{\partial \mathbf{U}_{k,l}} + \bar{\delta}_\eta\left(\frac{\partial\left\{\hat{\mathbf{F}}^I_i - \hat{\mathbf{F}}_v\right\}}{\partial \mathbf{U}}\right)\bullet\right]^n \left[\left(\hat{\mathbf{A}}^*_{k,l}\right)^{-1}\right]^n \mathrm{x}
$$

$$
\left[\hat{\mathbf{A}}^*_{k,l} + \frac{\partial\left(\delta_\zeta\left\{\hat{\mathbf{G}}^I_i - \hat{\mathbf{G}}_v\right\}\right)}{\partial \mathbf{U}_{k,l}} + \bar{\delta}_\zeta\left(\frac{\partial\left\{\hat{\mathbf{G}}^I_i - \hat{\mathbf{G}}_v\right\}}{\partial \mathbf{U}}\right)\bullet\right]^n \delta^{n+1}\left(\frac{d\mathbf{U}_{k,l}}{d\phi_i}\right) =
$$

$$
\frac{d\left(\mathrm{RHS}^n\right)}{d\phi_i} -
$$

$$
\frac{d\left(\begin{array}{l}\left[\hat{\mathbf{A}}^*_{k,l} + \dfrac{\partial\left(\delta_\eta\left\{\hat{\mathbf{F}}^I_i - \hat{\mathbf{F}}_v\right\}\right)}{\partial \mathbf{U}_{k,l}} + \bar{\delta}_\eta\left(\dfrac{\partial\left\{\hat{\mathbf{F}}^I_i - \hat{\mathbf{F}}_v\right\}}{\partial \mathbf{U}}\right)\bullet\right]^n \left[\left(\hat{\mathbf{A}}^*_{k,l}\right)^{-1}\right]^n \mathrm{x} \\ \left[\hat{\mathbf{A}}^*_{k,l} + \dfrac{\partial\left(\delta_\zeta\left\{\hat{\mathbf{G}}^I_i - \hat{\mathbf{G}}_v\right\}\right)}{\partial \mathbf{U}_{k,l}} + \bar{\delta}_\zeta\left(\dfrac{\partial\left\{\hat{\mathbf{G}}^I_i - \hat{\mathbf{G}}_v\right\}}{\partial \mathbf{U}}\right)\bullet\right]^n\end{array}\right)}{d\phi_i} \delta^{n+1}\mathbf{U}_{k,l} \qquad (30)
$$

It is to be noted that the block tridiagonal coefficient matrices on the left hand sides of Eqs. 28 and 30 are identical. Hence, the L-U decompositions of the block tridiagonal matrices of Eq. 28 can also be used for the calculation of the flow variable sensitivities from Eq. 30. Thus, it is only required to calculate the appropriate right hand side vectors of Eq. 30 for all the design variables, in order to calculate the flow variable sensitivities. In the finite difference approach, the flow solution needs to be solved an additional NDV times which implies that the L-U decompositions of the coefficient matrices of Eq. 28 are performed an additional NDV times. This makes the direct differentiation approach computationally very efficient over the finite difference approach. The following section describes the application of these procedures for the aerodynamic design sensitivity analysis of a high speed wing-body configuration.

3.5 Design Sensitivity Calculations for Wing-Body Configurations

The semi-analytical sensitivity techniques for grid sensitivity and aerodynamic sensitivity calculations, described above, are used to calculate the design sensitivities for a high speed configuration. Numerical results for a delta wing-body configuration (Fig. 2) are presented here. In this configuration, the center body is axisymmetric and is a combination of a nose region and an extended cylindrical region. The forebody of the vehicle has a sharp nose with the radius, r, varying quadratically with the axial coordinate, x, over the nose length, l_n. The radius of the cylindrical region is denoted r_m. The variation of the body radius of the body changes from the tip to its maximum value, r_m, over the nose length, l_n, is given by

$$r = r_m - r_m\left(1 - \frac{x}{l_n}\right)^2 \tag{31}$$

Here, x is the axial coordinate measured from the tip of the aircraft. The wing planform parameters include: leading edge sweep, λ, root chord, c_o, wing span, w_s and the wing starting location, x_w, measured from the nose of the aircraft. The wing cross section is a diamond airfoil with the thickness-to-chord ratio, t_c. The total length of the body is denoted l_b. The values of these parameters used in the present case are: $c_o = 7.08$ m, $\lambda = 66.0$ degrees, $w_s = 3.53$ m, $t_c = 0.052$, $r_m = 0.57$ m, $l_n = 6.01$ m, $x_w = 8.21$ m and $l_b = 17.52$ m. A three-dimensional hyperbolic grid, with 75 grid points in the circumferential (η) direction and 80 grid points in the normal (ζ) direction, is generated around the wing-body configuration for the flow analysis using the UPS3D solver. The space marching scheme of the UPS3D solver uses a step size of 0.01 m. The aerodynamic sensitivities are calculated for a cruise Mach number of 2.5 and an angle of attack of 5 degrees.

The grid sensitivities with respect to the leading edge sweep (λ), root chord (c_o), wing span (w_s) and thickness-to-chord ratio (t_c) are presented in Table 1. Comparisons are made with those obtained using the finite difference technique. The finite difference grid sensitivities are calculated by perturbing each of the four variables by 0.1 percent. As shown, there is excellent agreement between the results from the two techniques. The sensitivities at the first grid point are zero because this point lies in the nose region of the aircraft and the four variables considered are all wing design variables which do not affect the grid in the nose region.

Table 1. Grid sensitivity of the three-dimensional hyperbolic grid.

Grid point (x, y, z)	Design variable	Finite difference grid sensitivity method	Direct differentiation grid sensitivity method
(0.300, 0.044, 0.008)	Sweep (λ)	(0.000, 0.000, 0.000)	(0.000, 0.000, 0.000)
	Root chord (c_o)	(0.000, 0.000, 0.000)	(0.000, 0.000, 0.000)
	Wing span (w_s)	(0.000, 0.000, 0.000)	(0.000, 0.000, 0.000)
	Thickness/chord (t_c)	(0.000, 0.000, 0.000)	(0.000, 0.000, 0.000)
(13.19, -0.561, 0.104)	Sweep (λ)	(0.0, 0.0016, 0.0001)	(0.0, 0.0016, 0.0001)
	Root chord (c_o)	(0.0,-0.0171,-0.0109)	(0.0,-0.0170,-0.0108)
	Wing span (w_s)	(0.0,-0.0148,-0.0096)	(0.0,-0.0149,-0.0097)
	Thickness/chord (t_c)	(0.0,-1.0693,-0.7514)	(0.0,-1.0695,-0.7517)

A comparison of the CPU time on a CRAY-2 [Fig. 3] shows a 40 percent reduction achieved for one complete grid sensitivity analysis using the direct differentiation approach over the finite difference method. This clearly demonstrates the significant computational savings achievable by using the direct differentiation approach. This is particularly important in a formal design optimization procedure where several such design sensitivity analyses are necessary.

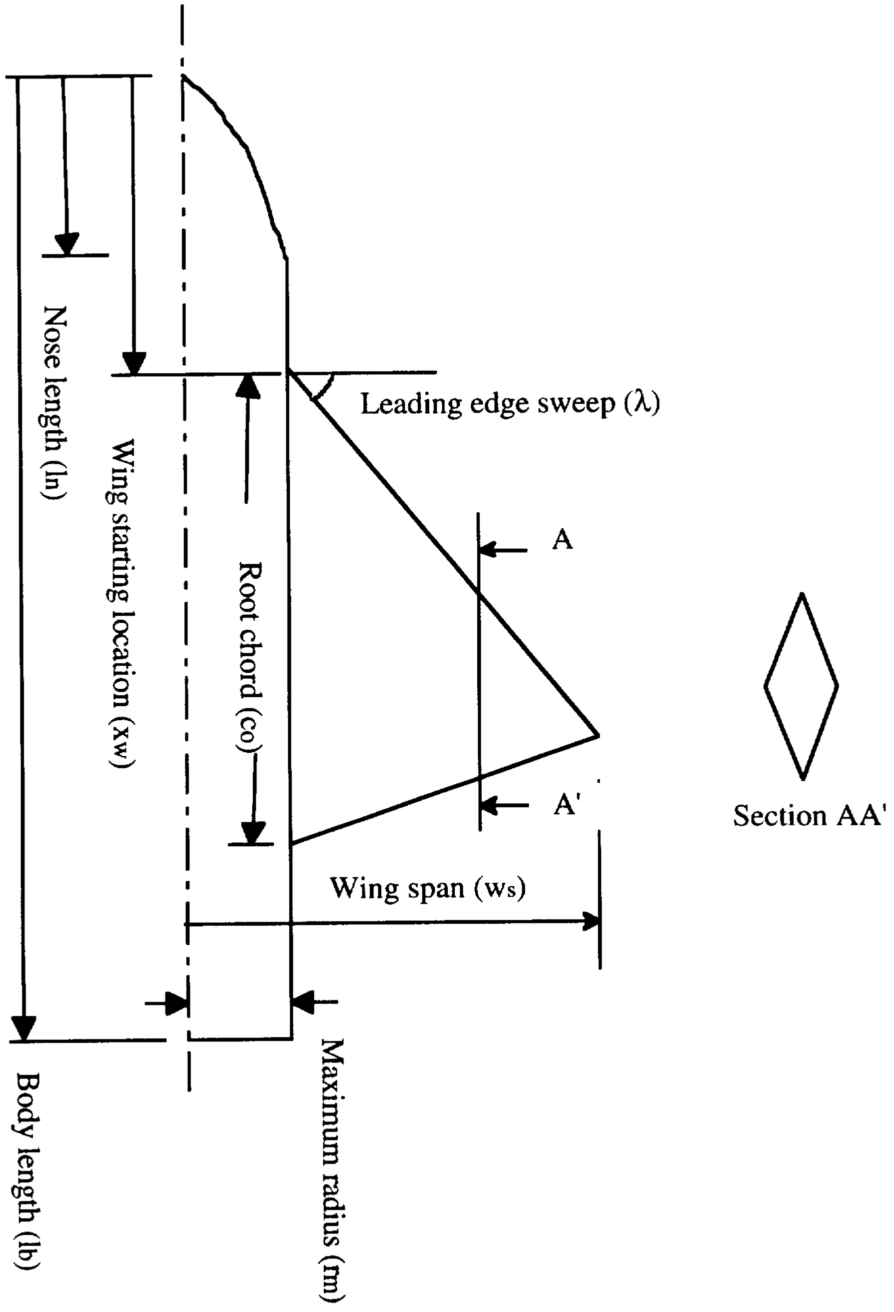

Figure 2. Delta wing-body configuration (schematic).

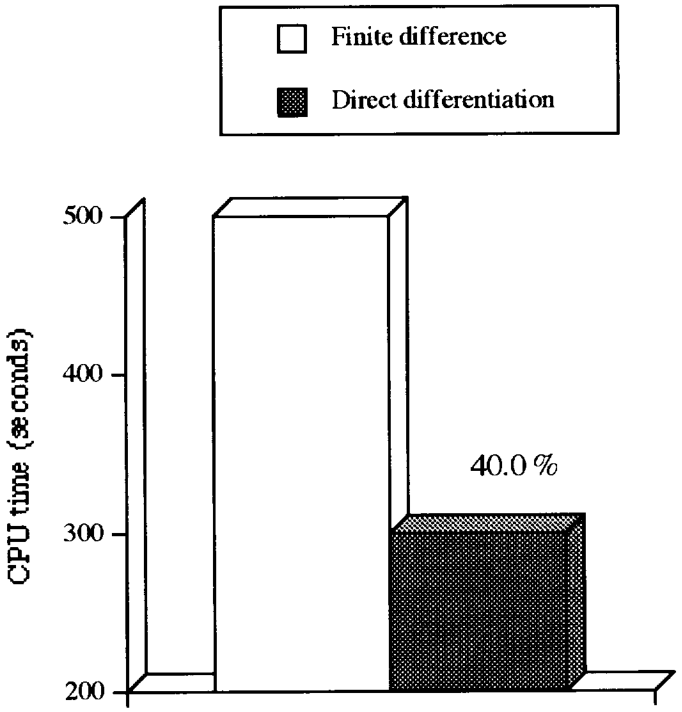

Figure 3. Comparison of CPU time (seconds) for the sensitivity of hyperbolic grid.

Results obtained from the aerodynamic sensitivity analysis procedure are presented next. The sensitivities of the inviscid drag coefficient (C_D) and the lift coefficient (C_L), calculated using the direct differentiation technique as well as the finite difference approach, are presented in Tables 2 and 3 respectively. It must be noted that column 3 in Tables 2 and 3 presents the results of the semi-analytical aerodynamic sensitivity approach with finite difference grid sensitivity while column 4 presents the results of the semi-analytical aerodynamic sensitivity approach with semi-analytical grid sensitivity. As shown, the results from both techniques are in excellent agreement. For one complete sensitivity analysis, the direct differentiation technique with finite difference grid sensitivity calculations results in a 30.5 percent reduction in computing time compared to the fully finite difference sensitivity analysis [Fig. 4]. The semi-analytical sensitivity analysis technique with semi-analytical grid sensitivity calculations yields a 39 percent reduction in computing time compared to the finite difference approach [Fig. 4]. This further illustrates the efficiency of the discrete semi-analytical technique for grid sensitivity calculations.

Table 2. Sensitivity of the drag coefficient, ($dC_D/d\phi_i$).

Design variable	Finite difference	Semi-analytical method (with finite difference grid sensitivity)	Semi-analytical method (with semi-analytical grid sensitivity)
Sweep (λ)	-0.0097676 (1/deg.)	-0.0096949 (1/deg.)	-0.0097558 (1/deg.)
Root chord (c_o)	0.0382632 (1/m)	0.0356884 (1/m)	0.0377937 (1/m)
Wing span (w_s)	0.0241877 (1/m)	0.0240876 (1/m)	0.0241989 (1/m)
Thickness/chord (t_c)	1.4164357	1.4218040	1.4233772

Table 3. Sensitivity of the lift coefficient, ($dC_L/d\phi_i$).

Design variable	Finite difference	Semi-analytical method (with finite difference grid sensitivity)	Semi-analytical method (with semi-analytical grid sensitivity)
Sweep (λ)	-0.0943222 (1/deg.)	-0.0944966 (1/deg.)	-0.0955675 (1/deg.)
Root chord (c_o)	0.0738337 (1/m)	0.0795423 (1/m)	0.0745353 (1/m)
Wing span (w_s)	0.0713310 (1/m)	0.0721375 (1/m)	0.0717341 (1/m)
Thickness/chord (t_c)	-1.9207192	-1.9154491	-1.9166282

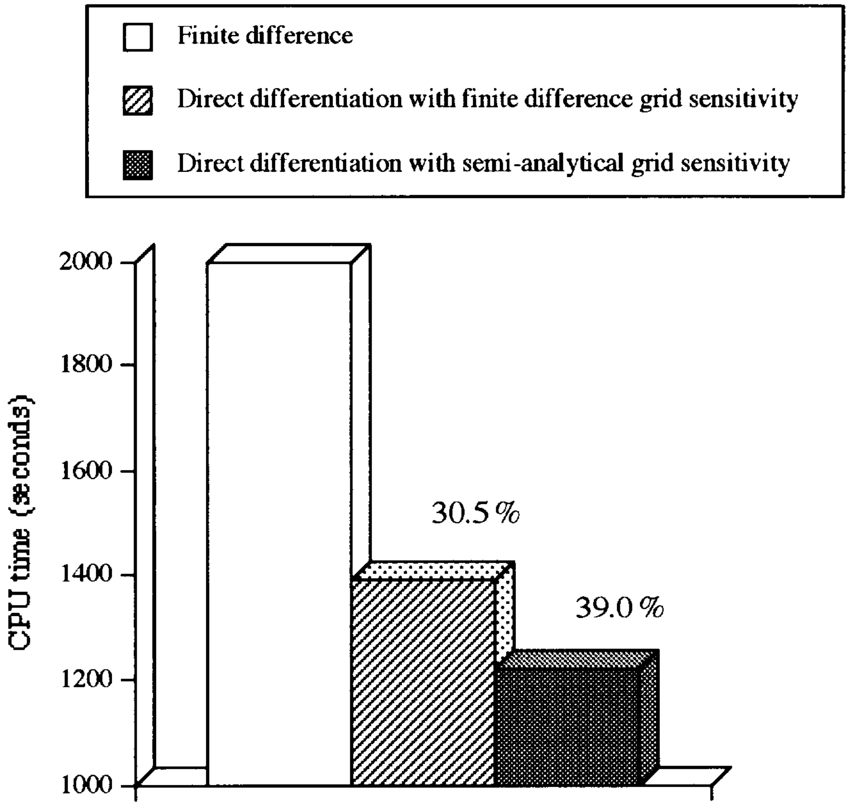

Figure 4. Comparison of CPU time for aerodynamic sensitivity analysis.

4. Optimization Techniques

The multidisciplinary optimization procedure for the design of aerospace systems such as high speed wing-body configurations requires the integration of several major disciplines. Since an "all-at-once" approach in such cases is complex and inefficient, the problem is formulated using a non-hierarchical, multilevel decomposition technique. In general, the optimization problem at each level involves several objective functions, constraints and design variables. In the present work, two different multiobjective formulation techniques have been used. These are the Kreisselmeier-Steinhauser (K-S) function [106-107] approach and the modified global criteria [13] technique. At levels where the K-S function approach is used, the Broyden-Fletcher-Goldfarb-Shanno (BFGS) algorithm [108] is used to solve the unconstrained nonlinear optimization problem. At levels where a single objective function is involved, a nonlinear constrained optimization algorithm based on the method of feasible directions [109-110] is used. At each level, the optimization procedure is coupled with an approximate analysis technique based on a two-point exponential expansion [111] thus making the overall procedure computationally efficient. The following sections describe these procedures.

4.1 Multilevel Decomposition

The formulation of a MDO problem using a two-level procedure is illustrated in Fig. 5. For example, in the case of an integrated aerodynamic and structural optimization of high speed aircraft, level 1 may optimize aerodynamic criteria and level 2 may address structural criteria [92-93, 100-101].

Each level is characterized by a multiobjective optimization problem with vectors of objective functions, constraints and design variables. The formulation is outlined below.

Level 1

$$\text{Minimize} \quad F_i^1(\mathbf{\Phi}^1) \qquad i = 1, \cdots, NOBJ^1$$

$$\text{subject to} \quad g_k^1(\mathbf{\Phi}^1) \le 0 \qquad k = 1, \cdots, NC^1$$

$$\sum_{i=1}^{NDV^1} \frac{\partial F_j^{2^*}}{\partial \phi_i^1} \Delta\phi_i^1 \le \varepsilon_{2j} \qquad j = 1, \cdots, NOBJ^2$$

$$\phi_i^{1L} \le \phi_i^1 \le \phi_i^{1U} \qquad i = 1, \cdots, NDV^1$$

$$\phi_j^{2L} \le \phi_j^{2^*} + \sum_{i=1}^{NDV^1} \frac{\partial \phi_j^{2^*}}{\partial \phi_i^1}\Delta\phi_i^1 \le \phi_j^{2U} \qquad j = 1, \cdots, NDV^2$$

where $\mathbf{F}^1$ and $\mathbf{F}^2$ are the objective function vectors at levels 1 and 2, respectively. The corresponding constraint vectors are $\mathbf{g}^1$ and $\mathbf{g}^2$ and the corresponding design variable vectors are $\mathbf{\Phi}^1$ and $\mathbf{\Phi}^2$. The quantity ε_j^2 represents a tolerance on the changes to the jth objective function of level 2, during level 1 optimization. Superscripts L and U refer to lower and upper bounds, respectively and the superscript (*) represents optimum values. The quantities $\frac{\partial F_j^{2^*}}{\partial \phi_i^1}$ are the optimal sensitivity derivatives of the objective functions of level 2 with respect to the design variables at level 1. The quantities $\frac{\partial \phi_j^{2^*}}{\partial \phi_i^1}$ represent the optimal sensitivity derivatives of the design variables at level with respect to the design variables at level 1.

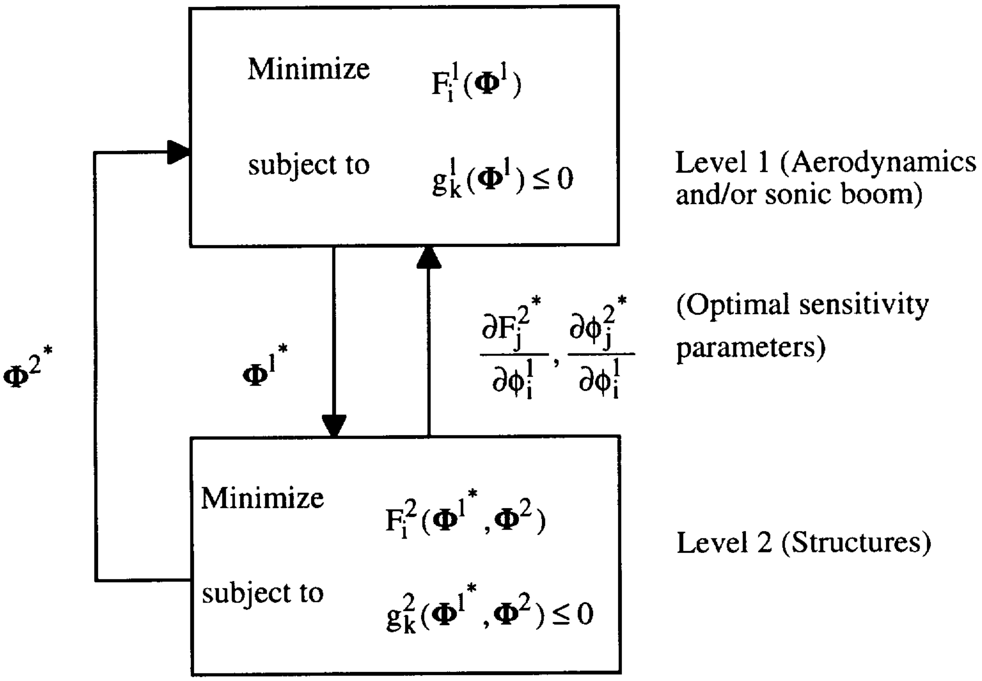

Figure 5. Two-level decomposition (schematic).

Level 2

Minimize $\quad F_i^2(\mathbf{\Phi}^{1^*}, \mathbf{\Phi}^2) \qquad i = 1, \cdots, NOBJ^2$

$$\text{subject to} \quad g_k^2(\Phi^{1^*}, \Phi^2) \le 0 \qquad k = 1, \cdots, NC^2$$

$$\phi_i^{2L} \le \phi_i^2 \le \phi_i^{2U} \qquad i = 1, \cdots, NDV^2$$

where Φ^{1*} is the optimum design variable vector from level 1. This vector is held fixed during optimization at level 2. The optimization procedure cycles through the two-levels before global convergence is achieved. A cycle is defined as one complete sweep through all the levels of optimization. Optimization at an individual level also requires several iterations before local convergence is achieved. The different levels are linked through the use of optimal sensitivity parameters which are essential in maintaining proper interdisciplinary coupling.

4.2 Multiobjective Formulations

In general, a subproblem within a multilevel optimization procedure, as described above, involves multiple objective functions and constraints. Since traditional optimization techniques address problems with a single objective function, it is essential to use formal multiobjective formulation techniques for such applications. In this research, two multiobjective formulation techniques namely, the Kreisselmeier-Steinhauser (K-S) function approach and the modified global criteria technique, have been used. The following sections describe these two formulations in detail.

4.2.1 Kreisselmeier-Steinhauser (K-S) Function Approach

The Kreisselmeier-Steinhauser (K-S) function approach [106-107] has been successfully used in various aircraft design applications [96-101]. In this approach, the original objective functions are scaled into reduced objective functions. Depending on whether the individual objective functions are to be minimized or maximized, these reduced objective functions assume one of the two following forms

$$F_k^*(\Phi) = \frac{F_k(\Phi)}{F_{k_o}} - 1.0 - g_{max} \le 0 \qquad k = 1, \ldots, NOBJ_{min} \quad (32a)$$

$$F_k^*(\Phi) = 1.0 - \frac{F_k(\Phi)}{F_{k_o}} - g_{max} \le 0, \qquad k = 1, \ldots, NOBJ_{max} \quad (32b)$$

where F_{k_o} represents the original value of the kth objective function (F_k) calculated at the beginning of each cycle and Φ is the design variable vector. g_{max} represents the largest constraint in the original constraint vector, $g_j(\Phi)$, and is held constant during each cycle. The reduced objective functions are analogous to constraints. Therefore, a new constraint vector, $f_m(\Phi)$ ($m = 1, 2, \cdots, M$ where $M = NC + NOBJ$), that includes the original constraints and the reduced objective functions (Eqs. 32a or 32b), is introduced. The design variable vector remains unchanged. The new objective function to be minimized is defined using the K-S function as follows

$$F_{KS}(\Phi) = f_{max} + \frac{1}{\rho}\log_e \sum_{m=1}^{M} e^{\rho(f_m(\Phi)-f_{max})} \tag{33}$$

where f_{max} is the largest constraint in the new constraint vector $f_m(\Phi)$ and in general, is not equal to g_{max}. The composite function $F_{KS}(\Phi)$, which represents an envelope function of the original objective functions and constraints, can now be minimized using a suitable unconstrained optimization technique.

An example of how the K-S function formulation works is illustrated in Figs. 6a and 6b for an optimization problem with two objective functions to be minimized and one constraint. The objective functions and the constraint are functions of single design variable, ϕ. An initial design point of $\phi_o = 0.5$ is used in the example. At this point, the constraint is satisfied and, therefore, g_{max} is negative. The original constraint and the two additional constraints from the two reduced objective functions, calculated from Eq. 32a, are shown in Fig. 6b along with the K-S function envelopes for two different values of ρ. Since g_{max} is negative, the constraints due to the two reduced objective functions are positive and hence, violated, at the initial design point, ϕ_o. It is seen in Fig. 6b that for $\rho = 1$, the K-S function includes contributions from all the three constraints. For a larger value of $\rho = 3$, the K-S function gets a stronger contribution from the largest constraint and weaker contributions from the other two. Thus large values of ρ "draw down" the K-S function closer to the value of the largest constraint. The value of ρ may change from cycle to cycle. It is progressively increased so that, as the optimization proceeds, the K-S function more closely represents only the largest constraint (or the most violated reduced objective function).

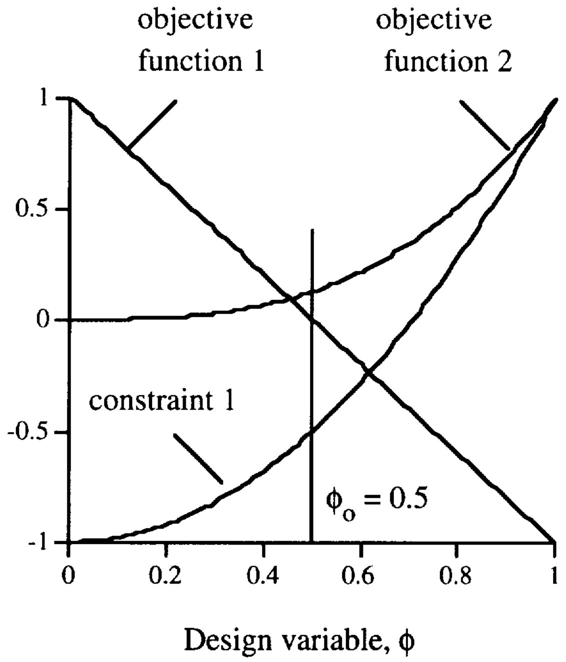

Figure 6a. Original objective functions and constraints.

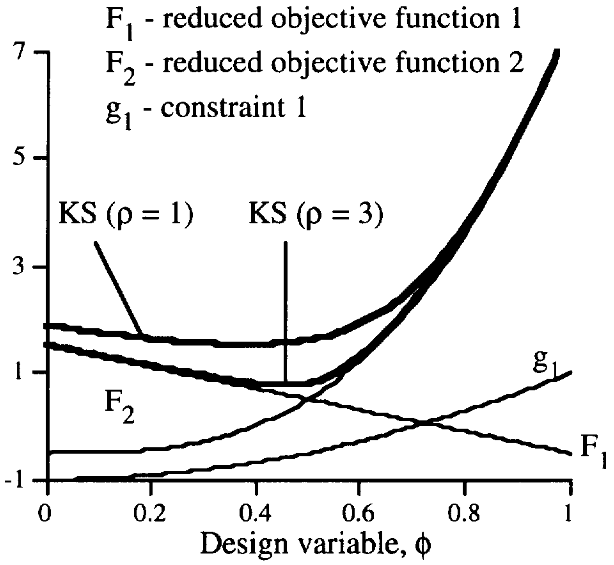

Figure 6b. K-S function envelope.

4.2.2 Modified Global Criteria Approach

The modified global criteria approach [13] is an alternate way to formulate multiobjective problems. In order to understand this approach, consider a problem with two objective functions, $f_1(\Phi)$ and $f_2(\Phi)$. Let $\bar{f}_1$ and $\bar{f}_2$ be their corresponding individually optimized values or known target values. The two original objective functions are combined into the global criteria function, $F(\Phi)$, as follows.

$$F(\Phi) = \sqrt{(f_1 - \bar{f}_1)^2 + (f_2 - \bar{f}_2)^2} \tag{34}$$

The global criteria function, $F(\Phi)$, represents the new objective function which is to be minimized. The minimization of $F(\Phi)$ forces the values of f_1 and f_2 towards their target values.

4.3 Approximate Analysis

The optimization techniques used in this research are gradient-based and they require evaluations of the objective functions and constraints during every iteration of optimization. Since it is computationally expensive to evaluate these functions through exact analysis all the time, an approximate analysis technique is used within each iteration of the optimization. The two-point exponential approximation technique developed by Fadel et al. [111], has been found to be well suited for nonlinear optimization problems and has been used in the present research for approximating the objective functions and the constraints within the optimizer. The technique is formulated as follows.

$$\hat{F}(\Phi) = F(\Phi_1) + \sum_{n=1}^{NDV} \left[\left(\frac{\phi_n}{\phi_{1_n}} \right)^{p_n} - 1.0 \right] \frac{\phi_{1_n}}{p_n} \frac{\partial F}{\partial \phi_n}(\Phi_1) \tag{35}$$

where $\hat{F}_k(\Phi)$ is the approximation to the objective function F_k at a neighbouring design point Φ, based on its values and its gradients at the current design point Φ_1 and the previous design point Φ_0. The approximate values for the constraints, $\hat{g}_j(\Phi)$, are calculated in a similar fashion. The exponent p_n, in Eq. 35 is defined as:

$$p_n = \frac{\log_e\left\{\frac{\partial F}{\partial \phi_n}(\Phi_0)\right\} - \log_e\left\{\frac{\partial F}{\partial \phi_n}(\Phi_1)\right\}}{\log_e\left\{\phi_{0_n}\right\} - \log_e\left\{\phi_{1_n}\right\}} + 1.0 \tag{36}$$

The exponent p_n explicitly determines the trade-offs between traditional and reciprocal Taylor series based expansions (also known as a hybrid approximation technique). In the limiting case when $p_n = 1$, the expansion is identical to the first order Taylor series and when $p_n = -1$, the two-point exponential approximation reduces to the reciprocal expansion form. In the present work, the exponent is defined to lie within this interval, $-1 \leq p_n \leq 1$. If the exponent p_n is greater than 1, it is set equal to one and if p_n is less -1, it is set equal to -1. Equations 35 and 36 indicate that many singularity points may exist in the use of this method and hence, care must be taken to avoid such points. In the present study, when singularity problems arise, the approximation technique is reduced to the linear Taylor series expansion ($p_n = 1$).

5. Applications of Multidisciplinary Design Optimization

A significant aspect of this research has been the development and application of MDO procedures for aerospace designs. Several different MDO procedures have been developed. The first example optimizes a theoretical, minimum drag body of revolution. This procedure is similar to the optimization study conducted by Cheung et al. [78] and serves as a benchmark test for the optimizer. The second example addresses the integrated aerodynamic/structural optimization of high speed, delta wing-body configurations. The two-level decomposition technique described earlier has been used in this application. The third MDO procedure has been used for the coupled aerodynamic and sonic boom optimization of high speed wing-body configurations in a single level. The K-S function multiobjective formulation technique is employed within this application. The fourth MDO procedure has been developed using a two-level decomposition technique for high speed wing-body design where aerodynamic and sonic boom criteria are improved in level 1 and structural criteria are optimized in level 2. These four MDO procedures use the computationally intensive CFD solver, UPS3D [90], for aerodynamic analysis. Hence, the semi-analytical sensitivity analysis techniques for calculating aerodynamic design sensitivities are used for these four MDO procedures.

5.1 Aerodynamic Optimization of a Theoretical Minimum Drag Body

The first optimization procedure is applied to a body of revolution to minimize its wave drag. The reference geometry used is the Haack-Adam (H-A) body [117-118]. This is a body of revolution with a pointed nose and a base of finite area (Fig. 7). The H-A body has minimum drag amongst all bodies in its class, according to slender-body theory for linearized, supersonic flows [117-118]. In the present research, the minimization of the wave drag coefficient (inviscid, no lift case) of the H-A body is carried out as a benchmark test. Results obtained are compared with those obtained in Ref. 78.

5.1.1 Haack-Adam (H-A) Body

The H-A body (Fig. 7) is an axisymmetric body whose radius, r, varies with the axial coordinate, x, as follows.

$$\frac{r^2}{r_{max}^2} = \frac{A_{base}}{\pi A_{max}} \left\{ \left(\pi - \theta + \frac{1}{2}\sin 2\theta \right) + \gamma_1 \frac{4}{3}\sin^3\theta + \sum_{m=2}^{\infty} \gamma_m \left(\frac{\sin(m)\theta}{m} - \frac{\sin(m+2)\theta}{m+2} \right) \right\} \tag{43}$$

where

$$\theta = \cos^{-1}\left(\frac{2x}{l_b} - 1 \right) \tag{44}$$

In the above equations, A_{base} is the base area of the H-A body, A_{max} is the cross-sectional area at the section of maximum thickness (x_{max}) and l_b denotes the length of the body. The wave drag is non-dimensionalized by the product of the freestream dynamic pressure and the maximum cross-sectional area (A_{max}). The resulting wave drag coefficient (C_{D_w}), from slender body theory, is given by

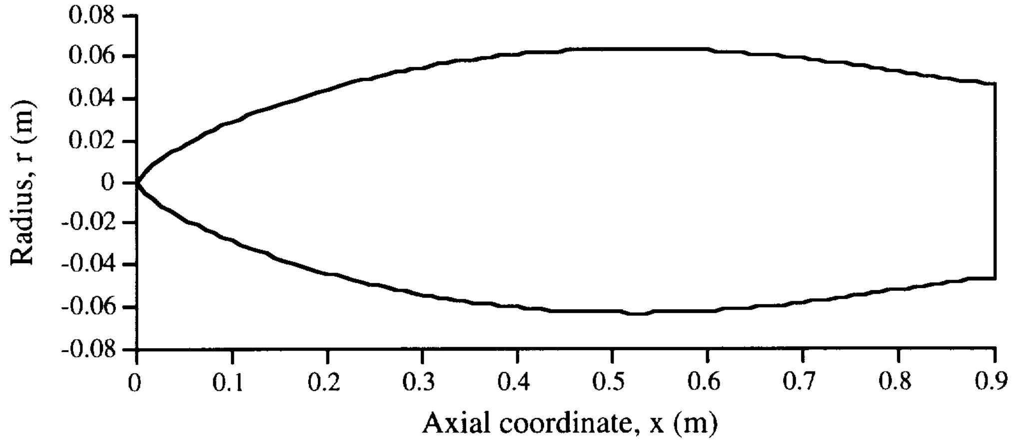

Figure 7. Haack-Adam body.

$$C_{D_w} = \frac{\pi l_b^2}{4A_{max}} \left\{ \left(\frac{4A_{base}}{\pi l_b^2} \right)^2 + \sum_{m=1}^{\infty} (m+1) \left(\frac{4A_{base}}{\pi l_b^2} \gamma_m \right)^2 \right\} \tag{45}$$

By definition, a H-A body satisfies the conditions that 1) the base area, A_{base}, is fixed and non-zero, 2) the slope at the end, $(dA/dx)^{l}{}_{x=l_b}$, is zero and 3) the location of the maximum thickness, x_{max}, is fixed. It can be verified that Eq. 43 satisfies the first two conditions automatically. The third condition determines the value of γ_1 to be,

$$\gamma_1 = \frac{1}{2\cos\theta_{max}} = \frac{l_b}{2(2x_{max} - l_b)} \tag{46}$$

The wave drag coefficient is independent of the freestream Mach number because the H-A body satisfies the condition that the slope of the area at the end, $(dA/dx)|_{x=l_b}$, is zero. From Eq. 45, it is clear that, for a body with minimum wave drag, $\gamma_m = 0$ for $m \geq 2$.

5.1.2 Results and Discussion

In the present research, the optimization of the H-A body is initiated with identical geometric parameters as reported in Ref. 78. The length of the H-A body (l_b) = 0.9 m and the fineness ratio ($l_b/2r_{max}$) = 7. The location of the maximum thickness (x_{max}) = 0.525 m and the corresponding value of theta (θ_{max}) = $\cos^{-1}(1/6)$. The ratio of the base area to the maximum area (A_{base}/A_{max}) = 0.532. Condition 3 requires the H-A body to satisfy $(dA/dx)|_{x=x_{max}} = 0$. In the present research, this slope has been allowed to change in such a way that $-1 \leq (dA/dx)|_{x=x_{max}} \leq 1$. This condition is expressed as follows.

$$\left| \begin{array}{l} -2\sin^2\theta_{max} + 4\gamma_1 \sin^2\theta_{max}\cos\theta_{max} + \\ \sum_{m=2}^{\infty} \gamma_m \left\{ \cos(m)\theta_{max} - \cos(m+2)\theta_{max} \right\} \end{array} \right| \leq 1 \qquad (47)$$

Also, a constraint is imposed during the optimization to ensure that the radius of the optimal body is greater than zero. This constraint is expressed as follows.

$$\left(\pi - \theta + \frac{1}{2}\sin 2\theta \right) + \gamma_1 \frac{4}{3}\sin^3\theta + \sum_{m=2}^{\infty} \gamma_m \left(\frac{\sin(m)\theta}{m} - \frac{\sin(m+2)\theta}{m+2} \right) \geq 0 \qquad (48)$$

for all $\pi \geq \theta \geq 0$.

In the present research, five coefficients from Eq. 43, namely, $\gamma_2, \gamma_3, \ldots, \gamma_6$ have been used as design variables. The reference values of these five coefficients are zeroes, corresponding to the theoretical minimum wave drag H-A body (Eq. 45). The wave drag coefficient (C_{D_w}) is used as the objective function to be minimized subject to two constraints, given by Eqs. 47 and 48. The optimization is carried out at a free stream Mach number of 2.5 and angle of attack of zero degrees. The flow analysis is performed using the UPS3D solver [90-91] and the inviscid option has been used to obtain the wave drag coefficient. The computational grid uses 21 points in the circumferential (η) direction, 70 points in the normal (ζ) direction and a maximum marching step size of 0.0009 m. Table 4 presents the reference and optimum values of the design variables and the wave drag coefficient. In Table 4, column 2 reproduces the optimum values obtained by Cheung et al. [78] and column 3 gives the optimum values obtained from the present research. The developed procedure yields a 6.6 percent reduction in the wave drag coefficient which is better than the 5 percent reduction achieved in Ref. 78. Figure 8 compares the drag coefficients of the reference and the optimum configurations. Clearly, the current procedure yields a better optimum than that obtained in Ref. 78. Figure 9 compares the reference and optimum configurations. The optimum body has a reduced radius distribution in the nose region compared to the reference geometry, in order to reduce the wave drag coefficient. However, the radius of the aft increases in the optimum configuration in order to satisfy the two constraints imposed during the optimization (Eqs. 47 and 48). Similar trends are observed in the optimum geometry obtained in Ref. 78.

Table 4. Comparison of design variables and objective function.

Design variables and performance function	Reference (Haack-Adam body)	Optimum (Cheung)	Optimum (present)
γ_2	0.00000	0.85300	0.73866
γ_3	0.00000	0.67300	0.45117
γ_4	0.00000	0.49500	0.27602
γ_5	0.00000	0.42000	0.38728
γ_6	0.00000	0.08460	0.15854
Drag coefficient, C_D	0.07599	0.07220 (-5.0 %)	0.07095 (-6.6 %)

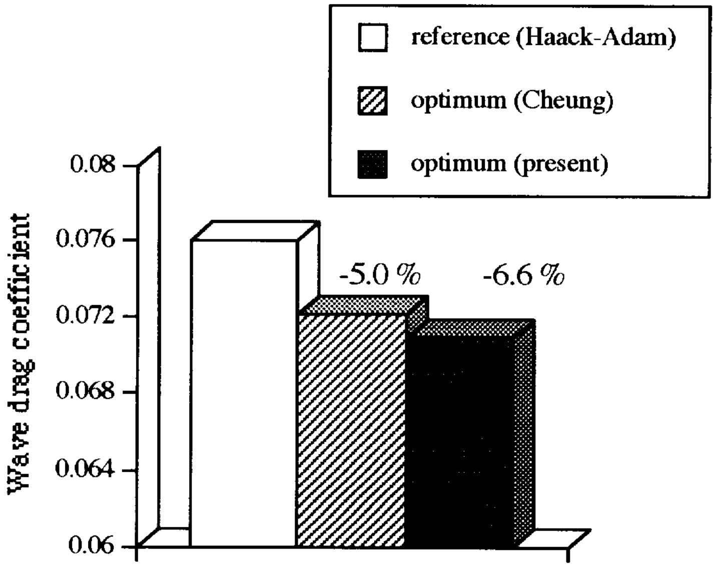

Figure 8. Comparison of wave drag coefficient (C_{D_w}).

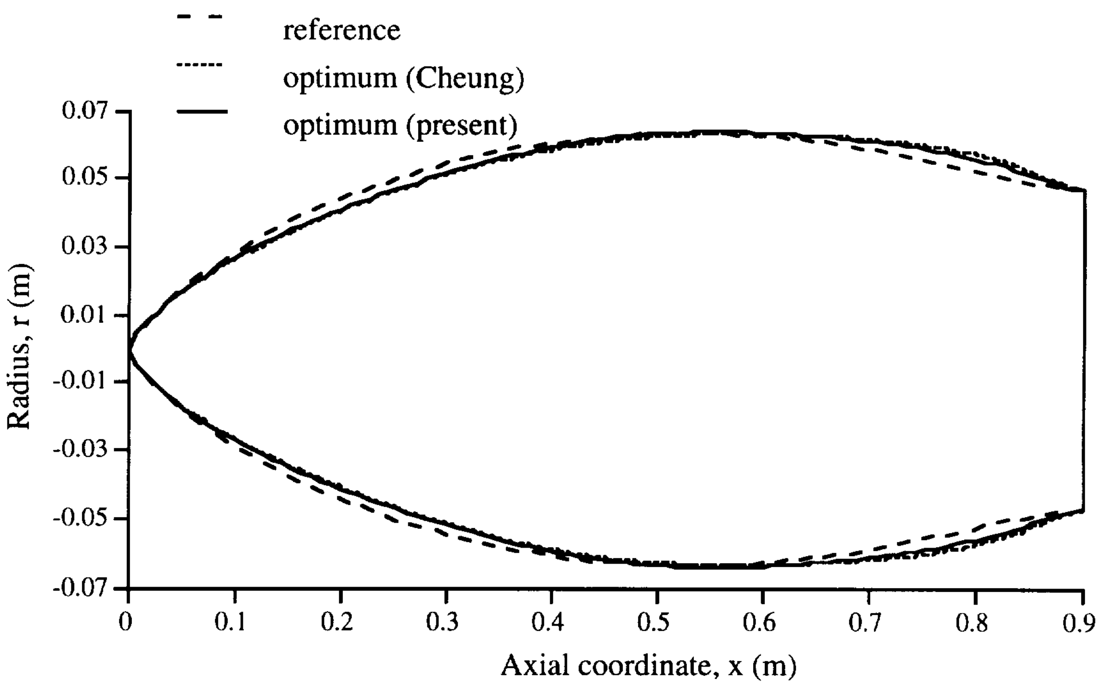

Figure 9. Comparison of reference and optimum body configurations.

5.2 Multidisciplinary Optimization of High Speed Wing-Body Configurations

The second MDO procedure developed in this research uses a two-level decomposition technique that addresses the simultaneous improvement of aerodynamic and structural performance of high speed wing-body configurations [92-93]. From aerodynamics point of view, the drag coefficient (C_D) must be minimized while maintaining the lift coefficient (C_L) above a desired value. From a structural perspective, the aircraft weight (W) must be minimized while maintaining the stresses in the load carrying members within allowable limits. These requirements are formulated as a two-level optimization problem as follows.

5.2.1 Multilevel Optimization Formulation

In a typical aircraft design, the aerodynamic performance criteria dictate the planform geometry of the aircraft wing. After designing the planform, the wing load carrying member is designed to carry the loads arising from aerodynamics, inertia and gravity. Keeping this in mind, the two-level optimization procedure improves the wing-body aerodynamic performance at level 1 and the structural performance at level 2. These optimization problems are stated as follows.

Level 1 (Aerodynamics)

Minimize

Drag coefficient (C_D)

subject to the constraints

$$C_L \geq C_{L_{min}} \qquad \text{(Lift coefficient constraint)}$$

$$W \leq W^* \qquad \text{(Optimal weight constraint)}$$

$$\phi_{j2}^L \leq \phi_{j2}^* + \sum_{i=1}^{NDV1} \frac{\partial \phi_{j2}^*}{\partial \phi_{i1}} \Delta\phi_{i1} \leq \phi_{j2}^U \qquad j = 1..NDV_2 \qquad \text{(Side constraints)}$$

$$\phi_{i1}^L \leq \phi_{i1} \leq \phi_{i1}^U \quad i = 1..NDV_1 \qquad \text{(Side constraints)}$$

where ϕ_1 denotes the vector of aerodynamic design variables, ϕ_2 denotes the structural design variable vector, NDV_1 and NDV_2 denote the number of aerodynamic and structural design variables respectively and the superscripts L and U denote lower and upper bounds on the design variables respectively.

Level 2 (Structures)

Minimize

Weight (W)

subject to the constraints

$$\sigma \leq \sigma_{all} \qquad \text{(Stress constraints)}$$

$$\phi_{i2}^L \leq \phi_{i2} \leq \phi_{i2}^U \quad i = 1..NDV_2 \qquad \text{(Side constraints)}$$

where σ is the vector of stresses at aircraft wing root and σ_{all} is the corresponding vector of material limits. During the structural optimization at the second level, the aerodynamic design variables of level 1 (ϕ_1) are held fixed at their optimum values. The quantities, $\frac{\partial W^*}{\partial \phi_{i1}}$ and $\frac{\partial \phi_{j2}^*}{\partial \phi_{i1}}$ are the sensitivities of the optimum values of the second level (structural) objective function and the design variables with respect to first level (aerodynamic) design variables. These optimal sensitivity derivatives provide the necessary coupling between the two disciplines.

5.2.2 Wing-Body Configuration

The two-level procedure and the semi-analytical sensitivity analysis techniques are applied to the design optimization of the delta wing-body configuration illustrated in Fig. 2. The description of the delta wing-body configuration has been presented earlier. The values of the parameters describing the delta wing-body configuration are: wing root chord (c_o) = 7.08 m, leading edge sweep (λ) = 66.0 degrees, wing span (w_s) = 3.53 m, wing thickness-to-chord ratio (t_c) = 0.052, maximum radius (r_m) = 0.57 m, nose length (l_n) = 6.01 m, wing starting location (x_w) = 8.21 m and body length (l_b) = 17.52 m. This reference design has been used in Ref. 120 for sonic boom prediction and comparison with wind-tunnel data. The wing leading edge sweep (λ), root chord (c_o), wing span (w_s) and thickness-to-chord ratio (t_c) are used as design variables in level 1 optimization and hence, change from their reference values during optimization. The rest of the planform parameters of the delta wing-body are held fixed throughout the optimization.

5.2.3 Wing Structural Model

In this study, a simple structural model has been used. The wing is assumed to carry all the aerodynamic loading. The load carrying structural member of the wing is modeled as a single celled, isotropic, rectangular box beam with unequal wall thicknesses [Fig. 10]. In Fig. 10, the quantity c is the local chord length of the wing section. The beam width-to-chord ratio (w_c), horizontal wall thickness-to-chord ratio (t_w) the vertical wall thickness-to-chord ratio (t_v) are used as design variables during the structural optimization at level 2.

The wing structural analysis is performed using a code developed in-house. The code is capable of analyzing single celled isotropic box beams with rectangular cross-sections, unequal horizontal and vertical wall thicknesses and linear sweep and taper distributions. The structural analysis is initiated slightly inwards of the wing tip. This ensures that the sharp wing tip of the delta wing-body does not give rise to a singular point. The wing weight (W) is calculated as the sum of the weight of the box beam (W_{box}) and the weight of the skin (W_{skin}). The normal and shear stresses (σ) at the root section of the beam are calculated using thin wall theory [119]. The isotropic box beam and the wing skin are made of 2014-T6 Aluminum alloy. The alloy has a density of 2800 Kg/m^3, tensile yield strength of 410 MPa and a shear yield strength of 220 MPa. The reference values of structural design variables are: spar width-to-chord ratio (w_c) of 0.5, spar horizontal wall thickness-to-chord ratio (t_w) of 0.0015 and vertical wall thickness-to-chord ratio (t_h) of 0.0075.

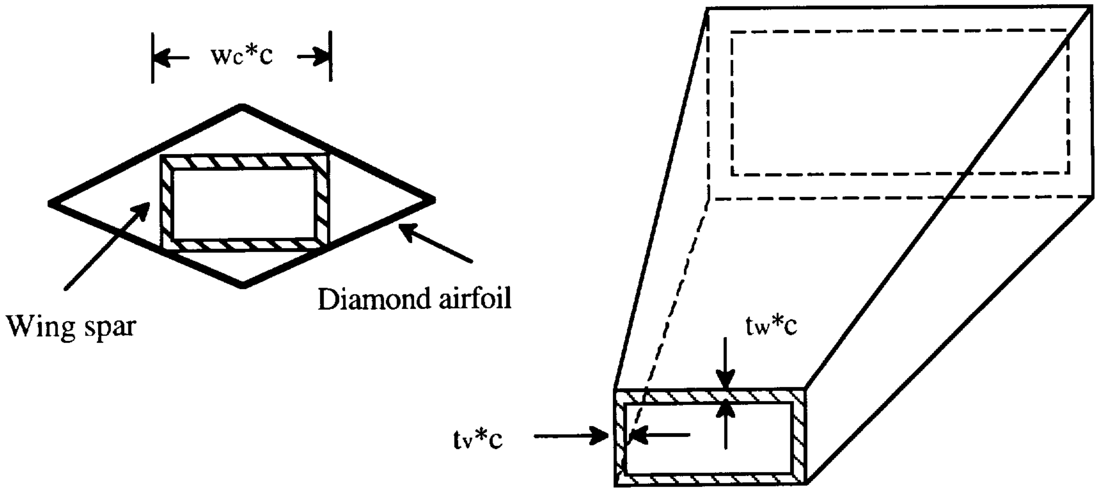

Wing spar (Box beam)

Figure 10. Wing cross-section and wing spar (box beam).

5.2.4 Results and Discussion

The optimization is performed for a cruise design Mach number of 2.5 and an angle of attack of 5 degrees. The inviscid, supersonic flow field is calculated using the CFD solver, UPS3D [90]. The inviscid drag and the lift forces are non-dimensionalized using the product of the dynamic pressure and a unit reference area, to yield a drag coefficient, denoted C_{D_u}, and a lift coefficient, denoted C_{L_u}. Though the use of a unit reference area yields high values for these non-dimensional coefficients, improvements in these coefficients directly reflect improvements in the corresponding aerodynamic forces. A maximum step size of 0.01 m is used to march in the ξ direction. The aerodynamic design sensitivities, required during the level 1 aerodynamic optimization, are calculated using the semi-analytical sensitivity analysis procedures [94-95] described before. A hyperbolic grid with 75 points in the circumferential (η) direction and 80 points in the normal (ζ) direction is used for the flow analysis. Further refinement of the grid does not alter the flow solution.

The iteration histories of the drag and the lift coefficients (C_{D_u} and C_{L_u}) of the wing-body configuration, during the level 1 aerodynamic optimization, are compared in Figs. 11 and 12, respectively. Significant improvements are observed in both the quantities. The drag coefficient decreases by 5.5 percent and the lift coefficient increases by 5.43 percent. All the increase in the lift coefficient occurs in the first iteration of the optimization after which the lift coefficient is maintained at its improved value through the rest of the optimization. The lift coefficient constraint is a violated constraint in the first cycle of optimization. The optimizer, based on the method of feasible directions, establishes feasibility by increasing the lift coefficient to its desired value, $C_{L_{min}}$, in the first cycle. Increasing the lift coefficient any further results in an associated increase in the induced drag. As a result, the optimizer maintains the lift coefficient constraint active. The constraint imposed on the weight, is well satisfied during the level 1 optimization.

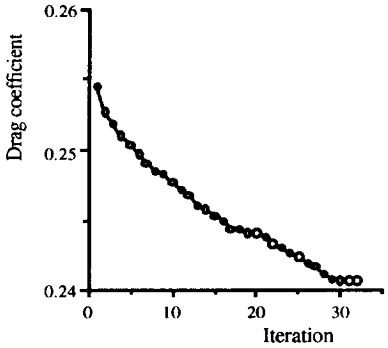

Figure 11. Iteration history of drag coefficient, (C_{D_u}).

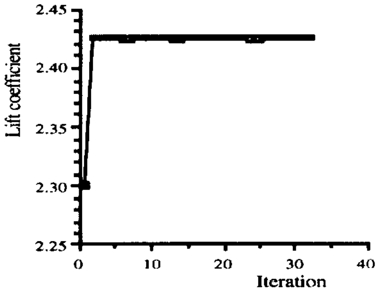

Figure 12. Iteration history of lift coefficient, (C_{L_u}).

Table 5. Aerodynamic design variables.

Design variable	Reference	Optimum
Sweep (λ)	66.00 deg.	65.33 deg.
Root Chord (c_0)	7.08 m	7.70 m
Wing Span (w_s)	3.530 m	3.617 m
Thickness-to-chord (t_c)	0.05200	0.03105

Table 5 compares the reference and the optimum values of the aerodynamic design variables used in the aerodynamic optimization. The root chord is increased significantly from its reference value

(8.76 percent), whereas the wing thickness-to-chord ratio is decreased significantly (40.29 percent). The wing span and the leading edge sweep are maintained close to their reference values (2.94 percent and 1.01 percent respectively). The reduction in the wing thickness-to-chord ratio decreases the form drag of the diamond airfoil section. The optimization is driven by this reduction in drag. The increase in the wing planform area, caused by the increase in the root chord and the wing span, helps improve the lift of the aircraft in spite of the decrease in the wing thickness-to-chord ratio. Though the drag and the lift coefficients have been non-dimensionalized using a unit reference area in this study, the optimization procedure allows a traditional non-dimensionalization using the wing planform areas.

The iteration history of the weight of the wing body configuration is presented in Fig. 13. Considerable reduction (18.13 percent) in the weight is observed. The shear and the normal stresses at the blade root remain well within the allowable limits of the chosen Aluminum alloy. Table 6 compares the reference and optimum values of the structural design variables. The spar width to chord ratio, horizontal and vertical wall thickness to chord ratios decrease significantly from their reference values (60 percent, 60 percent and 65.2 percent respectively). In spite of the increased planform area, the weight is reduced through significant reductions to the wall thicknesses and wing thickness-to-chord ratio.

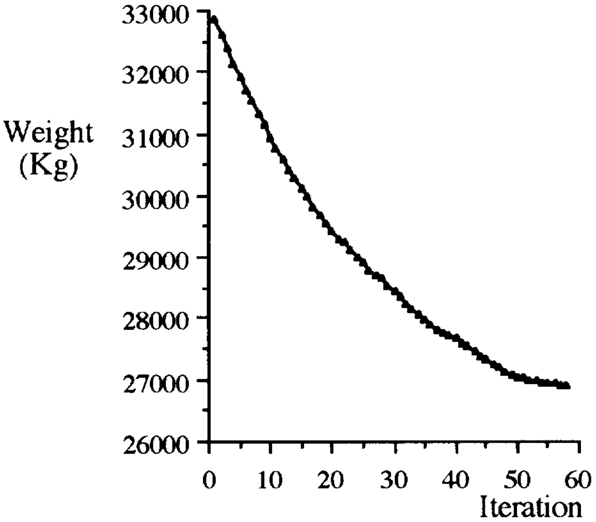

Figure 13. Iteration history of weight.

Table 6. Structural design variables.

Design variable	Reference	Optimum
Spar width-to-chord ratio (w_c)	0.5	0.2
Horizontal wall thickness-to-chord ratio (t_w)	0.0015	0.0006
Vertical wall thickness-to-chord ratio (t_v)	0.0075	0.00261

5.3 Integrated Aerodynamic/Sonic Boom Optimization

One of the desired objectives of high speed (supersonic) aircraft designs is to arrive at low sonic boom configurations. Such designs would have minimum environmental impact thus making them viable for operation over population centers. At the same time, such designs should also be able to produce optimum aerodynamic performance so that they are economically viable too. These considerations give rise to an important multidisciplinary design optimization problem requiring minimum sonic boom and maximum aerodynamic performance from the designs. In this section, an optimization procedure that has been developed to reduce the sonic boom levels of high speed wing-body configurations without deteriorating their aerodynamic performance, is described. The sonic boom of an aircraft is measured in terms of the pressure disturbances it produces at designated distances from the aircraft. The pressure disturbance at any point is given by $\Delta p = (p - p_\infty)/p_\infty$, where p is the pressure at the point of interest and p_∞ is the free stream pressure. Figure 14 presents the overpressure signature (Δp) produced by the delta wing-body configuration described in Section 3.5. The aircraft is flying at a Mach number of 2.5 and angle of attack of 5 degrees at a cruise altitude of about 16,500 m. The pressure signature is captured at the ground level (this corresponds to 941.2 times the length of the aircraft, vertically below the aircraft). The pressure signature has two positive pressure peaks and a negative peak. The first positive pressure peak (Δp_1) corresponds to the pressure jump associated with the shock wave at the nose of the aircraft. The second positive peak (Δp_2) is due to the shock wave created by the aircraft wing. The negative pressure peak corresponds to expansion waves in the flow field past the wing trailing edge. From a sonic boom perspective, it is desirable to minimize these positive pressure peaks in the overpressure signal. From aerodynamics point of view, it is of interest to minimize the aerodynamic drag to lift ratio (C_D/C_L) while maintaining the lift coefficient (C_L) at a desired level. In the following sections, the sonic boom analysis procedure and the various optimization formulations to reduce sonic boom levels of high speed wing-body configurations are presented.

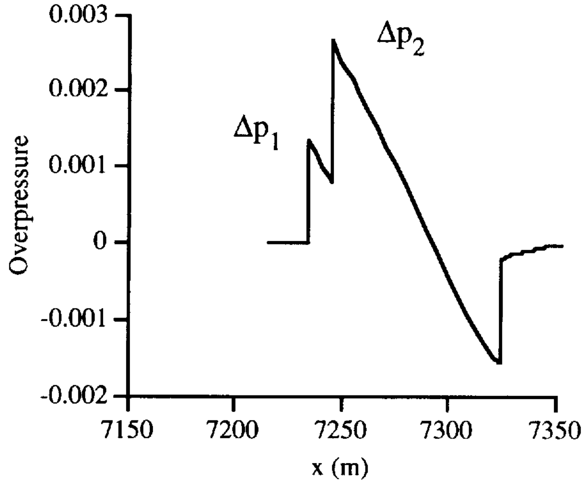

Figure 14. Sonic boom pressure signature of a supersonic wing-body configuration.

5.3.1 Sonic Boom Analysis

For isentropic flow past smooth axisymmetric bodies, the pressure disturbances (sonic boom) at large distances from the aircraft can be evaluated by using the Whitham F-function [121], which is based on the Abel integral of the equivalent area distribution of the aircraft. Lighthill [122] developed an alternate formulation of the F-function which was shown to be suitable for sonic boom prediction for projectile geometries. Walkden [123] extended Whitham's theory for application to wing-body configurations. The asymptotic forms of the equations used in developing the sonic boom overpressure signature (Δp) are as follows.

$$\begin{aligned} F(y) = & \frac{1}{2\pi}\int_0^\infty \sqrt{\frac{2}{\beta R_{vol}(t)}}\, h\left[\frac{y-t}{\beta R_{vol}(t)}\right] dS'_{vol}(t) \\ & + \frac{1}{2\pi}\int_0^\infty \sqrt{\frac{2}{\beta R_{lift}(t)}}\, h\left[\frac{y-t}{\beta R_{lift}(t)}\right] dS'_{lift}(t) \\ & + \frac{1}{2\pi}\int_0^\infty \sqrt{\frac{2}{\beta R_{int}(t)}}\, h\left[\frac{y-t}{\beta R_{int}(t)}\right] dS'_{int}(t) \end{aligned} \qquad (49)$$

$$\Delta p = \gamma M_\infty^2 F(y)/\sqrt{2\beta d_o} \qquad (50)$$

$$\beta = (M_\infty{}^2 - 1)^{0.5} \qquad (51)$$

$$\kappa = (\gamma + 1)M_\infty{}^4/[\beta^*(2\beta)^{0.5}] \qquad (52)$$

$$x = y + \beta d_o - \kappa\sqrt{d_o}F(y) \qquad (53)$$

where γ is the ratio of specific heats (1.4 for air) and M_∞ is the freestream Mach number. The first integral of Eq. 49 is associated with the volume of the flying object, the second integral is associated with the lift and the third integral is associated with the interference lift for a winged body [123]. R_{vol}, R_{lift} and R_{int} are the equivalent radii of the flying object based on its volume, lift and wing-body interference, S' is the derivative of the area distribution of the flying object and h is the Heaviside unit step function. The quantity, $y(x, d_o)$ = constant is a characteristic curve where x is the streamwise distance and d_o is the distance normal to the flight axis. Since the above models are based on linearized theory, they are inaccurate in predicting sonic boom in highly nonlinear flows such as the flow at angle-of-attack at higher Mach numbers ($M_\infty > 2$). Reference 124 describes an F-function extrapolation method to evaluate the pressure signature at a distance d_l from known pressure at distance d_o ($d_l > d_o$). The pressure signature at distance d_o, where the flowfield is assumed to be locally axisymmetric, is evaluated either by measurements in a wind tunnel or through computation and the value of the F-function is calculated from Eq. 50. Since the pressure signal propagates at the local speed of sound and each point of the signal advances according to its amplitude, the signal is distorted and the F-function becomes multivalued at a farther distance d_l. A new F-function at d_l is then obtained by placing discontinuities (shocks) in such a way that the discontinuities divide the multivalued regions with equal areas on either side of them. This new F-function gives the overpressure signature at d_l using Eqs. 50 through 53.

Cheung et al. [120] have combined Whitham's quasilinear theory with the three-dimensional PNS code, UPS3D, to predict sonic boom. The flow field associated with wing-body configurations is evaluated by UPS3D and the overpressure signal for the near field is evaluated. The overpressure signals at specified far fields are then obtained using one of three different approaches for various configurations such as a cone-cylinder, a low aspect-ratio rectangular wing and a delta wing-body. In the first approach (for nonlifting cases), the UPS3D code is modified so as to incorporate a sonic boom prediction capability including all nonlinear effects. The second approach is applicable to both lifting and nonlifting cases. In this approach, the extrapolation method described earlier [124] has been used for predicting sonic boom. In the third approach (for lifting cases), the equivalent area distribution due to lift is generated by the surface pressure coefficients calculated by the CFD solver. The equivalent area distribution due to volume is calculated from the geometry of the aircraft. Summation of the two equivalent area distributions yields the total equivalent area distribution that gives the F-function of the body.

In the present research, the second approach, based on the extrapolation technique of Ref. 124, has been used to obtain the sonic boom signatures. This extrapolation procedure has been validated by comparison with wind tunnel data in Ref. 120 by applying it to the delta wing-body configuration described in Section 3.5.

5.3.2 Sonic Boom Sensitivities

The optimization procedures used for sonic boom minimization require the sensitivities of the overpressure peaks (Δp_1 and Δp_2). The near field pressure signature, at a distance d_o, is directly calculated by the UPS3D code. The sensitivity of this near field pressure signature is part of the aerodynamic flow sensitivities calculated using the semi-analytical procedure based on the direct differentiation approach [94-95], described earlier. Using these sensitivities, perturbed near field pressure signatures are generated for each design variable. These perturbed near field signatures are then extrapolated using the sonic boom extrapolation procedure [124] to obtain perturbed far field signatures corresponding to each design variable. These perturbed far field signatures are then used to obtain the sensitivities of the pressure peaks using finite difference techniques.

5.3.3 Optimization Formulation

The multidisciplinary optimization procedure must lead to minimum sonic boom while maintaining or improving the aerodynamic performance of the aircraft. From a sonic boom perspective, it is desirable to minimize the first and the second peaks (Δp_1 and Δp_2) in the overpressure signal at a given distance, d_1, away from the aircraft. From aerodynamics point of view, the drag to lift ratio (C_D/C_L) must be minimized while maintaining the lift coefficient (C_L) at a desired level. The optimization problem can be stated as follows.

Minimize

$$\Delta p_1, \ \Delta p_2 \ \text{and} \ C_D/C_L$$

subject to the constraints

$$C_{L\min} \leq C_L \leq C_{L\max}$$

$$\Phi_{\min} \leq \Phi \leq \Phi_{\max}$$

where Φ is the design variable vector and the subscripts "min" and "max" denote lower and upper bounds, respectively. It must be noted that both upper and lower bounds have been imposed on the lift coefficient. While the lower bound ensures the prescribed minimum lifting capability, the upper bound is designed to keep the sonic boom levels from increasing. This is because, the sonic boom overpressure peaks increase in value as the lift increases [122]. Some of the optimization studies presented in the following sections, do not include the second pressure peak (Δp_2) as an objective function and, in some cases, omit the lift coefficient constraints.

5.3.4 Wing-Body Configurations

The above multiobjective optimization procedure is applied to two high speed wing-body configurations. The first configuration is the delta wing-body configuration, illustrated in Fig. 2 and described in Section 3.5. The second configuration addressed is a doubly swept wing-body configuration (Fig. 15). The doubly swept configuration is characterized by two sweep angles, λ_1 and λ_2, root chord, c_o, tip chord, c_t, break length, x_b, maximum body radius, r_m, nose length, l_n, wing starting location, x_w and total body length, l_b. The wing cross-section is a diamond airfoil with thickness-to-chord ratio, t_c. A combination of these geometric parameters forms the design variable set.

The inviscid flow field around the vehicle is evaluated using the CFD solver, UPS3D, over a flow domain that extends from the tip of the body up to three times the body length in the longitudinal direction. The pressure field at a distance $d_o = 0.5\ l_b$ measured from the axis (directly beneath the aircraft) is evaluated from the flow field solution. The sonic boom at a far field distance d_l is then evaluated using the extrapolation procedure of Ref. 124. Two specified far field distances have been considered during optimization. The first of the two corresponds to a distance $d_l = 3.61\ l_b$ from the axis of the body and is denoted "near field" in the text. The second distance considered is $d_l = 941.7\ l_b$ from the axis of the body and is denoted "far field" in the text. This far field distance corresponds to the ground level for an aircraft flying at an altitude of approximately 16,500 m. The optimization of both configurations is performed at a design cruise Mach number of 2.5 and angle of attack of 5 degrees. A hyperbolic grid with 75 points in the circumferential (η) direction and 80 points in the normal (ζ) direction is used for the flow analysis. The maximum step size for marching in the ξ direction is set to 0.01 m. The semi-analytical sensitivity analysis procedures, described before, are used to calculate the aerodynamic and sonic boom design sensitivities.

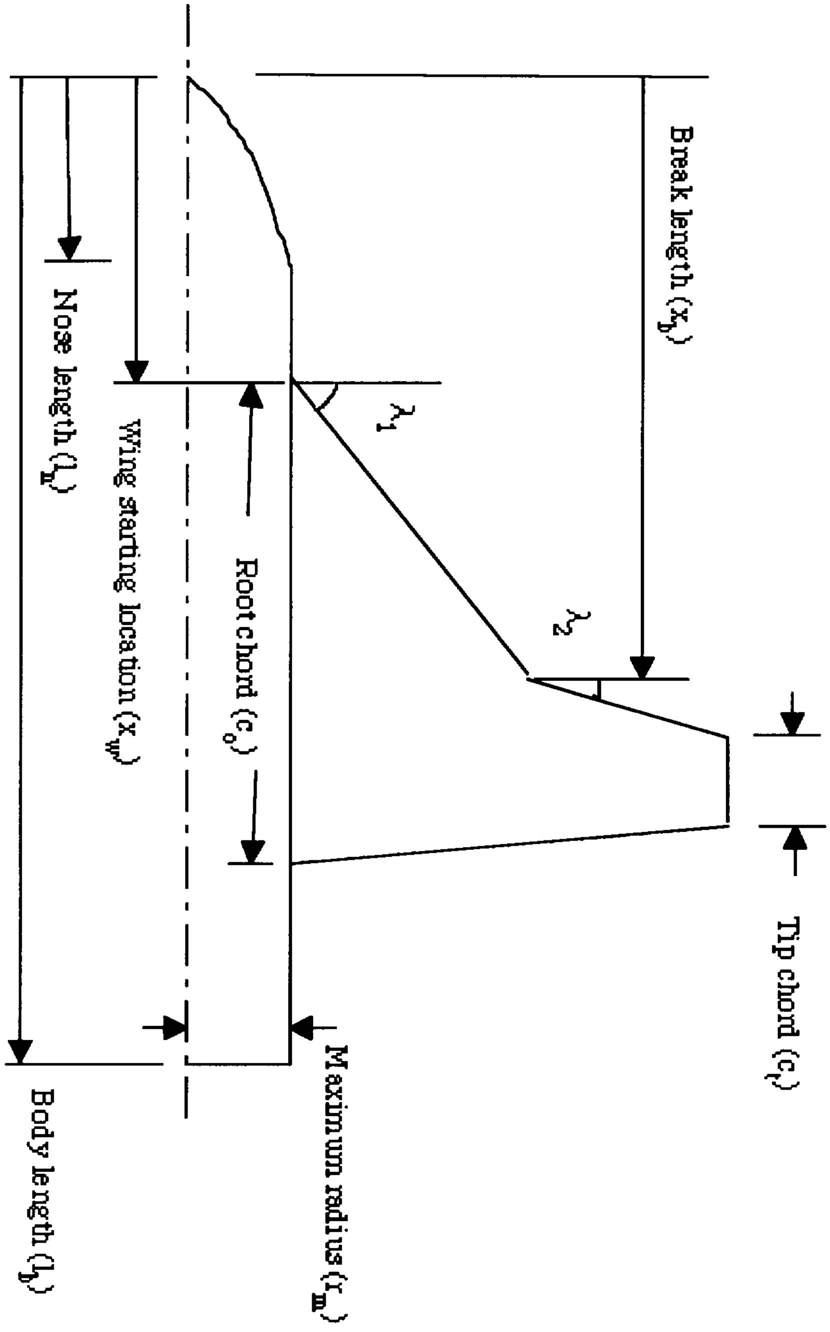

Figure 15. Doubly swept wing-body configuration (schematic).

The inviscid flow field around the vehicle is evaluated using the CFD solver, UPS3D, over a flow domain that extends from the tip of the body up to three times the body length in the longitudinal direction. The pressure field at a distance $d_o = 0.5\ l_b$ measured from the axis (directly beneath the aircraft) is evaluated from the flow field solution. The sonic boom at a far field distance d_1 is then evaluated using the extrapolation procedure of Ref. 124. Two specified far field distances have been considered during optimization. The first of the two corresponds to a distance $d_l = 3.61\ l_b$ from the axis of the body and is denoted "near field" in the text. The second distance considered is $d_l = 941.7\ l_b$ from the axis of the body and is denoted "far field" in the text. This far field distance corresponds to the ground level for an aircraft flying at an altitude of approximately 16,500 m. The optimization of both configurations is performed at a design cruise Mach number of 2.5 and angle of attack of 5 degrees. A hyperbolic grid with 75 points in the circumferential (η) direction and 80 points in the normal (ζ) direction is used for the flow analysis. The maximum step size for marching in the ξ direction is set to 0.01 m. The semi-analytical sensitivity analysis procedures, described before, are used to calculate the aerodynamic and sonic boom design sensitivities.

5.3.5 Delta Wing-Body Optimization

For the delta wing-body configuration case, the leading edge sweep (λ), the wing root chord (c_o), the wing span (w_s), the airfoil thickness-to-chord ratio (t_c), the maximum nose radius (r_m) and the nose length (l_n) are used as design variables. The reference values of the delta wing-body parameters are: wing root chord (c_o) = 7.08 m, leading edge sweep (λ) = 66.0 degrees, wing span (w_s) = 2.96 m, wing thickness-to-chord ratio (t_c) = 0.052, maximum radius (r_m) = 0.57 m, nose length (l_n) = 6.01 m, wing starting location (x_w) = 8.21 m and body length (l_b) = 17.52 m. The wing starting location (x_w) and the body length (l_b) are held constant during the optimization.

Near Field Sonic Boom Minimization ($d_l = 3.61\ l_b$)

The results from the optimization of the pressure signature at a distance of 3.61 l_b (directly below the aircraft) are presented first. Two sets of results are presented. In the first case, the optimization is performed for minimum C_D/C_L and minimum first sonic boom peak (Δp_l) with a constraint on the lift coefficient ($C_{L_{min}} \leq C_L \leq C_{L_{max}}$). In the second case, the same objectives are optimized without any lift constraint. Results from the first case are discussed first. The bounds chosen for the lift coefficient are $C_{L_{min}} = C_{L_{ref}}$ and $C_{L_{max}} = 1.02\ C_{L_{ref}}$, where $C_{L_{ref}}$ is the lift coefficient of the reference configuration. Table 7 compares the reference and the optimum values of the six design variables and the performance functions used in the optimization. Reductions are observed in the wing thickness-to-chord ratio and nose radius whereas nose length and wing root chord have increased. Small changes in the leading edge sweep and wing half span are observed. Figure 16 compares the geometries of the reference and optimum configurations. Figure 17 compares the reference and optimum values of the objective functions. The objective functions have been normalized with respect to their corresponding reference values in Fig. 17. There is a significant drop in the sonic boom level (11.1 %) for the optimum configuration. The drag-to-lift ratio has also decreased by 4.3 percent. The drag coefficient has decreased by 2.6 percent and the lift coefficient has increased by 1.8 percent for the optimized configuration. The drag force has decreased by 3.3 percent and the lift force has increased by 1.1 percent. Figure 18a presents the reference and optimum pressure distributions at $d_l = 3.61\ l_b$. The same signature extrapolated to the ground level ($d_l = 941.7\ l_b$) is presented in Fig. 18b. Clearly, the first pressure peak in these signatures (Δp_1) are smaller for the optimum configuration. However, the second pressure peak (Δp_2) has increased by 1.2 percent in the near field signature. This increase is due to the increase in the lift. It is to be noted that this second pressure peak is not an objective function in this optimization and hence, increases slightly due to the increase in the lift.

Table 7. Delta wing-body case; near field optimization with lift coefficient constraint.

Design variables and performance functions	Reference	Optimum
Root chord, c_o (m)	7.08	7.05
Leading edge sweep, λ (degrees)	66.0	64.4
Thickness to chord ratio, t_c	0.05200	0.04894
Wing half span, w_s (m)	3.53	3.4873
Nose length, l_n (m)	6.01	6.2528
Max. nose radius, r_m (m)	0.570	0.5363
First pressure peak (Δp_1)	0.033195	0.029022
Second pressure peak (Δp_2)	0.058374	0.060113
Drag-to-lift ratio, C_D/C_L	0.11681	0.11178
Drag coefficient, C_D	0.02446	0.02383
Lift coefficient, C_L	0.20940	0.21318
Drag force (N)	16539.6	16000.6
Lift force (N)	141594.1	143144.3

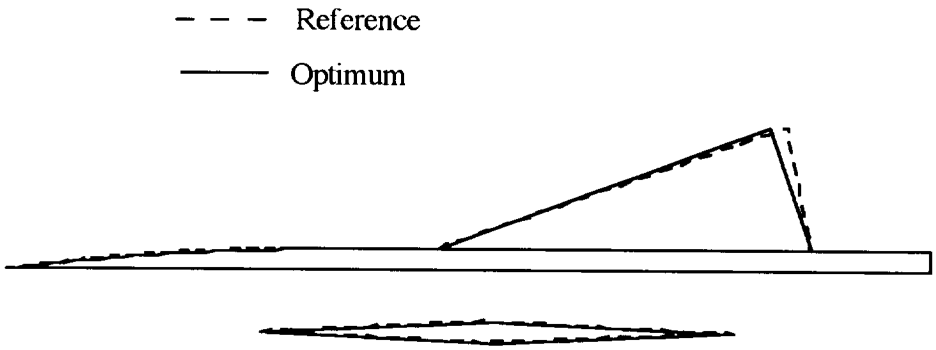

Figure 16. Comparison of geometries; near field optimization with lift coefficient constraint.

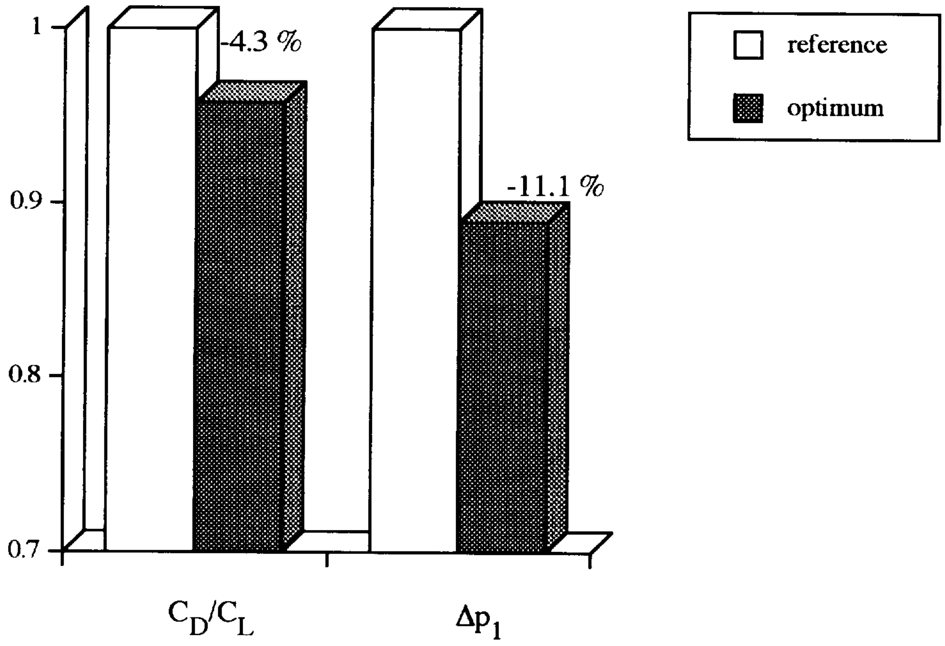

Figure 17. Comparison of objective functions; near field optimization with lift constraint.

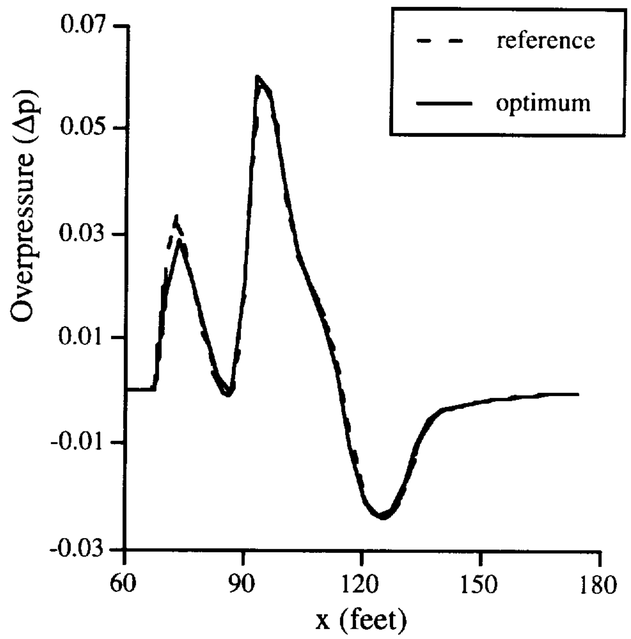

Figure 18a. Comparison of pressure signatures; near field optimization with lift constraint; d_l = 3.61 l_b.

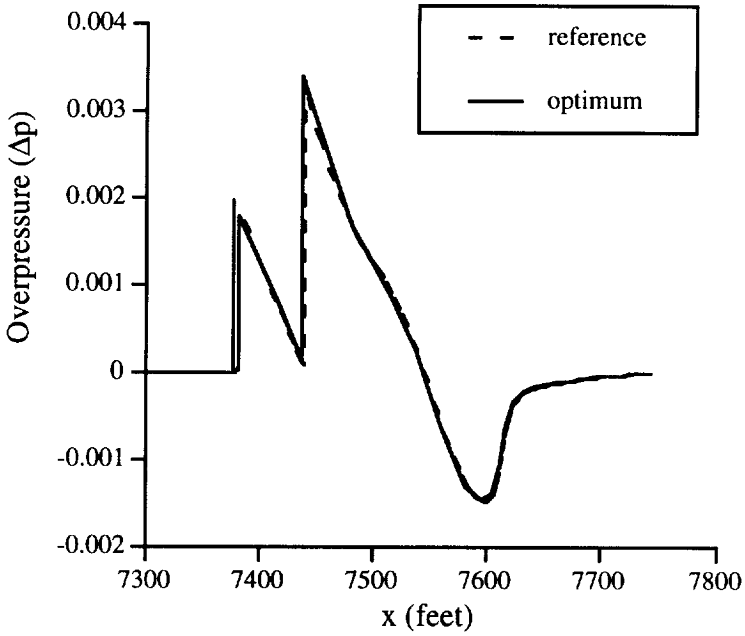

Figure 18b. Comparison of pressure signatures; near field optimization with lift constraint; extrapolated to ground level (d_l = 941.7 l_b).

Table 8 summarizes the results for the second case where optimization is performed for minimum C_D/C_L and minimum sonic boom (Δp_l) without any constraint on the lift coefficient.

Similar to the previous case, the wing thickness-to-chord ratio and nose radius have decreased whereas the nose length and wing root chord have increased. Small changes in the leading edge sweep and wing half span are observed. Figure 19 compares the geometries for the reference and the optimum configurations. Figure 20 present the reference and optimum values of the normalized objective functions. The first peak in the pressure signature has decreased significantly (21.5 %) for the optimum configuration. The drag-to-lift ratio has also decreased by 7.6 percent and the drag coefficient has decreased by 12.8 percent. There is also a 5.6 percent decrease in the lift coefficient of the optimized configuration. The drag force has decreased by 12.9 percent and the lift has reduced by 5.8 percent.

Table 8. Delta wing-body case; near field optimization without lift coefficient constraint.

Design variables and performance functions	Reference	Optimum
Root chord, c_o (m)	7.08	7.63
Leading edge sweep, λ (deg)	66.0	69.1
Thickness to chord ratio, t_c	0.05200	0.04680
Wing half span, w_s (m)	3.530	3.254
Nose length, l_n (m)	6.01	6.611
Max. nose radius, r_m (m)	0.570	0.513
First pressure peak (Δp_1)	0.033195	0.026042
Second pressure peak (Δp_2)	0.058739	0.052679
Drag-to-lift ratio, C_D/C_L	0.11681	0.10790
Drag coefficient, C_D	0.02446	0.02133
Lift coefficient, C_L	0.20940	0.19771
Drag force (N)	16539.6	14395.8
Lift force (N)	141594.1	133413.1

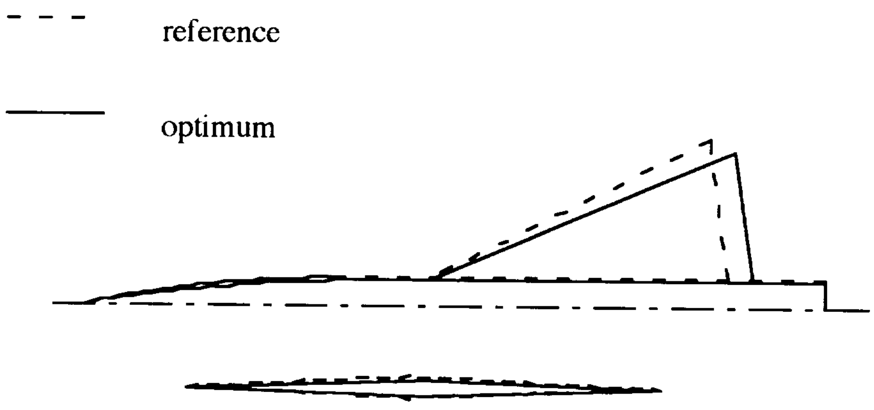

Figure 19. Comparison of geometries; near field optimization without lift constraint.

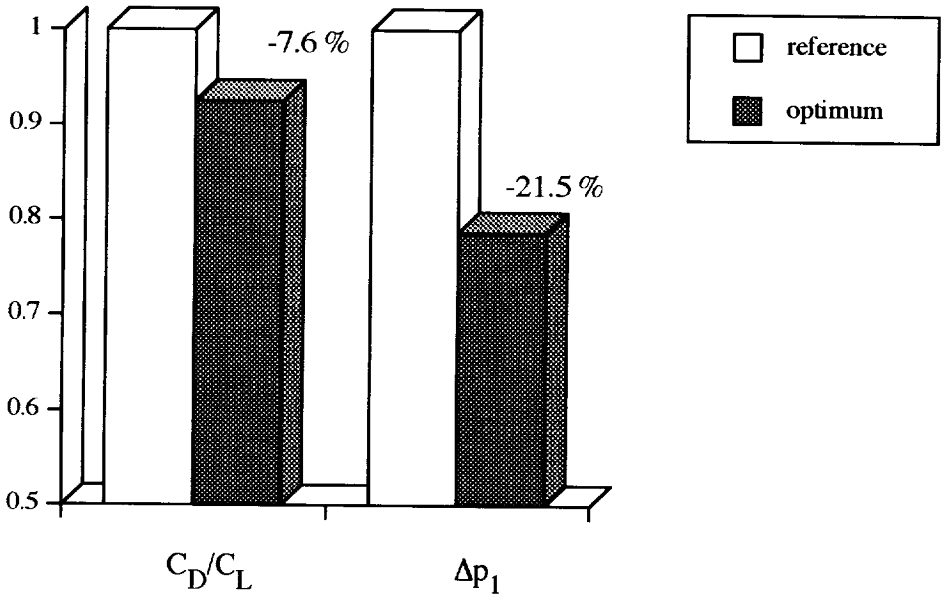

Figure 20. Comparison of objective functions; near field case without lift constraint.

Figure 21a presents the reference and optimum overpressure distributions at $d_l = 3.61\ l_b$ and Fig. 21b presents the corresponding signatures extrapolated to ground level ($d_l = 941.7\ l_b$). The reductions in both the peaks of the pressure signature for the optimum configuration are seen. The changes to the geometric parameters, especially the aircraft nose parameters and the wing thickness-to-chord ratio, cause the reductions in the sonic boom overpressure and the drag coefficient. The reduction in the lift force is also due to the small decrease in the wing planform area.

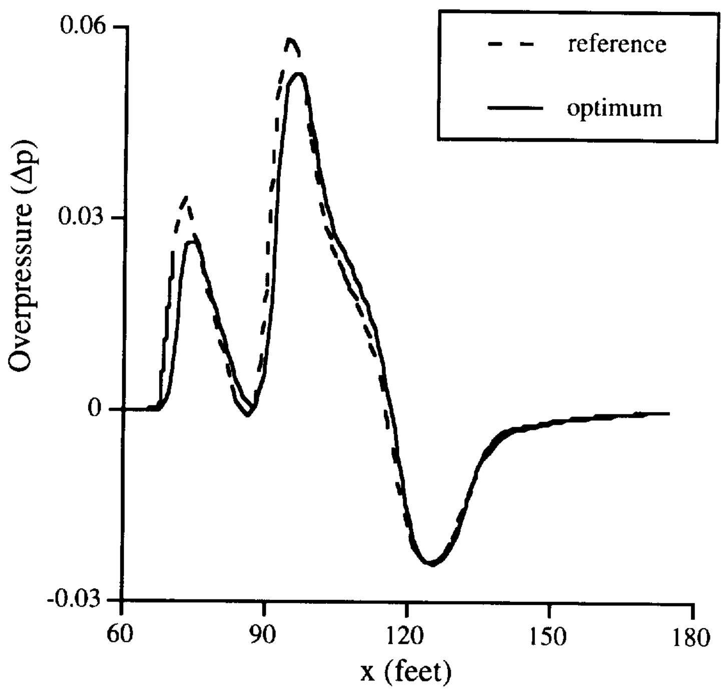

Figure 21a. Comparison of pressure signatures; near field case without lift coefficient constraint; $d_l = 3.61\ l_b$.

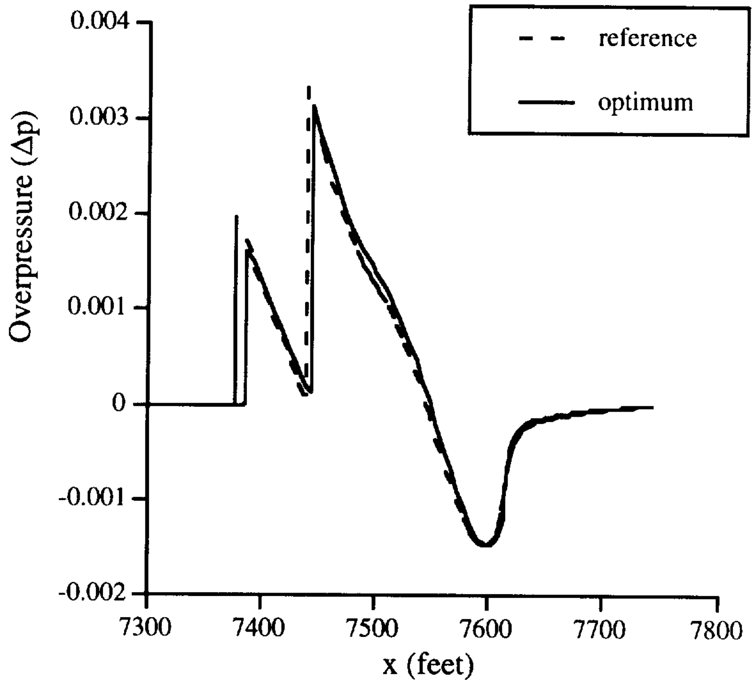

Figure 21b. Comparison of pressure signatures; near field case without lift coefficient constraint; extrapolated to ground level ($d_l = 941.7\ l_b$).

One of the advantages of the design optimization procedure is its applicability to conduct design trade-off studies. This is illustrated by the results shown above. The two design objectives of minimum sonic boom and improved aerodynamic performance often impose conflicting restrictions/variations on the geometric parameters of the aircraft. This is observed to be true while comparing the two cases described above. In the first case where a constraint on the lift coefficient is imposed, the optimum design has an improved lift coefficient. The sonic boom signature associated with this design is also reduced. However, an increase in the second peak is observed. In the second case where no constraint is imposed on the lift coefficient, the reduction in the first peak is very significant (compared to the optimum from the previous case) and the second peak is also reduced. However, the lift coefficient also has decreased. The optimum design shows significant improvements in C_D and C_D/C_L values compared to the optimum design from the first case illustrating the trade-off between low sonic boom and high lift configurations. Both sonic boom overpressures and induced drag increase with an increase in the lift and decrease with a decrease in the lift. The optimization procedure, in the second case, exploits this important physical relationship and yields significantly low boom configurations with reduced C_L.

Far Field Sonic Boom Minimization ($d_l = 941.7\ l_b$)

The results from the optimization of the pressure signature at a distance of 941.7 l_b are presented next. As before, optimization has been performed for minimum sonic boom first peak (Δp_1) and minimum C_D/C_L without any constraint on the lift coefficient. Table 9 compares the reference and the optimum values of the design variables and the performance functions used in the optimization. The significant changes to the design variables can be seen. The wing thickness-to-chord ratio, wing span and nose radius have reduced whereas the wing root chord and nose length have increased. Figure 22 compares the reference and optimum geometries. Figure 23 compares the reference and the optimum values of the normalized objective functions. The first peak in the pressure signature has decreased by 10.2 percent for the optimum configuration. The drag-to-lift ratio has decreased by 6.0 percent and the drag coefficient has decreased by 9.7 percent. The lift coefficient has also decreased (3.9 %). The drag force has decreased by 13.1 percent and the lift force has reduced by 7.2 percent. Figure 24 presents the pressure signatures for the reference and optimum configurations. The percentage reductions in the optimum far field pressure peaks are not as significant as those in the near field optima because the far field signature is less sensitive to changes in the design variables. This is due to the fact that the sonic boom extrapolation procedure coalesces all the detailed shock information into an N-wave in the far field. This also results in a higher reduction in the aircraft lift.

Table 9. Delta wing-body case; far field optimization without lift coefficient constraint.

Design variables and performance functions	Reference	Optimum
Root chord, c_o (m)	7.08	7.73
Leading edge sweep, λ (deg)	66.0	68.9
Thickness to chord ratio, t_c	0.05200	0.04680
Wing half span, w_s (m)	3.53	3.2055
Nose length, l_n (m)	6.01	6.611
Max. nose radius, r_m (m)	0.570	0.5415
First pressure peak (Δp_1)	0.0019479	0.0017499
Second pressure peak (Δp_2)	0.0033103	0.0031540
Drag-to-lift ratio, C_D/C_L	0.11681	0.10985
Drag coefficient, C_D	0.024460	0.022099
Lift coefficient, C_L	0.20940	0.20117
Drag force (N)	16539.6	14374.5
Lift force (N)	141594.1	131328.6

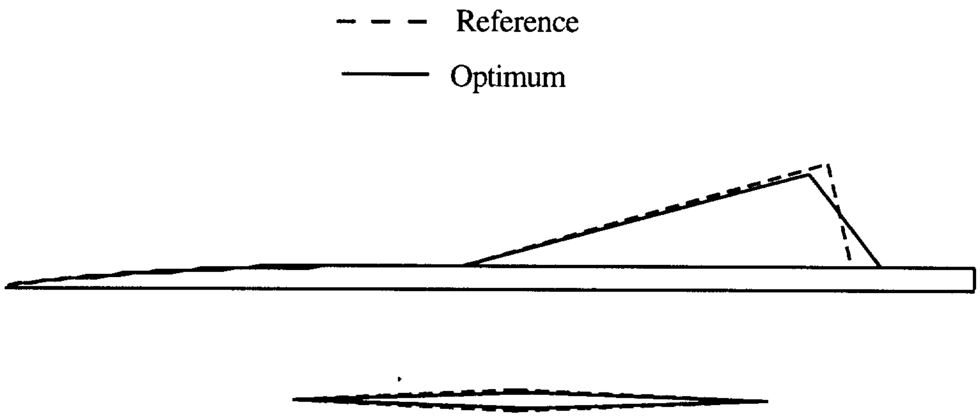

Figure 22. Comparison of geometries; far field case without lift coefficient constraint.

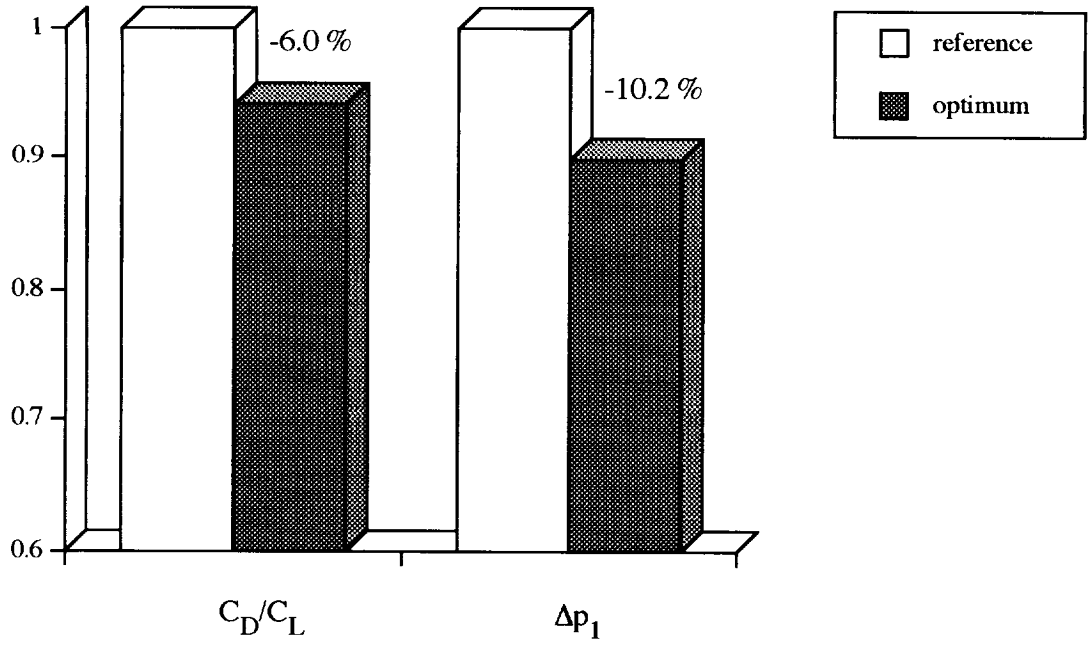

Figure 23. Comparison of objective functions; far field case without lift coefficient constraint.

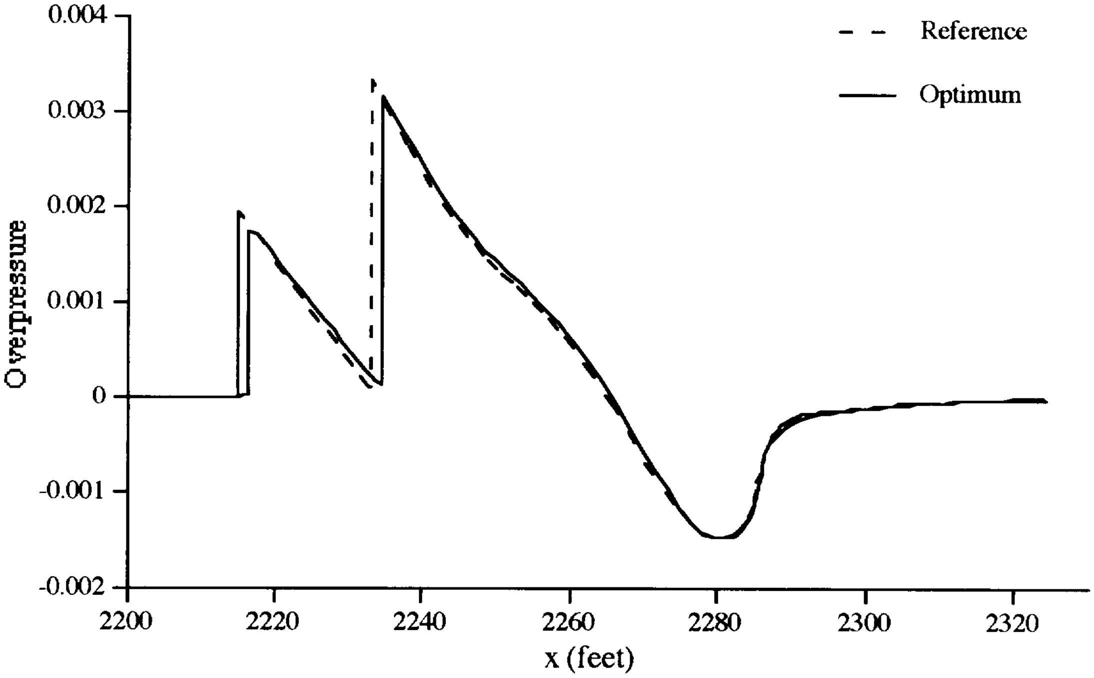

Figure 24. Comparison of pressure signatures; far field case without lift coefficient constraint.

5.3.6 Doubly Swept Wing-Body Optimization

For the doubly swept wing-body configuration case, the two leading edge sweeps (λ_1 and λ_2), the break length (x_b), the wing root chord (c_o), the wing tip chord (c_t), the maximum nose radius (r_m), the nose length (l_n) and the wing starting location (x_w) are used as design variables. The reference values of the doubly swept wing-body parameters are: root chord (c_0) = 8.12 m, tip chord (c_t) = 1.62 m, first leading edge sweep (λ_1) = 70.2 degrees, second leading edge sweep (λ_2) = 54.9 degrees, maximum radius (r_m) = 0.57 m, nose length (l_n) = 6.01 m, break length (x_b) = 12.28 m, wing starting location (x_w) = 8.13 m, wing span (w_s) = 3.53 m, wing thickness-to-chord ratio (t_c) = 0.05 and body length (l_b) = 17.52 m. The wing half span (w_s), the wing thickness to chord ratio (t_c) and the body length (l_b) are held constant during the optimization. The optimization of the doubly swept wing-body configuration has been carried out in two steps. In the first step, the body radius and nose length are used as design variables to minimize the first peak in the sonic boom pressure signature. In the second step, the wing geometric parameters are used as design variables to minimize the second peak in the sonic boom pressure signature, while the nose dimensions are maintained at their optimum values obtained from the first step. In both steps, optimization is performed for minimum C_D/C_L and minimum sonic boom (Δp_1 and Δp_2) at a near field distance of $d_l = 3.61\ l_b$. The lift coefficient is constrained using $C_{L_{min}} = 0.95\ C_{L_{ref}}$ and $C_{L_{max}} = 1.05\ C_{L_{ref}}$ where $C_{L_{ref}}$ is the lift coefficient of the reference configuration. Table 10 presents the reference and the optimum values of the design variables and the performance functions used in the optimization.

Figure 25 compares the reference and the optimum geometries. Figure 26 compares the reference and the optimum values of the normalized objective functions. The first peak in the sonic boom signature (Δp_1) has decreased by 23.6 percent in the optimum configuration. This is due to decrease in the maximum radius (r_m) and the increase in the nose length (l_n) during optimization. This slender nose has a smaller equivalent area distribution for the nose region yielding a reduced first pressure peak. Significant increases are observed in the first leading edge sweep, the root chord and the break length of the optimum wing. These increases coupled with the decreases in the wing tip chord and starting location result in a smaller planform area for the optimum wing. The smaller planform area has a smaller equivalent area and lift distribution yielding a significant reduction (19.9 %) in the second pressure peak of the sonic boom signature. Also, the increase in the first leading edge sweep of the wing corresponds to a weaker leading edge shock in the wing. This factor also contributes to the decrease in the second peak (Δp_2) of the sonic boom signature. The C_D/C_L ratio has also decreased by 3.6 percent in the optimum configuration. This percentage reduction is small because there are simultaneous reductions in both drag and lift in this case. The drag coefficient has decreased by 4.7 percent and the drag force has decreased by 9.2 percent. There is also a decrease in the lift coefficient (1.1 %) and the lift force (4.9 %) of the aircraft. The increase in the first leading edge sweep of the aircraft corresponds to a decreased value of the effective Mach number. Also, the optimum configuration has a smaller planform area. Therefore, the lift coefficient and the lift have decreased for the optimum configuration. Figures 27a and 27b present the sonic boom pressure signatures for the reference and the optimum configurations at near and far fields, respectively. The reductions in the two pressure peaks can be seen.

Table 10. Doubly swept wing-body case; near field optimization with lift constraint.

Design variables and performance functions	Reference	Optimum
Maximum nose radius, r_m (m)	0.57	0.513
Nose length, l_n (m)	6.01	6.61
First leading edge sweep, λ_1 (degrees)	70.16	74.25
Root chord, c_o (m)	8.12	8.60
Second leading edge sweep, λ_2 (degrees)	54.93	52.51
Tip chord, c_t (m)	1.62	1.39
Break length, x_b (m)	12.28	12.76
Wing starting location, x_w (m)	8.13	7.75
First pressure peak	0.03389	0.02590
Second pressure peak	0.05483	0.04394
Drag-to-lift ratio, C_D/C_L	0.11510	0.11099
Drag coefficient	0.02238	0.02133
Lift coefficient	0.19441	0.19221
Drag force (N)	18558.2	16852.5
Lift force (N)	159666.9	151843.3

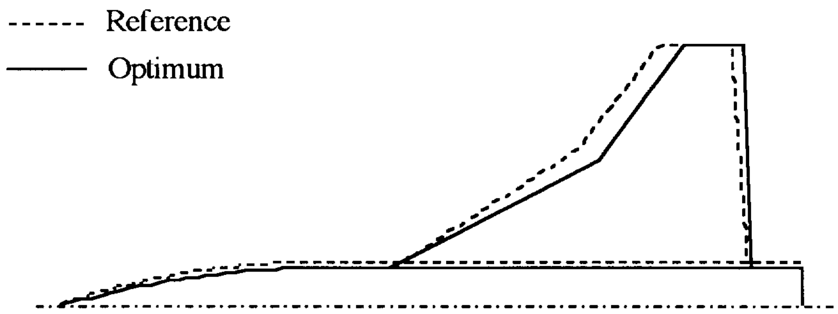

Figure 25. Comparison of planforms; near field case with lift coefficient constraint.

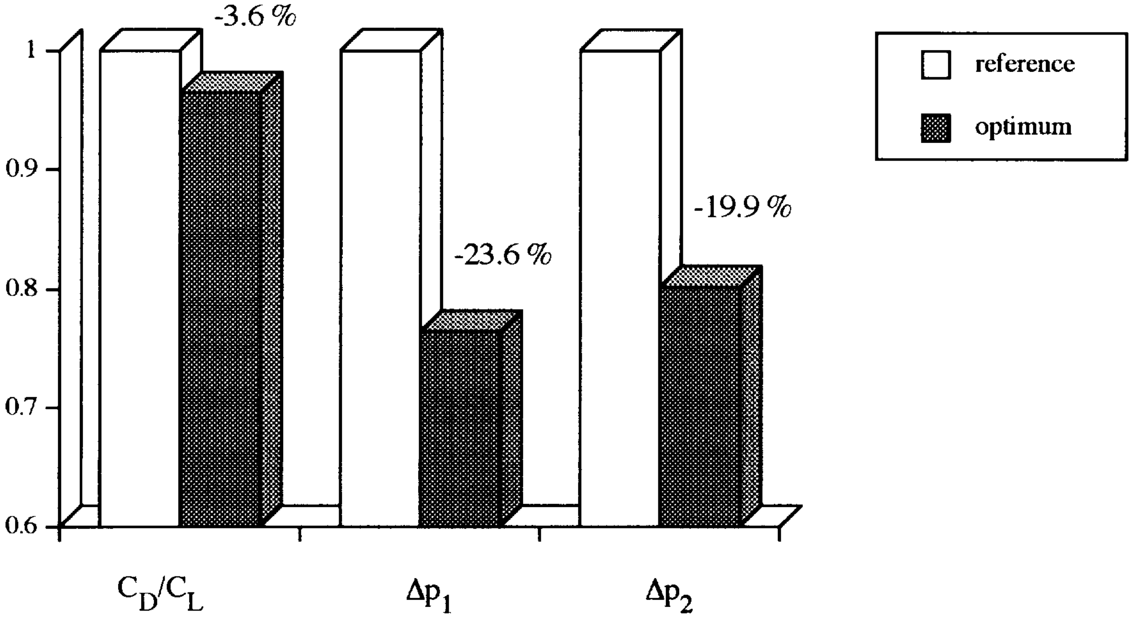

Figure 26. Comparison of objective functions; near field case with lift coefficient constraint.

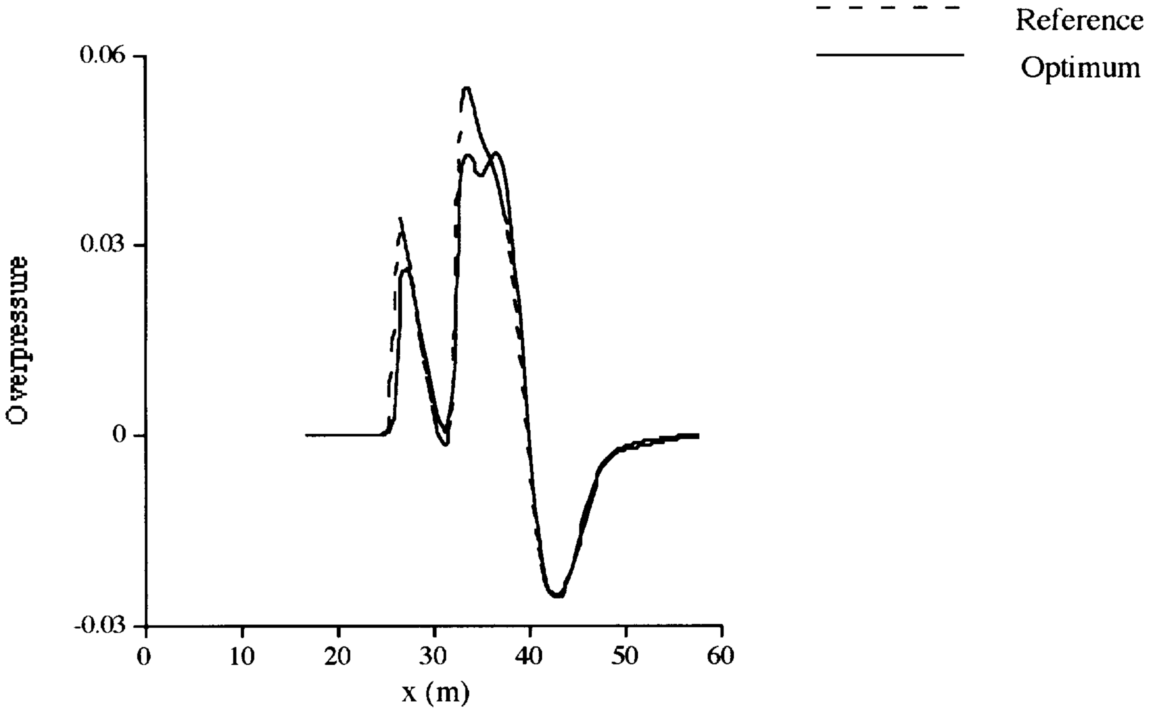

Figure 27a. Comparison of pressure signatures; near field optimization with lift coefficient constraint; $d_l = 3.61\ l_b$.

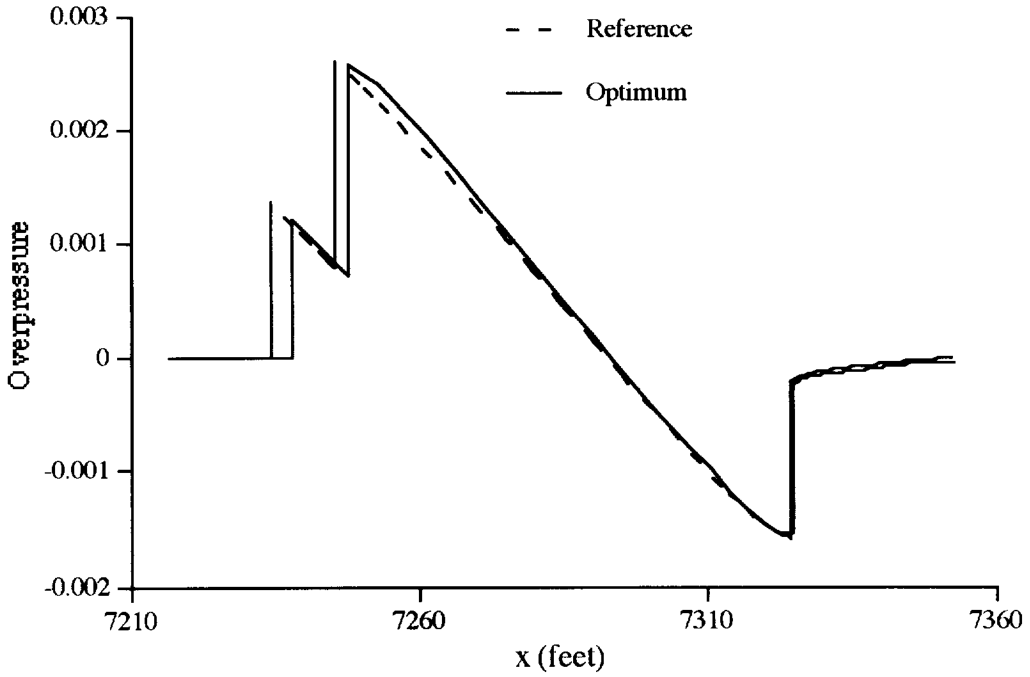

Figure 27b. Comparison of pressure signatures; near field case with lift coefficient constraint; extrapolated to ground level ($d_l = 941.7\ l_b$).

The optimum designs from the aerodynamic/sonic boom optimization procedure for the two configurations show a common trend. All these optimum designs are such that the nose region of these configurations are more slender than their reference nose configurations. Correspondingly, the first peaks in the pressure signatures of these optimum designs have decreased. This is contrary to the trends observed by previous optimization studies [80-87] that the nose region actually becomes more blunt for the sonic boom to decrease. The reasoning given in these studies behind this trend is that, a blunt nosed configuration with special shaping gives rise to a strong shock wave which avoids coalition with shocks from other aircraft components, thereby resulting in a weak wave in the far field. However, the current MDO procedure that couples sonic boom and aerodynamic criteria, does not compromise aerodynamic performance for sonic boom improvement and yields slender bodies which have improved sonic boom as well as aerodynamic characteristics.

5.4 Integrated Aerodynamic/Sonic Boom/Structural Optimization

The fourth MDO procedure developed in this research addresses the simultaneous improvement in the aerodynamic, sonic boom and structural performance of high speed aircraft configurations. The procedure uses two-levels of decomposition that are coupled with each other. Since the sonic boom characteristics of an aircraft are strongly tied in with its aerodynamics, the performance of the aircraft in these two disciplines is addressed in level 1 of the optimization procedure. At level 2, the structural performance of the aircraft is optimized. The MDO problem is formulated as follows.

5.4.1 Optimization Formulation

Level 1

The objectives at this level are reduced sonic boom pressure peaks and improved aerodynamic performance. This can be stated as follows.

Minimize

Δp_1, Δp_2 and C_D/C_L

subject to the constraints

$$C_{L\min} \leq C_L \leq C_{L\max}$$

$$W \leq W_{\max}$$

$$\Phi^1_{min} \leq \Phi^1 \leq \Phi^1_{max}$$

$$\Phi^2_{min} \leq \Phi^2 \leq \Phi^2_{max}$$

where Δp_1 and Δp_2 are the overpressure peaks in the sonic boom signature at a distance d_1 from the aircraft. The quantity W is the aircraft weight. Φ^1 is the first level design variable vector, Φ^2 is the second level design variable vector and the subscripts "min" and "max" denote lower and upper bounds respectively. To incorporate the structural coupling in the first level, constraints are imposed on the second level objective function, namely the aircraft weight (W) and the second level design variables (Φ^2). The derivatives, $\frac{\partial W^*}{\partial \phi_{i1}}$ and $\frac{\partial \phi^*_{j2}}{\partial \phi_{i1}}$, are the optimal sensitivity parameters of the second level objective function and design variables with respect to the first level design variables. These derivatives establish the coupling between the two-levels of optimization.

Level 2

In the second level, structural optimization of the wing-body configuration is performed during which, the first level design variables (Φ^1) are held fixed at their optimum values obtained from level 1 optimization. The optimization problem is defined as follows.

Minimize

$$W$$

subject to the following constraints

$$g(\bar{\sigma}) \leq 0$$

$$M_x{}^r \leq M_x{}^r{}_{max}$$

$$M_y{}^r \leq M_y{}^r{}_{max}$$

$$\Phi^2_{min} \leq \Phi^2 \leq \Phi^2_{max}$$

where $\bar{\sigma}$ is the stress vector, $g(\bar{\sigma})$ is a stress-based failure criterion to determine material failure, $M_x{}^r$ and $M_y{}^r$ are the root bending moments along the x and the y directions [Fig. 28], respectively and subscripts 'min' and 'max' denote lower and upper bounds, respectively. The upper bounds on the root bending moments are imposed to reduce the loading that is eventually transmitted to the aircraft. The wing structural parameters are used as design variables during the optimization. The multilevel optimization procedure iterates through the two-levels until global convergence is achieved.

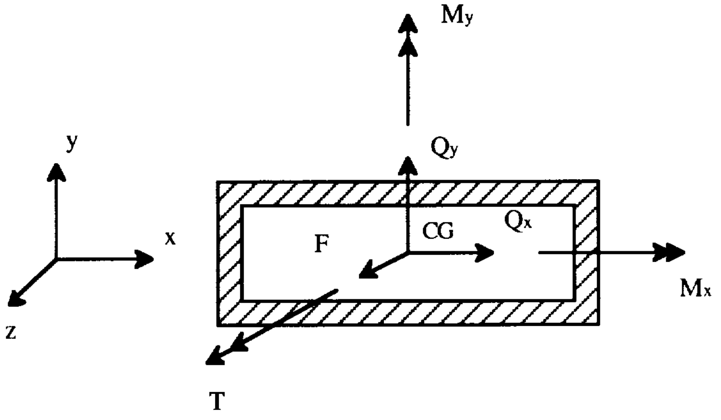

Figure 28. Nodal force vectors due to aerodynamic loading at a given wing section.

5.4.2 Wing-Body Configuration

The two-level optimization is applied to the design optimization of the doubly swept wing-body configuration (Fig. 15), described in Section 5.4.4. The reference values of the doube sweep wing-body parameters are:c_o = 8.12 m, c_t = 1.62 m, λ_1 = 70.2 degrees, λ_2 = 54.9 degrees, r_m = 0.57 m, l_n = 6.01 m, x_b = 12.28 m, x_w = 8.13 m, w_s = 3.53 m, t_c = 0.05 and l_b = 17.52 m. The wing half span (w_s), the wing thickness to chord ratio (t_c) and the body length (l_b) are held constant during the optimization. The two leading edge sweeps (λ_1 and λ_2), the break length (x_b), the wing root chord (c_o), the wing tip chord (c_t), the maximum nose radius (r_m), the nose length (l_n) and the wing starting location (x_w) are used as design variables during optimization at level 1.

5.4.3 Structural Model and Analysis

The principal load carrying member in the wing is modeled as a single-celled composite box beam, as illustrated in Fig. 29. The structural design variable vector (Φ^2) includes the box beam width to chord ratio (w_c) and the ply angles (θ's) of the laminates used to form the box beam walls (Fig. 29). The box beam width to chord ratio (w_c) is a continuous design variable whereas the ply angles are discrete variables, taking on discrete values from the set (0°, ±15°, ±30°, ±45°, ±60°, ±75° and ±90°).

The analysis procedure for such composite beams is based on the formulation developed by Smith and Chopra [125]. The analysis procedure allows the inclusion of pre-twist, taper and spanwise sweep in the box beam. Using the analytical model, the deformation of the beam is described through extension, bending, torsion, transverse shearing and torsion related warping. In the present work, this quasi one dimensional model is used within a finite element analysis to obtain nodal deflections and stresses in the load carrying member. The beam has been divided into 10 elements over the wing span. The i^{th} finite element is bounded by the nodes i ($z = z^i$) and i+1 ($z = z^{i+1}$). Each finite element has 19 degrees of freedom, $\mathbf{U}_e$, which are described as follows [Fig. 30].

$$\mathbf{U}_e^T = [\, u_1, u_2, u_3, u_4, v_{b_1}, v_{b_1}', v_{b_2}, v_{b_2}', w_{b_1}, w_{b_1}', w_{b_2}, w_{b_2}', \phi_1, \phi_2, \phi_3, v_{s_1}, v_{s_2}, w_{s_1}, w_{s_2} \,] \tag{54}$$

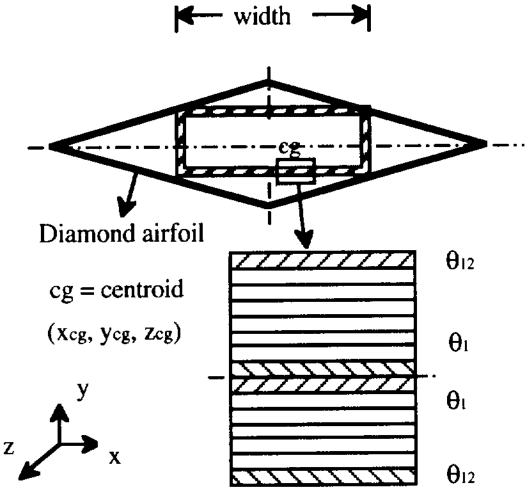

Figure 29. Composite box beam model.

In Eq. 54, u is the spanwise wing displacement, v and w are the inplane vertical and horizontal wing displacements and ϕ is the elastic twist. First partial derivatives with respect to the spanwise coordinate (z) are denoted ('). The inplane wing displacements are expressed as a sum of two terms, one corresponding to pure bending and another corresponding to shear. In Eq. 54, the subscript (b) refers to the displacements due to beam bending and the subscript (s) refers to the displacements due to shear.

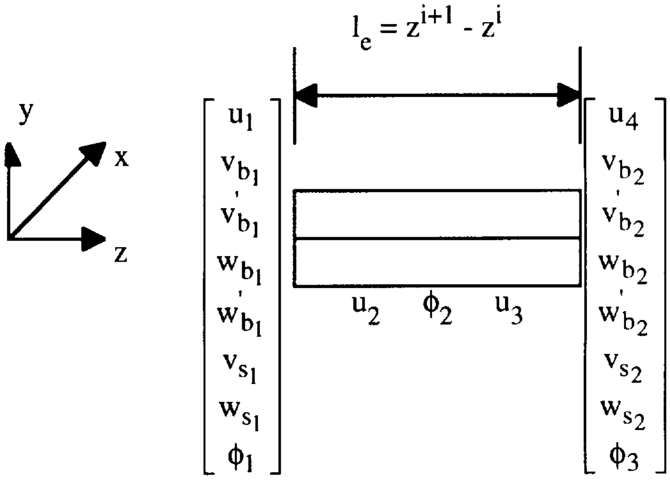

Figure 30. Finite element degrees of freedom.

The elemental equations of equilibrium can then be expressed as follows.

$$\begin{Bmatrix} F \\ Q_y \\ Q_x \end{Bmatrix} = \begin{bmatrix} k_{11} & 0 & k_{13} \\ 0 & k_{22} & k_{23} \\ k_{13} & k_{23} & k_{33} \end{bmatrix} \begin{Bmatrix} u' \\ \gamma^o_{z\eta} \\ \gamma^o_{z\varsigma} \end{Bmatrix} \tag{55}$$

$$\begin{Bmatrix} T \\ M_y \\ M_x \end{Bmatrix} = \begin{bmatrix} k_{44} & 0 & k_{46} \\ 0 & k_{55} & k_{56} \\ k_{46} & k_{56} & k_{66} \end{bmatrix} \begin{Bmatrix} \phi' \\ w'' - \gamma^{o'}_{z\varsigma} \\ v'' - \gamma^{o'}_{z\eta} \end{Bmatrix} \tag{56}$$

where F is the spanwise force, Q_y and Q_x denote the inplane forces in the vertical and the horizontal directions, T is the torsional moment and M_y and M_x denote the bending moments in the vertical and the horizontal directions [Fig. 28] , respectively. k_{ij} represents the element stiffness matrix and $\gamma^o_{z\eta}$ and $\gamma^o_{z\varsigma}$ are the inplane shear stresses in the vertical and the horizontal directions of the composite box beam walls, respectively. Further details of the formulation can be found in Ref. 125. The elemental equations are assembled into a global system of equations for the unknown nodal wing displacements.

$$\mathbf{F_G} = \mathbf{K_G U_G} \tag{57}$$

where $\mathbf{F_G}$ is the global force vector, $\mathbf{K_G}$ is the global stiffness matrix and $\mathbf{U_G}$ is the vector of nodal wing displacements.

5.4.4 Aerodynamic Load Calculations

The finite element method for the aircraft wing structural analysis requires the nodal load vectors to be specified. Clearly, the loading on the wing structure comes from the aerodynamic forces and moments that act on the surface of the wing. The pressure distribution on the wing, which gives rise to these forces and moments, is obtained from the UPS3D flow solver. These forces and moments are expressed as follows.

$$Q_x^i = \iint_{S_i^{i+1}} -p(x,y,z)ds_x \tag{58}$$

$$Q_y^i = \iint_{S_i^{i+1}} -p(x,y,z)ds_y \tag{59}$$

$$F^i = \iint_{S_i^{i+1}} -p(x,y,z)ds_z \tag{60}$$

$$M_x^i = \iint_{S_i^{i+1}} -p(x,y,z)(z-z_{cg}^i)ds_y \tag{61}$$

$$M_y^i = \iint_{S_i^{i+1}} -p(x,y,z)(z-z_{cg}^i)ds_x \tag{62}$$

$$T^i = \iint_{S_i^{i+1}} -p(x,y,z)\left[(x-x_{cg}^i)ds_y+(y-y_{cg}^i)ds_x\right] \tag{63}$$

In Eqs. 58-63, p(x,y,z) is the local pressure, ds_x, ds_y and ds_z are the projections of an elemental wing surface area element (dS) in the x, y and z directions, respectively and S_i^{i+1} denotes the area segment between the finite element nodes i ($z = z^i$) and i+1 ($z = z^{i+1}$). The quantities x_{cg}^i, y_{cg}^i and z_{cg}^i are the x, y and z coordinates of the centroid of the beam section at node i ($z = z^i$) (Fig. 29). Since a symmetric composite box beam is used at every station throughout the span, the centroid corresponds to the center of the box beam section (Fig. 29).

The Tsai-Wu failure criterion [126] has been used in the second level optimization to avoid composite material failure. This criterion is expressed as follows.

$$\left(\frac{1}{\sigma_{1_T}}-\frac{1}{\sigma_{1_C}}\right)\sigma_1+\left(\frac{1}{\sigma_{2_T}}-\frac{1}{\sigma_{2_C}}\right)\sigma_2+\frac{\sigma_1^2}{\sigma_{1_T}\sigma_{1_C}}$$
$$+\frac{\sigma_2^2}{\sigma_{2_T}\sigma_{2_C}}-\frac{\sigma_1\sigma_2}{\sqrt{\sigma_{1_T}\sigma_{1_C}\sigma_{2_T}\sigma_{2_C}}}+\frac{\tau_{12}^2}{\tau_{12_S}^2}<0 \qquad (64)$$

where σ_1 and σ_2 represent normal stresses along the material axes and τ_{12} represents the shear stress. The subscripts T, C and S represent ultimate stress in tension, compression and shear, respectively. The Tsai-Wu criterion reduces the total number of constraints as individual constraints on the stresses (σ_1, σ_2 and τ_{12}) at each ply are eliminated. Each of the four composite plates used in the box beam modeling is assumed to be symmetric about the midplane of the plate and the beam itself is assumed to be symmetric about the beam centerline. The above failure criterion is imposed, on each lamina, at each of the four corners of the box beam to prevent failure due to stresses.

5.4.5 Weight Calculations

The aircraft weight (W) is calculated as the sum of the fuselage skin weight (W_{fus}), the wing skin weight (W_{wsk}) and the wing spar weight (W_{wsp}). The skin is assumed to be made of 2014-T6 Aluminum alloy. The composite box beam is assumed to be made of Carbon-Epoxy IM6/Epoxy. This material has a density of 1600 Kg/m^3 and its ultimate stresses are given by σ_{1_T} = 3500 MPa, σ_{1_C} = 1540 MPa, σ_{2_T} = 56 MPa, σ_{2_C} = 150 MPa, τ_{12_S} = 98 MPa. The box beam vertical wall thickness (t_v) is 0.0366 m and the horizontal wall thickness (t_w) is 0.0366 m. These two parameters are held fixed during the optimization. The expressions for W_{fus}, W_{wsk}, W_{wsp} are as follows.

$$W = W_{fus} + W_{wsk} + W_{wsp} \qquad (65)$$

$$W_{fus} = \left(r_m(l_b - l_n) + \int_0^{l_n} r(x)dx \right) \pi t_{sk} \rho_{sk} g \qquad (66)$$

$$W_{wsk} = \left(\sqrt{1+t_c^2} \int_{r_m}^{w_s} c(z)dz \right) t_{sk} \rho_{sk} g \qquad (67)$$

$$W_{wsp} = \rho_{sp} g * [\, -4 t_h t_v (w_s - r_m) + 2\left[w_c t_h + t_c(1 - w_c) t_v\right] \int_{r_m}^{w_s} c(z)dz \,] \qquad (68)$$

where t_{sk} is the skin thickness, ρ_{sk} is the density of the skin material, ρ_{sp} is the density of the wing spar material, c(z) is the local chord at any spanwise wing section z and g is the acceleration due to gravity.

5.4.6 Optimization Algorithms

In level 1, all the design variables are continuous and a nonlinear quasi Newton technique which uses the BFGS algorithm [108] for finding the search direction is used. The structural optimization problem at the second level involves a design variable vector that includes both continuos design variables Φ_c (e.g., spar width-to-chord ratio) and discrete design variables Φ_d (e.g., ply angles). Continuos design variables are not compatible with combinatorial optimization methods such as branch and bound techniques which require discrete values to operate. Similarly, discrete variables are not compatible with gradient-based optimization methods unless a continuous relaxation of the discrete variables is allowed which may lead to sub-optimal solutions. Thus, optimization problems with both continuous and discrete design variables require the development of a technique which efficiently incorporates both types of design variables. Chattopadhyay and Seeley [127] have recently developed a hybrid optimization technique which can efficiently include both continuous and discrete design variables. This procedure uses both a gradient-based search and a modified simulated annealing algorithm to obtain a more global optimum. The technique is briefly outlined below.

```
1.  START
2.  Current value of objective function is F
3.  Select either continuous or discrete design variables to perturb for $F_{new}$
4.  If continuous variables are selected,
        $\Phi_{c_{new}} = \Phi_c + \alpha S_c$
5.  If discrete variable is selected
        $\Phi_{d_{new}} = \Phi_{d_i}$
6.  Compute $F_{new}$
7.  If $F_{new} \leq F$ then
        $F = F_{new}$
    Else if $P_{acc} \geq P$ then
        $F = F_{new}$
    Endif
8.  Check for convergence
9.  If no convergence, go to START else STOP
```

Here, the quantity F is the current value of the K-S function. α is a random step size selected to be within a prescribed percentage of the current value of the continuous variables and S is the search direction vector which is determined from the gradients of the K-S function with respect to the continuous design variables. The subscript i refers to the i^{th} choice for a discrete design variable out of a set of discrete values and the subscript 'new' stands for a new design point. The continuous design variables are perturbed using α and S to improve the efficiency of the search while the discrete variables are perturbed by randomly selecting values for Φ_{d_i} within a given set. Move limits and bounds are imposed on the continuous design variables to ensure a physically meaningful design. The parameter P is a random number such that $0 \leq P \leq 1$ and the acceptance probability (P_{acc}) of retaining a worse design is computed as follows.

$$P_{acc} = \exp(-\Delta F/T) \tag{69}$$

where ΔF represents the change in objective function and T is the "temperature" which is computed at each iteration using the following relation.

$$T = T_o q^i \tag{70}$$

where the temperature T is reduced from the initial temperature T_o during successive iterations i using the cooling rate q ($0 < q < 1$). A high temperature allows the optimizer to occasionally accept a design for which the objective function (F_{new}) value is worse than the reference value. The worse design is accepted based on the acceptance probability probability and allows the algorithm to climb out of local minima. The acceptance probability is gradually reduced to zero during optimization so that the optimizer converges smoothly to an improved design point.

The hybrid optimization procedure relies on a directed search for the continuous design variables which increases efficiency. However, the probabilistic nature of the simulated annealing algorithm allows the optimization procedure to climb out of local minima. Therefore, the procedure exhibits the benefits of both gradient-based and discrete optimization techniques.

5.4.7 Results and Discussion

The optimization at level 1 has been carried out in two steps. In the first step, the body radius and nose length are used as design variables to minimize the first peak in the sonic boom pressure signature. In the second step, the wing geometric parameters are used as design variables to minimize the second peak in the sonic boom pressure signature, while the nose dimensions are maintained at their optimum values obtained from the first step. In both steps, optimization is performed for minimum C_D/C_L and minimum sonic boom (Δp_1 and Δp_2). The lift coefficient is constrained using $C_{L_{min}} = 0.95\ C_{L_{ref}}$ and $C_{L_{max}} = 1.05\ C_{L_{ref}}$ where $C_{L_{ref}}$ is the lift coefficient of the reference configuration. The inviscid flow field around the vehicle is evaluated using the CFD solver (UPS3D) over a streamwise distance that extends from the tip of the body up to three times the body length in the longitudinal direction. The aerodynamic sensitivity analysis at level 1 is performed using the semi-analytical sensitivity analysis techniques [94-95]. The sensitivity analysis at level 2 is performed using the finite difference method. A three-dimensional hyperbolic grid with 75 grid points in the circumferential direction and 80 grid points in the normal direction has been used. The cruise Mach number is 2.5, the angle of attack is 5 degrees and the flight altitude is approximately 16,500 m. The aircraft weight (W) is constrained during the level 1 optimization to be below $W_{max} = W_{ref}$ where W_{ref} is the weight of the reference configuration. The pressures at $d_o = 0.5\ l_b$ are directly obtained from the CFD solver. The sonic boom signatures at two locations have been considered during the optimization. The first of the two corresponds to a distance $d_l = 3.61\ l_b$ from the axis of the body and is denoted "near field" in the text. The second distance considered is $d_l = 941.7\ l_b$ from the axis of the body and is denoted "far field." This far field distance corresponds to the ground level. Results from both cases of optimization are discussed here.

Near Field Optimization ($d_l = 3.61\ l_b$)

Figure 31 compares the reference and the optimum geometries. Figure 32 compares the reference and the optimum values of the level 1 objective functions normalized with respect to their corresponding reference values.

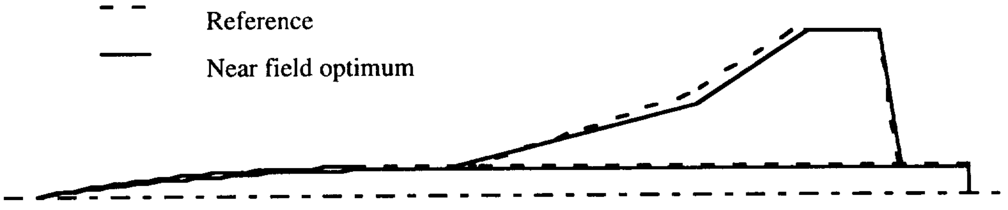

Figure 31. Comparison of planforms; near field optimization.

The first peak in the sonic boom signature (Δp_1) decreases by 23.6 percent in the optimum configuration. This is due to the decrease in the maximum radius (r_m) and the increase in the nose length (l_n) during optimization. This slender nose has a smaller equivalent area distribution for the nose region yielding a reduced first pressure peak. The smaller planform area of the optimum configuration has a smaller equivalent area and lift distribution. The increase in leading edge sweep (λ_l) of the optimum configuration also results in a weaker wing shock. These factors yield a significant reduction (18.7 %) in the second pressure peak (Δp_2) of the sonic boom signature.

The C_D/C_L ratio has also decreased by a modest 3.5 percent in the optimum configuration. This percentage reduction is small because there are simultaneous reductions in both drag and lift in this case. Figure 33 presents the sonic boom pressure signatures for the reference and the optimum configurations. The constraint imposed on the aircraft weight (W) during the level 1 optimization is satisfied throughout the optimization.

Table 11 presents the reference and the optimum values of the design variables and the performance functions used in the level 1 optimization. Significant increases are observed in the first leading edge sweep, the root chord and the break length of the optimum wing. These increases coupled with the decreases in the wing tip chord and starting location result in a smaller planform area for the optimum wing.

Table 11. Comparison of level 1 design variables and objective functions.

Design Variables	Reference	Near field optimum	Far field optimum
Maximum nose radius, r_m (m)	0.570	0.513	0.513
Nose length, l_n (m)	6.010	6.610	6.610
1st leading edge sweep, λ_1 (deg)	70.20	74.40	70.32
Root chord, c_o (m)	8.120	8.610	8.060
2nd leading edge sweep, λ_2 (deg)	54.93	52.45	59.75
Tip chord, c_t (m)	1.620	1.355	1.240
Break length, x_b (m)	12.28	12.44	11.27
Wing starting location, x_w (m)	8.130	7.670	7.150
First pressure peak (Δp_1)	0.03389 (Near) 0.00136 (Far)	0.02590 (-23.6 %)	0.00120 (-11.9 %)
Second pressure peak (Δp_2)	0.05483 (Near) 0.00269 (Far)	0.04459 (-18.7 %)	0.00258 (-3.9 %)
Drag-to-lift ratio, C_D/C_L	0.11510	0.11112 (-3.5 %)	0.10983 (-4.6 %)

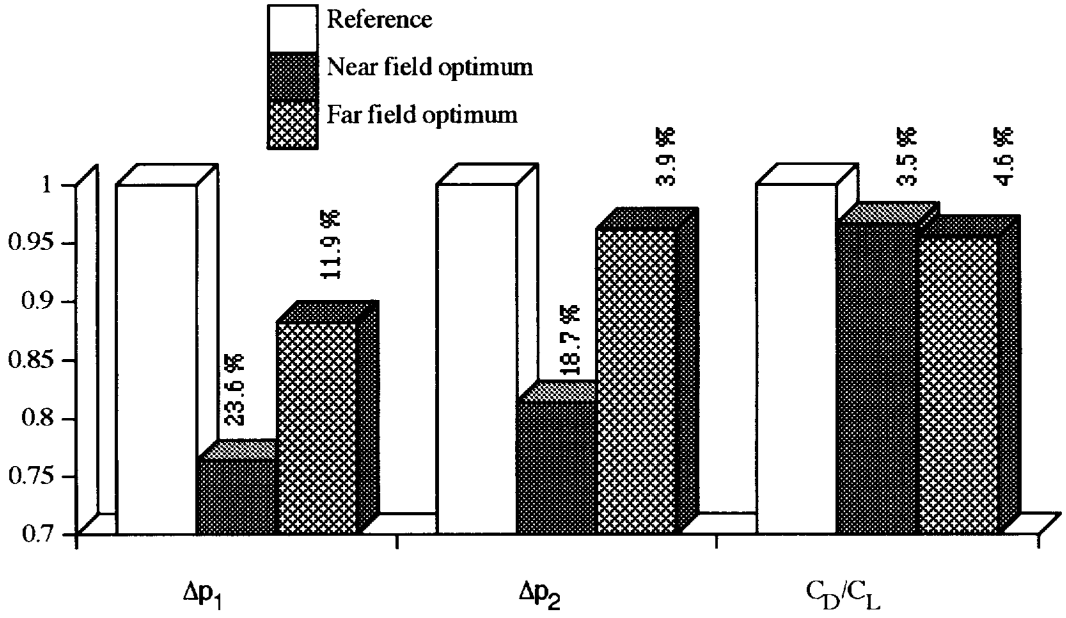

Figure 32. Comparison of level 1 objective functions.

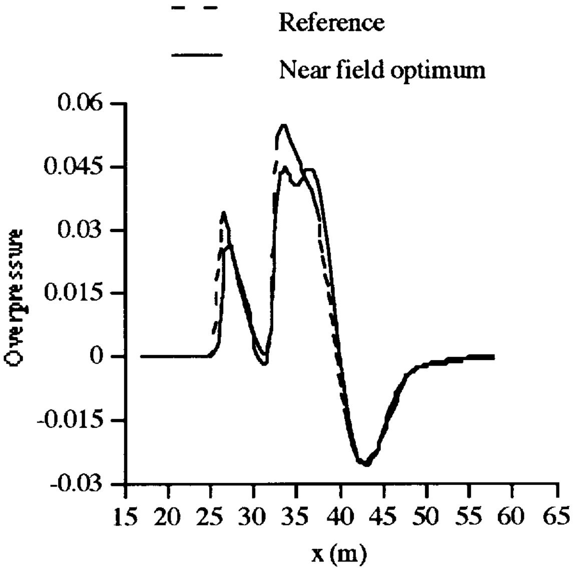

Figure 33. Comparison of pressure signatures; near field optimization.

Structural optimization is performed in level 2. As mentioned earlier, the walls of the composite box beam have 24 plies which are symmetrically oriented about the midsection of the wall. The corresponding 12 ply orientations and the beam width-to-chord ratio (w_c) have been used as design variables. Constraints on the stresses in the plies at all the spanwise finite element nodes are imposed through the Tsai-Wu criterion. The reference values are used as the upper bounds for the wing root bending moment constraints, that is, ${M_x}^r{}_{max} = {M_x}^r{}_{ref}$ and ${M_y}^r{}_{max} = {M_y}^r{}_{ref}$. The level 2 optimization is initiated with all the 12 ply angles set to the reference value of 90 degrees. Table 12 compares the reference and the optimum values of the design variables and the aircraft weight obtained from the level 2 optimization. Considerable reduction (10 percent) in the aircraft weight is observed from the reference to the optimum configuration.

Figure 34 compares the reference and the optimum values of the aircraft weight normalized with respect to the reference weight and shows the corresponding reductions in the fuselage, wing skin and wing spar weights. The aircraft weight reduction is due in part to the reductions in the fuselage weight (11.2 percent) and the wing skin weight (2.1 percent), associated with the changes in the level 1 design variables during the level 1 optimization. The reduction in the wing skin weight is relatively small because the reduction in the wing planform area is relatively small. Weight reduction is also obtained through a reduction in the wing spar weight (18.2 percent). The optimum spar width-to-chord ratio (w_c) has reduced by 16.1 percent to effect this change. In the reference configuration, the stress constraints are violated within several plies at various spanwise locations. The optimization procedure is able to modify these stresses through significant changes to the ply stacking sequence. The modified stress distribution in the optimum box beam configuration satisfies the Tsai-Wu criteria at all the plies at all spanwise finite element nodes. The optimum configuration also satisfies the root bending moment constraints well. Figure 35 compares the stresses and the root bending moments in the plies of the reference and the optimum beam configurations for the root section. It is to be noted the stresses and the bending moments have been normalized using their corresponding reference values. Significant reductions are observed in both the root stresses and the root bending moments after the optimization.

Table 12. Comparison of level 2 design variables and objective function(s).

Reference weight	1999.6 N
Near field optimum	1799.8 N (-10 %)
Far field optimum	1737.5 N (-13 %)

Design variable.	w_c	θ_1	θ_2	θ_3	θ_4	θ_5	θ_6	θ_7	θ_8	θ_9	θ_{10}	θ_{11}	θ_{12}
Reference	0.50	90°	90°	90°	90°	90°	90°	90°	90°	90°	90°	90°	90°
Near field	0.42	75°	75°	-75°	90°	75°	90°	-60°	90°	90°	-75°	-75°	75°
Far field	0.43	75°	75°	-75°	90°	90°	90°	-75°	90°	90°	90°	-75°	75°

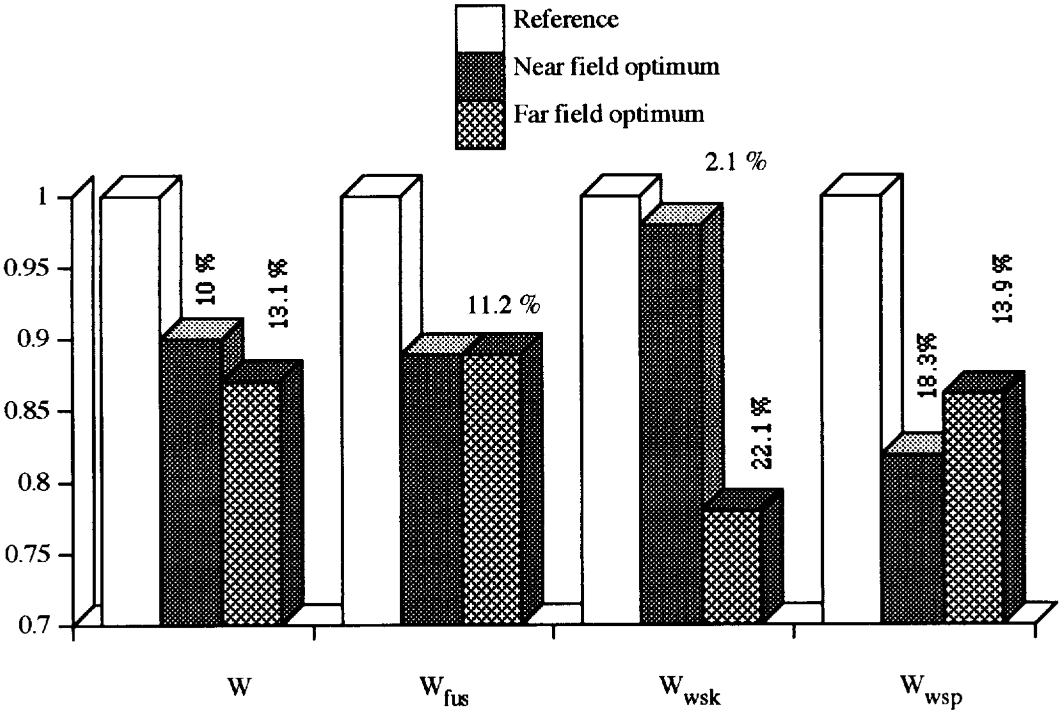

Figure 34. Comparison of level 2 objective function(s).

Far Field Optimization ($d_l = 941.7\ l_b$)

The far field optimization formulation is identical to that the near field optimization except that the sonic boom pressure peaks (Δp_1 and Δp_2) are evaluated at $d_l = 941.7\ l_b$. Table 11 presents the reference and the optimum values of the design variables and the performance functions used in the level 1 optimization. Figure 36 compares the reference and the optimum geometries. Figure 32 compares the reference and the optimum values of the level 1 objective functions normalized with respect to their corresponding reference values. The first peak in the sonic boom signature (Δp_1) has decreased by 11.9 percent in the optimum configuration. Similar to the near field optimization case, this is due to the decrease in the maximum radius (r_m) and the increase in the nose length (l_n) during optimization. In fact, it can be noticed that both the near field and the far field optimizations yield the same optimum values for these two design variables. However, the changes in the wing planform variables show different trends in the far field optimization. Unlike the near field case, there is relatively small changes in the first leading edge sweep (λ_1) and the wing root chord (c_o). The tip chord (c_t) has decreased significantly (23.4 percent) and the second leading edge sweep (λ_2) has increased (8.1 percent). The wing starting location (x_w) has moved forward by a significant 12.1 percent and the break length (x_b) has decreased by 8.2 percent. These factors yield only a modest reduction (3.9 %) in the second pressure peak (Δp_2) of the sonic boom signature. These design trends indicate that the far field sonic boom signature is relatively less sensitive to design variable changes than the near field signature. This is due to the fact that the sonic boom extrapolation procedure [124] tries to fit an approximate N-wave to the sonic boom signature at far field distances. The extrapolation procedure coalesces all the detailed shock information into the N-wave in the far field and makes it less sensitive to changes in the design variables. The C_D/C_L ratio has decreased by 4.6 percent in the optimum configuration.

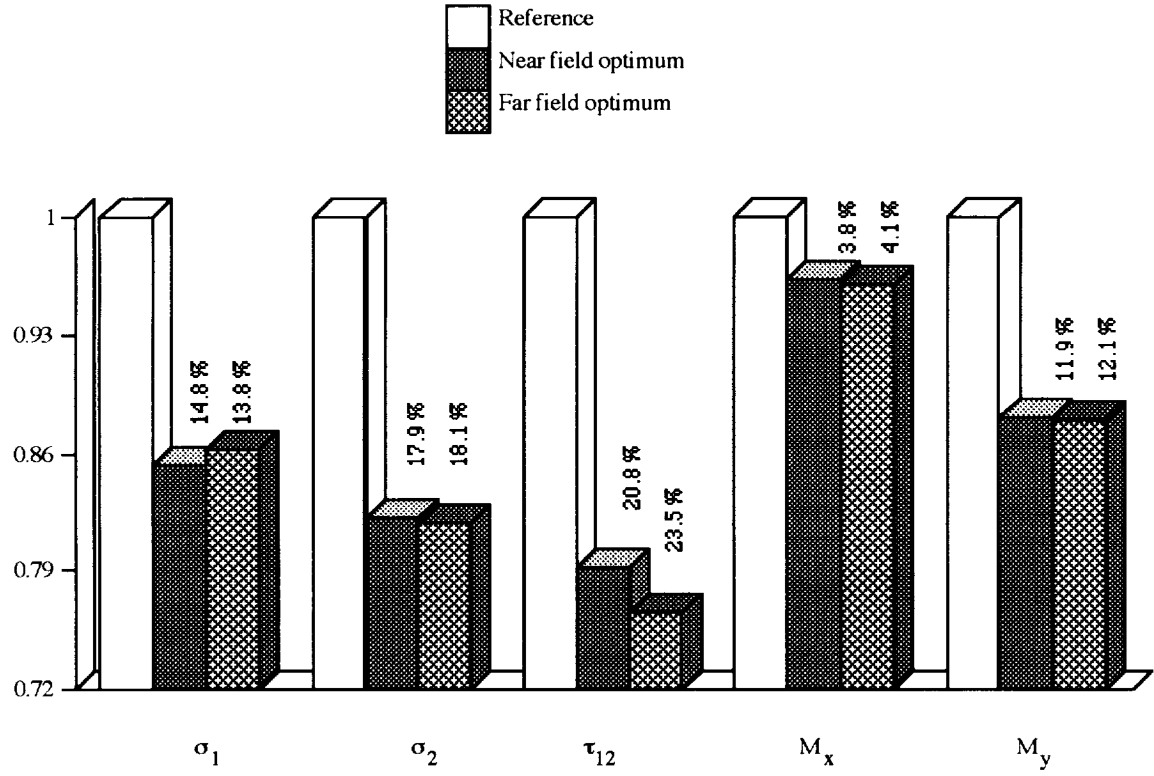

Figure 35. Comparison of normalized root stresses and bending moments.

Figure 37 presents the sonic boom pressure signatures for the reference and the optimum configurations. Since the wing starting location and the break length have decreased for the optimum configuration [Fig. 36], the relative separation between the first and the second sonic boom overpressure peaks has also decreased for the optimum configuration. This can be clearly seen in Fig.37 for the optimum pressure signature.

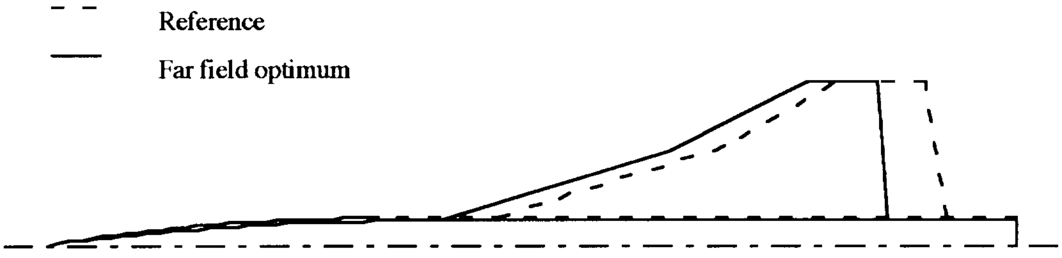

Figure 36. Comparison of planforms; far field optimization.

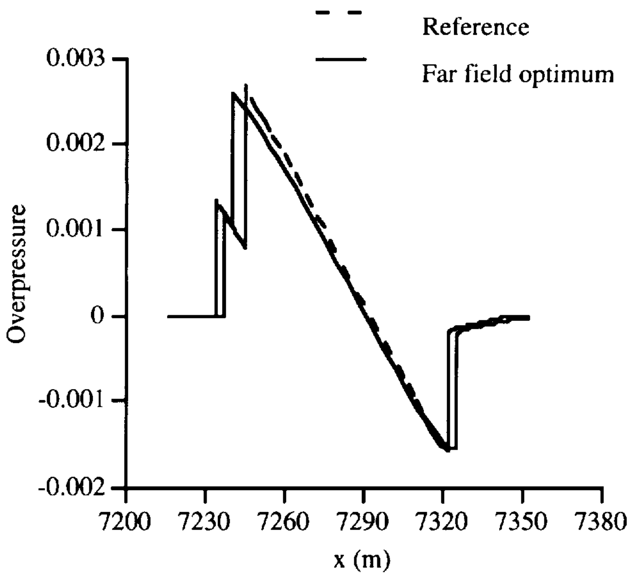

Figure 37. Comparison of pressure signatures; far field optimization.

The reference design for the level 2 (structural) optimization has the 12 ply angles set equal to 90 degrees. Table 12 compares the reference and the optimum values of the design variables and the aircraft weight obtained from the level 2 optimization. The optimization procedure reduces the weight significantly (13 percent). Figure 34 compares the reference and the optimum values of the aircraft weight normalized with respect to the reference weight and shows the significant reduction in the total weight and its components. The fuselage weight, the wing skin weight and the wing spar weight have decreased by 11.2 percent, 22.1 percent and 13.9 percent, respectively. Unlike the near field case, the wing skin weight has reduced significantly in this case because the planform area of the far field optimum configuration is considerably smaller than the planform area of the reference configuration. The stress distribution in the optimum configuration satisfies the Tsai-Wu criteria at all the plies and at all spanwise finite element nodes. The optimum configuration also satisfies the root bending moment constraints. Figure 35 compares the stresses and the root bending moments in the plies of the reference and the optimum beam configurations for the root section. The optimization procedure successfully reduces the stresses and the root bending moments in all the plies. However, the reduction in the root bending moments are mainly due to the reductions in the aerodynamic loading corresponding to the decreases in the drag and the lift forces of the wing-body. The values of the root bending moments are dictated by the aerodynamic loading. If an "all-at-once" approach is used to perform the multidisciplinary optimization instead of the present multilevel decomposition technique, these root bending moment constraints would play an important role during optimization.

From Table 12, it can be observed that in level 2, the near field optimum and the far field optimum lead to similar design variable changes. One of the main reasons for this trend is that the aerodynamic load distributions, obtained after level 1 optimization, are similar to each other in both the near field and the far field cases. Therefore, the changes in the level 2 design variables show similar trends in both cases.

6. Concluding Remarks

A semi-analytical sensitivity analysis procedure has been developed for calculating aerodynamic design sensitivities to be used in design optimization problems involving comprehensive CFD solvers. The grid sensitivities and the flow variable sensitivities are calculated by directly differentiating the discretized governing differential equations. The procedure has been developed for the three-dimensional PNS solver, UPS3D. The aerodynamic design sensitivities of wing-body configurations have been calculated using the developed procedure. The computational grid using within UPS3D includes 75 points in the circurmferential direction and 80 points in the normal direction. Results obtained from the semi-analytical sensitivity techniques compare very well with those obtained using a finite difference approach. When the semi-analytical sensitivity analysis techniques are used instead of a finite difference approach within design optimization procedures, these CPU savings become very significant. For a typical sensitivity analysis using four design variables, the procedure yields a 39 percent reduction in CPU time over the finite difference technique. Within the integrated aerodynamic/structural optimization of the delta wing-body configuration where these four design variables are used, the semi-analytical sensitivity analysis techniques decrease the CPU time by 780 seconds per design cycle on the CRAY 2 or nearly 6.5 CPU hours for the entire optimization. During the integrated aerodynamic/sonic boom optimization of the delta wing-body configuration where six design variables are used, the semi-analytical sensitivity analysis techniques offer a savings of 2595 seconds per design cycle (35 %) and approximately 7 CPU hours for the entire optimization. During the integrated aerodynamic/sonic boom optimization of the doubly swept wing-body configuration where eight eight design variables are used, the semi-analytical sensitivity analysis techniques offer a savings of 3460 seconds per design cycle (36.2 %). The time required for the entire optimization decreases by 11 CPU hours due to these CPU savings. Thus, there are two important observations to be made of the semi-analytical sensitivity analysis technques.

1. Significant savings in CPU time are realized by using these techniques instead of the finite difference approach, without any loss in accuracy.
2. The reduction in CPU time for each sensitivity analysis increases as the number of design variables increases.

The second observation is of important consequence in a practical design environment, where a large of design parameters may be used to define the aircraft. In such a situation, the semi-analytical sensitivity analysis procedure will be able to save a very significant amount of computational time. The savings associated with the semi-analytical approach also allows the use of comprehensive analysis procedures (three-dimensional Navier Stokes solvers) within design optimization.

Several multidisciplinary design optimization procedures have been developed for aerospace applications. The MDO procedures for high speed configurations simultaneously improve the aerodynamic, sonic boom and structural performance of the aircraft. The three-dimensional, supersonic flow around the aircraft is calculated using the PNS solver, UPS3D. The wing load carrying member is modeled as either an isotropic box beam or a composite box beam. The isotropic box beam model is analyzed using thin wall theory and the composite box beam model is analyzed using a finite element approach. The aerodynamic design sensitivities have been calculated using the semi-analytical sensitivity analysis techniques. A two-level decomposition procedure is used when structural criteria are included within the optimization formulation. The following summarizes the results from the optimization procedures.

1. The integrated aerodynamic/structural optimization procedure for high speed wing-body configurations yields significant reductions in the aircraft drag and weight while improving the lift.
2. The reduction in the aircraft drag is predominantly due to the significant reduction in the wing thickness-to-chord ratio. The improvement in the lift is due to the increased planform area caused by the increases in the wing root chord and wing span. Reduction in the aircraft weight is achieved through reductions in the wall thicknesses of the wing spar.
3. The multiobjective optimization procedures, for integrated aerodynamic/sonic boom optimization and the two-level optimization procedure, for integrated aerodynamic/sonic boom/structural optimization, are efficient and yield overall improvements in all the performance criteria included in the formulations.
4. Contrary to prior investigations, the multidisciplinary procedures yield low boom configurations that are more slender and hence, aerodynamically efficient. Reductions in the first peak of the sonic boom pressure signature are achieved through significant changes to the nose dimensions of the aircraft. Reduction in the second pressure peak is achieved through changes to the wing planform geometry and thickness-to-chord ratio.
5. The procedure demonstrates the trade-offs between low boom and aerodynamically efficient configurations. The low boom designs have decreased lift associated with them.

6. The percentage reductions in the sonic boom overpressure peaks are smaller for optimizations based on the far field signature than those based on the near field signature.
7. The aircraft weight is affected both by the planform variables as well the beam width-to-chord ratio. The stresses in the plies and the root bending moments are significantly reduced during the optimization through a redistribution of the ply stacking sequence.

The MDO procedures, coupled with the sensitivity analysis techniques, have been found to be efficient and reliable tools for the design of aerospace systems. The procedures are capable of optimizing complete configurations as well as individual components. They bring out the trade-offs between the individual disciplines. They also help identify design parameters that are ineffective during the optimization and hence, can be eliminated from the design variable set. They can be extremely useful tools to the designer by providing insight into the influence of each design variable on the overall performance of the system. The semi-analytical sensitivity analysis techniques offer significant computational savings and allow comprehensive analysis procedures (e.g., Navier Stokes solvers) to be coupled within design optimization.

References

1. Sobieszczanski-Sobieski, J. and Loendorf, D., "A Mixed Optimization Method for Automated Design of Fuselage Structures," *Journal of Aircraft*, Vol. 9, No. 12, December, 1972, pp. 805-811.
2. Fulton, R. E., Sobieszczanski, J., Storaasli, O., Landrum, E. J. and Loendorf, D., "Application of Computer-Aided Aircraft Design in a Multidisciplinary Environment," *Proceedings of the 14th AIAA/ASME/SAE Structures, Structural Dynamics and Materials Conference*, Williamsburgh, Virginia, 1973.
3. Barthelemy, J. F. M., Coen, P. G., Wrenn, G. A., Riley, M. F., Dovi, A. R. and Hall, L. E., "Application of Multidisciplinary Optimization Methods to the Design of a Supersonic Transport," *NASA TM-104073.*
4. Barthelemy, J. F. M., Wrenn, G. A., Dovi, A. R. and Coen, P. C., "Integrating Aerodynamics and Structures in the Minimum Weight Design of a Supersonic Transport Wing," *33rd AIAA/ASME/AHS/ASCE Structures, Structural Dynamics and Materials Conference*, Dallas, Texas, 1992.
5. Dovi, A. R., Wrenn, G. A., Barthelemy, J. F. M., Coen, P. G. and Hall, L. E., "Multidisciplinary Design Integration Methodology for a Supersonic Transport Aircraft" *Journal of Aircraft*, Vol. 32, No. 2, March-April, 1995, pp. 290-297.
6. Celi, R. and Friedmann, P. P., "Structural Optimization with Aeroelastic Constraints of Rotor Blades with Straight and Swept Tips," *AIAA Journal*, Vol. 28, No. 5, 1990, pp. 928-936.
7. Chattopadhyay, A., Walsh, J. L. and Riley, M. F., "Integrated Aerodynamic/Dynamic Optimization of Helicopter Blades," *Special Issue of the AIAA Journal of Aircraft on Multidisciplinary Optimization of Aeronautical Systems*, Vol. II, 1991, pp. 58-64.
8. Chattopadhyay, A. and Narayan, J. R., "Optimum Design of High Speed Prop-Rotors Using a Multidisciplinary Approach," Presented at the *48th Annual Forum of the American Helicopter Society*, Washington D. C., June, 1992.

9. Chattopadhyay, A. and Narayan, J. R., "A Design Optimization Procedure for High Speed Prop-Rotors," AIAA Paper No. 92-2375, *Proceedings of the 33rd AIAA/ASME/ASCE/AHS Structures, Structural Dynamics and Materials Conference*, Dallas, Texas, April, 1992.
10. Chattopadhyay, A., McCarthy, T. R. and Madden, J. F., "A Design Optimization Procedure for Minimizing Drive System Weight of High Speed Prop-Rotors," Presented at the *4th AHS Specialists Meeting on Multidisciplinary Optimization*, Atlanta, Georgia, April, 1993.
11. Chattopadhyay, A., McCarthy, T. R. and Madden, J. F., "Structural Optimization of High Speed Prop-Rotors Including Aeroelastic Stability Constraints," *Mathematical Computer Modelling*, Vol. 18, No. 3/4, 1993, pp. 101-114.
12. Chattopadhyay, A., McCarthy, T. R. and Madden, J. F., "An Optimization Procedure for the Design of Prop-Rotors in High Speed Cruise Including the Coupling of Performance, Aeroelastic Stability and Structures," *Mathematical Computer Modelling*, Vol. 19, No. 3/4, 1994, pp. 75-88.
13. McCarthy, T. R. and Chattopadhyay, A., "Multidisciplinary Optimization of Helicopter Rotor Blades Include Design Variable Sensitivity," Presented at the *4th AIAA/USAF/NASA/OAI Symposium on Multidisciplinary Analysis and Optimization*, Cleveland, Ohio, September, 1992.
14. McCarthy, T. R. and Chattopadhyay, A., "Design of High Speed Prop Rotors Using Multiobjective Optimization Techniques," AIAA Paper No. 93-1032, *Proceedings of the 1993 AIAA/AHS/ASEE Aerospace Design Conference*, Irvine, California, February, 1993.
15. Cramer, E. J., Frank, P. D., Shubin, G. R., Dennis, Jr., J. E. and Lewis, R. M., "On Alternative Problem Formulations for Multidisciplinary Design Optimization," AIAA Paper No. 92-4752, Presented at the *4th AIAA/USAF/NASA/OAI Symposium on Multidisciplinary Analysis and Optimization*, Cleveland, Ohio, September, 1992.
16. Sobieszczanski-Sobieski, J. and Balling, R. J., "Optimization of Coupled Systems: A Critical Overview of Approaches," *AIAA Journal*, Vol. 34, No. 1, January, 1996, pp. 6-11.
17. Schmit, L. A. and Merhinfar, M., "Multilevel Optimum Design of Structures with Fiber-Composite Stiffened-Panel Components," *AIAA Journal*, Vol. 20, No. 1, 1982, pp. 138-147.
18. Schmit, L. A. and Chang, K. J., "A Multilevel Method for Structural Synthesis," *25th AIAA/ASME/AHS/ASCE Structures, Structural Dynamics and Materials Conference*, Palm Springs, California, 1984.
19. Hughes, O. F., "A Method for Nonlinear Optimum Design of Large Structures and Applications to Naval Ship Design," *Proceedings of the International Symposium on Optimum Structural Design*, Tucson, Arizona, October, 1981.
20. Sobieszczanski-Sobieski, J., "A Linear Decomposition Method for Large Optimization Problems - Blueprint for Development," *NASA TM 83248*, February, 1982.
21. Sobieszczanski-Sobieski, J., James, B. and Dovi, A. R., "Structural Optimization by Multilevel Decomposition," *AIAA Journal*, Vol. 23, November, 1985, pp. 1775-1782.
22. Sobieszczanski-Sobieski, J., James, B. and Riley, M. F., "Structural Optimization by Generalized, Multilevel Optimization," *26th AIAA/ASME/AHS/ASCE Structures, Structural Dynamics and Materials Conference*, Orlando, Florida, 1985.

23. Sobieszczanski-Sobieski, J., James, B. and Riley, M. F., "Structural Optimization by Generalized, Multilevel Decomposition," *AIAA Journal* , Vol. 25, January, 1987, pp. 139-145.

24. Wrenn, G. A. and Dovi, A. R., "Multilevel/Multidisciplinary Optimization Scheme for Sizing a Transport Aircraft Wing," *Proceedings of the 28th AIAA/ASME/ASCE/AHS Structures, Structural Dynamics and Materials Conference*, Monterey, California, April, 1987.

25. Haftka, R. T., "An Improved Computational Approach for Multilevel Optimum Design," *Journal of Structural Mechanics*, Vol. 12, No. 2., 1984, pp. 245-261.

26. Kirsch, U., "An Improved Multilevel Structural Synthesis Method," *Journal of Structural Mechanics*, Vol. 13, No. 2, 1985, pp. 123-144.

27. Barthelemy, J. F. M. and Riley, M. F., "Improved Multilevel Optimization Approach for the Design of Complex Engineering Systems," *AIAA Journal*, Vol. 26, No. 3, 1988, pp. 353-360.

28. Barthelemy, J. F. M., "Engineering Applications of Heuristic Multilevel Optimization Methods," *NASA TM 101504*, October, 1988.

29. Bloebaum, C. L. and Hajela, P., "Heuristic Decomposition for Non-Hierarchical Systems," *32nd AIAA/ASME/AHS/ASCE Structures, Structural Dynamics and Materials Conference, AIAA Paper 91-1039,* Baltimore, Maryland, 1991.

30. Rogan, J. E. and Kolb, M. A., "Application of Decomposition Techniques to the Preliminary Design of a Transport Aircraft," *NASA CR 178239*, February, 1987.

31. Adelman, H. M., Walsh, J. L. and Pritchard, J. I., "Recent Advances in Integrated Multidisciplinary Optimization of Rotorcraft," AIAA Paper 92-4777, *4th AIAA/USAF/NASA/OAI Symposium on Multidisciplinary Analysis and Optimization,* Cleveland, Ohio, 1992.

32. Chattopadhyay, A., McCarthy, T. R. and Pagaldipti, N., "Multilevel Decomposition Procedure for Efficient Design Optimization of Helicopter Rotor Blades," *AIAA Journal*, Vol. 33, No. 2, February, 1995, pp. 223-230. Also presented as Paper n^{o}G7, *19th European Rotorcraft Forum*, Italy, 1993.

33. Chattopadhyay, A., McCarthy, T. R. and Seeley, C. E., "A Decomposition Based Optimization Procedure for High Speed Prop-Rotors Using Composite Tailoring and Simulated Annealing," *Journal of Aircraft*, Vol. 32, No. 5, 1995, pp. 1026-1033.

34. Sobieszczanski-Sobieski, J., Barthelemy, J. F. M. and Riley, M. F., "Sensitivity of Optimum Solutions to Problem Parameters," *AIAA Journal,* Vol. 20, September, 1982, pp. 1291-1299.

35. Barthelemy, J. F. M. and Sobieszczanski-Sobieski, J., "Optimum Sensitivity Derivatives of Objective Functions in Nonlinear Programming," *AIAA Journal*, Vol. 21, June, 1983, pp. 913-915.

36. Sobieszczanski-Sobieski, J., "Sensitivity Analysis and Multidisciplinary Optimization for Aircraft Design: Recent Advances and Results," *NASA TM 100630*, 1988.

37. Sobieszczanski-Sobieski, J., "On the Sensitivity of Complex, Internally Coupled Systems," *AIAA Journal*, Vol. 28, No. 1, 1990.

38. Fluery, C. and Shyy, Y. K., "Shape Sensitivity Derivatives: Finite Differences Versus Analytical Approaches," *AIAA Journal*, 1990, pp. 184-195.

39. Tsay, J. J. and Arora, J. S., "Nonlinear Structural Design Sensitivity Analysis for Path Dependent Problems. Part 1: General Theory," *Computer Methods in Applied Mechanics and Engineering 81, pp. 183-208*, 1990.
40. Rajan, S. D. and Gani, L., "Improving Computational Efficiency of Sizing and Shape Optimal Design Process," *1st U.S. National Congress on Computational Mechanics*, Chicago, Illinois, 1991.
41. Wang, S. Y., Sun, Y. and Gallager, R. H., "Sensitivity Analysis in Shape Optimization of Continuum Structures," *Computers and Structures*, Vol. 20, 1985, pp. 855-867.
42. Chattopadhyay, A. and Guo, R., "Nonlinear Structural Design Sensitivity Analysis for Composites Undergoing Elastoplastic Deformation," Presented at the *Army Research Office Workshop on Dynamic Response of Composite Structures*, New Orleans, Louisiana, 1993. Also in Press for Publication in *Mathematical and Computer Modeling*.
43. Chattopadhyay, A. and Guo, R., "Development of a Finite Element-Based Design Sensitivity Analysis for Buckling and Post Buckling of Composite Plates,"*Mathematical Problems in Engineering: Theory, Methods and Applications*, Vol. 1, March, 1995, pp. 255-274.
44. Elbanna, H. and Carlson, L., "Determination of Aerodynamic Sensitivity Coefficients in the Transonic and Supersonic Regimes," AIAA Paper No. 89-0532, *27th Aerospace Sciences Meeting*, Reno, Nevada, 1989.
45. Elbanna, H. and Carlson, L., "Determination of Aerodynamic Sensitivity Coefficients in the Transonic and Supersonic Regimes," *Journal of Aircraft*, Vol. 27, No. 6, pp. 507-518, 1990.
46. Elbanna, H. and Carlson, L., "Determination of Aerodynamic Sensitivity Coefficients Based on the Three-Dimensional Full Potential Equation," AIAA Paper No. 92-2670, 1992, pp. 539-548.
47. Elbanna, H. M. and Carlson, L. A., "Aerodynamic Sensitivity Coefficients Using the Three-Dimensional Full Potential Equation," *Journal of Aircraft*, vol. 31, No. 5, September-October, 1994, pp. 1071-1077.
48. Baysal, O. and Elashaky, M. E., "Aerodynamic Sensitivity Analysis Methods for the Compressible Euler Equations," *Journal of Fluids Engineering, Vol. 113, No. 4*, 1991, pp. 681-688.
49. Elashaky, M. E. and Baysal, O., "Preconditioned Domain Decomposition Scheme for Three-Dimensional Aerodynamic Sensitivity Analysis," *Proceedings of the 12th AIAA Computational Fluid Dynamics Conference, Open Forum Paper*, 1993, pp. 1055-1056.
50. Elashaky, M. E. and Baysal, O., "Shape Optimization of a 3-D Nacelle near a Flat Plate Wing using Multiblock Sensitivity Analysis," AIAA Paper No. 94-0160, *32nd Aerospace Sciences Meeting and Exhibit*, Reno, Nevada, 1994.
51. Burgreen, G. W. and Baysal, O., "Three-Dimensional Aerodynamic Shape Optimization of Wings Using Sensitivity Analysis," AIAA Paper No. 94-0094, *32nd Aerospace Sciences Meeting and Exhibit*, Reno, Nevada, 1994.
52. Korivi V. M., Taylor A. C., Newman P. A., Hou G. J. W. and Jones H. E., "An Approximately Factored Incremental Strategy For Calculating Consistent Discrete Aerodynamic Sensitivity Derivatives," AIAA-92-4746-CP, Presented at the *4th AIAA/USAF/NASA/OAI Symposium on Multidisciplinary Analysis and Optimization*, Cleveland, Ohio, September, 1992.
53. Newman P. A., Hou G. J. W., Jones H. E., Taylor A. C. and Korivi V. M., "Observations on Computational Methodologies for Use in Large-Scale, Gradient-Based, Multidisciplinary Design," AIAA-92-4753-CP, Presented at the *4th AIAA/USAF/NASA/OAI Symposium on Multidisciplinary Analysis and Optimization*, Cleveland, Ohio, September, 1992
54. Haftka, R. T. and Grandhi, R. V., "Structural Shape Optimization: A Survey," *Computer Methods in Applied Mechanics and Engineering*, Vol. 57, No. 1, pp. 91-106, 1986.

55. Pironneau, O., Optimal Shape Design for Elliptic Systems, Springer-Verlag New York Inc., New York, 1985.
56. Dems, K. and Mroz., "Variational Approach by Means of Adjoint Systems to Structural Optimization and Sensitivity Analysis - II, Structural Shape Variation," *International Journal of Solids and Structures*, Vol. 20, No. 6, pp. 527-552, 1984.
57. Jameson, A., "Aerodynamic Design Via Control Theory," Journal of Scientific Computing, Vol. 3, 1988, pp. 233-260.
58. Jameson, A., "Automatic Design of Transonic Airfoils to Reduce the Shock Induced Pressure Drag," *Proceedings of the 31st Israel Annual Conference on Aviation and Aeronautics*, Tel Aviv, 1990, pp. 5-17.
59. Reuther, J. and Jameson, A., "Control Theory Based Airfoil Design for Potential Flow and a Finite Volume Discretization," AIAA Paper No. 94-0499, *32nd Aerospace Sciences Meeting*, Reno, Nevada, 1994.
60. Bischof, C. and Griewank, A., "ADIFOR: A FORTRAN System for Portable Automatic Differentiation," AIAA Paper 92-4744 CP, *4th AIAA/USAF/NASA/OAI Symposium on Multidisciplinary Analysis and Optimization*, Cleveland, Ohio, 1992, pp. 433-441.
61. Bischof, C., Corliss, G., Green, L., Griewank, A., Haigler, K. and Newman, P., "Automatic Differentiation of Advanced CFD Codes for Multidisciplinary Design," *Symposium on High Performance Computing for Flight Vehicles*, Arlington, Virginia, 1992.
62. Barthelemy, J. F. M. and Hall, L. E., "Automatic Differentiation as a Tool in Engineering Design," AIAA Paper 92-4743 CP, *4th AIAA/USAF/NASA/OAI Symposium on Multidisciplinary Analysis and Optimization*, Cleveland, Ohio, 1992, pp. 424-432.
63. Anderson, D. A., Tannehill, J. C. and Pletcher, R. H., Computational Fluid Mechanics and Heat Transfer, Hemisphere Publishing Corporation, 1984.
64. Hoffmann, K. A., Computational Fluid Mechanics for Engineers, *A Publication of Engineering Education System*, Austin, Texas, 1989.
65. Taylor A. C., Hou G. J. W. and Korivi V. M., "A Methodology for Determining Aerodynamic Sensitivity Derivatives With Respect to Variation of Geometric Shape," AIAA Paper 91-1101 CP, 1991.
66. Taylor A. C., Korivi V. M. and Hou G. J. W., "Approximate Analysis and Sensitivity Analysis Methods for Viscous Flow Involving Variation of Geometric Shape," AIAA Paper 91-1569 CP, 1991.
67. Hou G. J. W., Taylor A. C. and Korivi V. M., "Discrete Shape Sensitivity Equations for Aerodynamic Problems," AIAA Paper 91-2259, *AIAA/SAE/ASME/ASEE 27th Joint Propulsion Conference*, Sacremento, California, 1991.
68. Taylor A. C., Hou G. J. W. and Korivi V. M., "Sensitivity Analysis, Approximate Analysis and Design Optimization for Internal and External Viscous Flows," AIAA Paper 91-3083, *AIAA Aircraft Design Systems and Operations Meeting*, Baltimore, Maryland, 1991.
69. Sadrehaghighi I. and Smith R. E., Jr. and Tiwari S. N., "An Analytical Approach To Grid Sensitivity Analysis," AIAA Paper 92-0660, *30th Aerospace Sciences Meeting and Exhibit*, Reno, Nevada, January, 1992.
70. Sadrehaghighi I. and Smith R. E., Jr. and Tiwari S. N., "Grid Sensitivity and Aerodynamic Optimization of Generic Airfoils," *Journal of Aircraft*, Vol. 32, No. 6, November-December, 1995, pp. 1234-1239.
71. "National Aeronautical R & D Goals - Agenda for Achievement," Executive Office of the President, Offices of Science and Technology Policy, 1987.
72. Robins, A. W., Dollyhigh, S. M., Beissner, F. L., Jr., Geiselhart, K. G., Martin, G. L., Shields, E. W., Swanson, E. E., Coen, P. G. and Morris, S. J., Jr., "Concept Development of a Mach 3.0 High Speed Civil Transport," *NASA TM-4058*, 1988.

73. Boeing Commercial Airplanes, "High Speed Civil Transport Study," Summary, *NASA CR-4234*, 1989.
74. Douglas Aircraft Company, "Summary of High Speed Civil Transport Study," *NASA CR-4236*, 1989.
75. Ozoroski, L. P., Shields, E. W., Fenbert, J. W. and McElroy, M. O., "Benefits Associated With Advanced Technologies Applied to a High Speed Civil Transport Concept," AIAA Paper 93-1173, *AIAA/AHS/ASEE Aerospace Design Conference*, Irvine, California, 1993.
76. Haney, H. P., Johnson, R. R. and Hick, R. M., "Computational Optimization and Wing Tunnel Test of Transonic Wing Designs," AIAA Paper No. 79-0080, 1979.
77. Carlson, H. W. and Mann, M. J., "Survey and Analysis of Research on Supersonic Drag-to-Lift Minimization With Recommendations for Wing Design," *NASA TP-3202*, 1992.
78. Cheung, S. H. and Edwards, T. A., "CFD Optimization of a Theoretical Minimum-Drag Body," *Journal of Aircraft*, Vol. 32, No. 1, January-February, 1995, pp. 193-198.
79. Ibrahim, A. H. and Baysal, O., "Design Optimization Using Variational Methods and CFD," *32nd Aerospace Sciences Meeting and Exhibit*, Reno, Nevada, 1994.
80. Jones, L. B., "Lower Bounds for Sonic Bangs," *Journal of Royal Aeronautical Society*, Vol. 65, No. 606, June, 1961, pp. 433-436.
81. Jones, L. B., "Lower Bounds for Sonic Bangs in the Far Field," *Aeronautical Quarterly*, Vol. XVIII, Pt. 1, February, 1967, pp. 1-21.
82. Seebass, R., "Minimum Sonic Boom Shock Strengths and Overpressures," *Nature*, Vol. 221, No. 5181, February, 1969, pp. 651-653.
83. George, A. R., "Lower Bounds for Sonic Booms in the Midfield," *AIAA Journal*, Vol. 7, No. 8, August 1969, pp. 1542-1545.
84. George, A. R. and Seebass, R., "Sonic Boom Minimization Including Both Front and Rear Shocks," *AIAA Journal*, Vol. 9, No. 10, October, 1971, pp. 2091-2093.
85. Seebass, R. and George, A. R., "Sonic-Boom Minimization," *Journal of Acoustical Society of America*, Vol. 51, No. 2, Pt. 3, 1972.
86. Darden, C. M., "Minimization of Sonic-Boom Parameters in Real and Isothermal Atmospheres," *NASA TN D-7842*, 1975.
87. Darden, C. M., "Sonic Boom Minimization with Nose-Bluntness Relaxation," *NASA Technical Paper 1348*, 1979.
88. Rudman, S. and Rubin, S. G., "Hypersonic Viscous Flow Over Slender Bodies with Sharp Leading Edges," *AIAA Journal*, Vol. 6, 1968, pp. 1883-1889.
89. Lubard, S. C. and Helliwell, W. S., "Calculation of the Flow on a Cone at High Angle of Attack," *AIAA Journal*, Vol. 12, 1973, pp. 965-974.
90. Lawrence, S., Chaussee, D. and Tannehill, J., "Application of an Upwind Algorithm to the 3-D Parabolized Navier-Stokes Equations," AIAA Paper 87-1112, *AIAA 8th Computational Fluid Dynamics Conference*, Honolulu, Hawaii, June, 1987.
91. Roe, P. L., "Approximate Reimann solver, Parameter Vectors and Difference Schemes," *Journal of Computational Physics*, Vol. 43, 1981, pp. 357-372.
92. Chattopadhyay, A. and Pagaldipti, N., "A Multilevel Decomposition Procedure for Efficient Design of High Speed Civil Transport," AIAA Paper No. 94-0097, Presented at the *32nd Aerospace Sciences Meeting and Exhibit*, Reno, Nevada, 1994.
93. Chattopadhyay, A. and Pagaldipti, N., "A Multidisciplinary Optimization Using Semi-Analytical Sensitivity Analysis Procedure and Multilevel Decomposition," *Journal of Computers and Mathematics with Applications*, Vol. 29, No. 7, 1995, pp. 55-66.
94. Pagaldipti, N. and Chattopadhyay, A., "A Discrete Semi-Analytical Procedure for Aerodynamic Sensitivity Analysis Including Grid Sensitivity," AIAA Paper 94-4268, *5th AIAA/USAF/NASA/ISSMO Symposium on Multidisciplinary Analysis and Optimization*, Panama City, Florida, September, 1994.

95. Pagaldipti, N. and Chattopadhyay, A., "A Discrete Semi-Analytical Procedure for Aerodynamic Sensitivity Analysis Including Grid Sensitivity," Accepted for Publication in the *Journal of Computers and Mathematics with Applications*, February, 1996.

96. Narayan, J. R., Chattopadhyay, A., Pagaldipti, N. and Cheung, S. H., "Optimization Procedure for Improved Sonic Boom and Aerodynamic Performance Using a Multiobjective Formulation Technique," AIAA Paper 95-0127, *33rd AerospaceSciences Meeting and Exhibit*, Reno, Nevada, January 1995.

97. Chattopadhyay, A., Narayan, J. R., Pagaldipti, N., Wensheng, X. and Cheung, S. H., "Optimization Procedure for Reduced Sonic Boom in High Speed Flight," AIAA Paper 95-2156, *26th AIAA Fluid Dynamics Conference,* San Diego, California, June, 1995.

98. Narayan, J. R., Chattopadhyay, A. and Pagaldipti, N., "Development of a Multiobjective Optimization Procedure for Sonic Boom Minimization," *NASA HSR Program Sonic Boom Workshop*, NASA Langley Research Center, Hampton, Virginia, 1995.

99. Pagaldipti, N., Narayan, J. R. and Chattopadhyay, A., "Optimization Procedure With Analytical Aerodynamic Sensitivity for Reduced Sonic Boom Design," Under Review for Publication in the *AIAA Journal of Aircraft*, 1996.

100. Pagaldipti, N., Narayan, J. R. and Chattopadhyay, A., "Multidisciplinary Optimization Procedure for High Speed Aircraft Using Semi-Analytical Sensitivity Analysis Procedure and Multilevel Decomposition," AIAA Paper No. 96-1478, *AIAA/ASME/ASCE/AHS/ASC 37th Structures, Structural Dynamics and Materials Conference*, Salt Lake City, Utah, April, 1996.

101. Pagaldipti, N., Narayan, J. R. and Chattopadhyay, A., "Multidisciplinary Optimization Procedure for High Speed Aircraft Using Semi-Analytical Sensitivity Analysis Procedure and Multilevel Decomposition," Submitted to *Engineering Optimization*, 1996.

102. Steger, J. L. and Chaussee, D. S., "Generation of Body-Fitted Coordinates Using Hyperbolic Partial Differential Equations," SIAM Journal of Scientific and Statistical Computation, 1, 1980, pp. 431-437.

103. Steger, J. L. and Rizk, Y. M., "Generation of Three-Dimensional Body-Fitted Coordinates Using Hyperbolic Partial Differential Equations," *NASA TM 86753*, 1985.

104. Chan, W. M. and Steger, J. L., "A Generalized Scheme for Three-Dimensional Hyperbolic Grid Generation," AIAA Paper No. 91-1588-CP, *10th AIAA Computational Fluid Dynamics Conference*, June, 1991.

105. Vigneron, Y. C., Rakich, J. V. and Tannehill, J. C., "Calculation of Supersonic Viscous Flow over Delta Wings with Sharp Subsonic Leading Edges," AIAA Paper No. 78-1137, 1978.

106. Kreisselmeier, A. and Steinhauser, R., "Systematic Control Design by Optimizing a Vector Performance Index," *Proceedings of the IFAC Symposium on Computer Aided Design of Control Systems*, Zurich, Switzerland, 1979, pp. 113.-117.

107. Wrenn, G. A., "An Indirect Method for Numerical Optimization Using the Kreisselmeier-Steinhauser Function," AIAA Paper No. 87-1112, June 1987.

108. Haftka, R. T., Gurdal, Z. and Kamat, M. P., Elements of Structural Optimization, *Kluwer Academic Publishers*, Dordrecht, The Netherlands, 1990.

109. Vanderplaats, G. N., "A Robust Feasible Directions Algorithm for Design Synthesis," *Proceedings of the AIAA/ASME/ASCE/AHS 24th Structures, Structural Dynamics and Materials Conference*, Lake Tahoe, Nevada, 1983.

110. Vanderplaats, G. N., "CONMIN-A FORTRAN Program for Constrained Function Minimization," *Users Manual, NASA TMX-62282*, 1973.

111. Fadel, G. M., Riley, M. F. and Barthelemy, J. F. M., "Two-Point Exponential Approximation Method for Structural Optimization," *Structural Optimization*, 2, 1990, pp. 117-124.

112. McCarthy, T. R., Chattopadhyay, A. and Zhang, S., "A coupled Rotor/Wing Optimization Procedure for High Speed Tilt-Rotor Aircraft," *51st Annual Forum of the American Helicopter Society*, Fort Worth, Texas, 1995.

113. McFarland, E. R., "Solution of Plane Cascade Flows Using Improved Surface Singularity Methods," *ASME Journal of Engineering for Gas Turbine and Power*, Vol. 104, July, 1982, pp. 668-674.

114. McFarland, E. R., "A Rapid Blade to Blade Solution for Use in Turbomachinery Design," *ASME Journal of Engineering for Gas Turbine and Power*, Vol. 106, April, 1984, pp. 376-384.

115. Lieblein, S. and Stockman, N. O., "Compressibility Correction for Internal Flow Solutions," Journal of Aircraft, Vol. 9, No. 4, April, 1972, pp. 312-313.

116. Chapman, A. J., Heat Transfer, *Third Edition, Macmillan Publishing Co., Inc.*, 1974.

117. Haack, W., "Projectile Shapes for Smallest Wave Drag," Translation No. A9-T3, Contract W33-038-ac-15004 (16351), ATI No. 27736, Air Material Command, U.S. Air Force, Brown University, 1948.

118. Adams, A. C., "Determination of Shapes of Boattail Bodies of Revolution for Minimum Wave Drag," NACA TN-2550, 1951.

119. Peery, D. J. and Azar, J. J., Aircraft Structures, McGraw-Hill Book Company, USA, 1982.

120. Cheung, S. H., Edwards, T. A. and Lawrence, S. L., "Application of Computational Fluid Dynamics to Sonic Boom Near- and Mid-Field Prediction," *Journal of Aircraft*, Vol. 29, No. 5, 1992, pp. 920-926.

121. Whitham, G. B., "The Flow Pattern of a Supersonic Projectile," *Communications on Pure and Applied Mathematics*, Vol. 5, No. 3, 1952, pp. 301-348.

122. Lighthill, M. J., "General Theory of High Speed Aerodynamics, Sec. E; see also High Speed Aerodynamics and Propulsion," Vol. 6, Princeton University Press, Princeton, NJ, 1954, pp. 345-389.

123. Walkden, F., "The Shock Pattern of a Wing-Body Combination, Far From the Flight Path," *Aeronautical Quarterly*, Vol. 9, Pt. 2, May 1958, pp. 164-194.

124. Hicks, R. and Mendoza, J., "Prediction of Aircraft Sonic Boom Characteristics from Experimental Near Field Results," NASA TMX1477, November 1967.

125. Smith, E. C. and Chopra, I., "Formulation and Evaluation of an Analytical Model for Composite Box Beams," *Proc. 31st AIAA/AHS/ASME/ASCE/ASC SDM Conference*, Long Beach, California, 1990.

126. Tsai, S. W. and Wu, E., "A General Theory of Strength for Anisotropic Materials," *Journal of Composite Materials*, 5, 1971, pp. 58-80.

127. Chattopadhyay, A. and Seeley, C. E., "Development of a Hybrid Optimization Technique with Applications to Buckling of Cylindrical Shells," *1st World Congress of Structural and Multidisciplinary Optimization*, Germany, May 28 - June 2, 1995.